The Impact of Planar-Geometry Cathodes on Hall Thruster Performance

Jonah Taylor

A thesis
submitted in partial fulfillment of the
requirements for the degree of

Master of Science

University of Washington

2023

Committee:

Justin Little

Uri Shumlak

Program Authorized to Offer Degree:
Aeronautics and Astronautics

University of Washington

Abstract

The Impact of Planar-Geometry Cathodes on Hall Thruster Performance

Jonah Taylor

Chair of the Supervisory Committee:
Justin Little
Department of Aeronautics and Astronautics

This thesis explores the viability of planar cathodes for improving Hall thruster performance. A mathematical model is presented that calculates how the total efficiency of a Hall thruster changes when operated with a planar cathode instead of the traditionally utilized hollow cathode. The model assumes that a Hall thruster's anode efficiency is completely agnostic to the type of cathode employed and any difference in total efficiency will manifest in the thruster's cathode and electrical efficiencies. A one-dimensional model of the planar cathode's sheath is used to calculate the electrical efficiency of a Hall thruster equipped with a centrally mounted planar cathode as a function of the thruster's discharge voltage, discharge current, voltage utilization efficiency, current utilization efficiency, and the cathode's geometry and material properties. This sheath model is also used to calculate the maximum, space charge limited, discharge current a planar cathode can provide. This model demonstrates that under the correct conditions, the electrical and cathode efficiencies of a Hall thruster will be larger when operated with a planar cathode, leading to an increase in total thruster efficiency. Conversely, planar cathodes are far more susceptible to space charge issues and their ability to provide discharge currents of the magnitude desired by Hall thrusters is heavily reliant on the thruster having a sufficiently low voltage utilization efficiency. Working under this restriction, planar cathodes could

be a viable option on Hall thrusters that possess low voltage utilization efficiencies at their nominal operation conditions.

TABLE OF CONTENTS

LIST OF FIGURES

LIST OF TABLES

NOMENCLATURE

v_{ex}	Propellant exhaust velocity
$\dot{m}_p$	Total propellant mass flow rate
P_{sys}	Momentum of the rocket-exhaust system
Δv	Change in rocket velocity
m_0	Initial mass of the spacecraft
m_f	Final mass of the spacecraft
m_p	Mass of propellant spent to achieve Δv
F_T	Thrust force
I	Rocket impulse
I_{sp}	Specific impulse
g	Gravitational acceleration
K_{sys}	Kinetic energy of the rocket-exhaust system
P_{jet}	Jet power
P_{in}	Total thruster input power

η_T	Total efficiency of a thruster
Z	Ion charge state
v_{ex}^{+z}	Exhaust velocity of +Z ions
m_i	Propellant ion mass
V_b	Beam voltage
e	Charge of an electron
F_T^{+z}	Thrust force from +Z ions
$\dot{m}_{i+Z}$	Mass flow rate of +Z ions
$F_{T,n}$	Thrust force from neutral particles
$\dot{m}_n$	Mass flow rate of neutral particles
v_n	Exhaust velocity of neutral particles
I^{+z}	Current of +Z ions
I_b	Total ion beam current
f_i	Ratio of I^{+z} to the total beam current
$\dot{m}_i$	Total ion mass flow rate
I_{br}	Radial component of the ion beam current

I_{bz}	Axial component of the ion beam current
$I_{b,eff}$	Effective ion beam current
θ	Half-angle divergence of the ion beam
η_θ	Plume divergence efficiency
η_m	Mass utilization efficiency
η_q	Charge utilization efficiency
j_{th}	Emitted current density
ϕ_0	Work function of an emitter
α	Temperature dependent component of the work function
A	Richardson's constant
k	Boltzmann's constant
T	Surface temperature of the emitter
$\Delta\phi$	Shottkey Term
E_c	Magnitude of the electric field component normal to the emitter surface
ϵ_0	Permittivity of free space
R_1	Inner radius of a Hall thruster's channel

D_1	Inner diameter of a Hall thruster's channel
R_2	Outer radius of a Hall thruster's channel
D	Mean channel diameter of a Hall thruster
W	Channel width of a Hall thruster
A_{ch}	Cross-sectional channel area of a Hall thruster
$\dot{m}_a$	Anode mass flow rate
I_d	Discharge current
V_d	Discharge voltage
P_d	Discharge power
η_v	Voltage utilization efficiency
V_{cc}	Cathode coupling voltage
$\dot{m}_a$	Cathode mass flow rate
η_c	Cathode efficiency
η_b	Current utilization efficiency of a Hall thruster
P_{mag}	Power consumed by the magnets
P_{heat}	Power used to heat the cathode

P_{keep}	Power consumed by the keeper electrode
η_0	Electrical efficiency
η_{ma}	Anode mass utilization efficiency
η_a	Anode efficiency
$(\eta_c\eta_0)_{hollow}$	Product of the cathode and electrical efficiencies for a hollow cathode
$(\eta_c\eta_0)_{planar}$	Product of the cathode and electrical efficiencies for a planar cathode
η_{mag}	Ratio of the magnet power to the discharge power
V_s	Voltage drop across the planar cathode's sheath
L	Position of the sheath edge
V_0	Voltage drop across the planar cathode's pre-sheath
V_c	Sum of the sheath and pre-sheath potential drops
$V(x)$	Electric potential inside the sheath
$n_{th}(x)$	Density of emitted electrons inside the sheath
$n_i(x)$	Density of plasma ions inside the sheath
$n_e(x)$	Density of plasma electrons inside the sheath
n_0	Bulk plasma density

T_e	Bulk plasma electron temperature
m_e	Mass of an electron
n_{i0}	Plasma ion density at the sheath edge
n_{e0}	Plasma electron density at the sheath edge
P_{rad}	Radiated power loss from the emitter surface
σ	Stefan-Boltzmann constant
ϵ	Emissivity of the planar cathode's emitter
A_c	Area of the planar cathode's emitter
P_{emit}	Emitted power loss
ϕ_t	Total work function of the emitter
I_i	Back-streaming plasma ion current
U^+	First ionization energy of the propellant
P_i	Plasma ion power transferred to the emitter
I_e	Back-streaming plasma electron current
P_e	Plasma electron power transferred to the emitter
η_{heat}	Fraction of the heating power conducted into the emitter

P_{heat}	Required cathode heating power
V_r	Voltage drop between the planar cathode's sheath and the ion beam
j_{max}	Maximum emitted current density
$I_{d,max}$	Maximum discharge current
J_{ch}	Discharge current density in the thruster channel
$n_{0,ex}$	Plasma density at the channel exit
$T_{e,ex}$	Electron temperature at the channel exit
V_{sat}	Saturation voltage
$r_{c,min}$	Smallest emitter radius capable of providing a given discharge current
$D_{c,min}$	Smallest emitter diameter capable of providing a given discharge current
V_{int}	Potential drop between the insert and the hollow cathode's orifice
V_{plume}	Potential drop between the cathode's orifice and the thruster's plume

ACKNOWLEDGMENTS

I would first like to thank my advisor, Justin Little, for taking me into the SPACE Lab and providing me with so many valuable opportunities. You were an incredibly supportive and patient mentor and I'm grateful for all the help you gave me. I would also like to thank Peter Thoreau for putting up with my myriad of annoying engineering and Hall thruster-related questions over the years. I owe a lot of my progress and understanding of various concepts to you. Lastly, I would like to thank Curtis Promislow for being the only other nocturnal member of SPACE Lab. All those nights I spent setting up my experiment would have been a lot lonelier and spookier if you weren't also there toiling away in lab.

DEDICATION

To my friends and family, who supported me along the way.

Chapter 1

INTRODUCTION

1.1 Motivation for This Research

Hall thrusters are an electrostatic propulsion device first conceptualized in the 1960's and flown in space for the first time on a Russian weather satellite in 1971 [3]. As of 2012, Hall thrusters have been successfully flown on over 240 different spacecraft [24]. These thruster's have been primarily been utilized for station keeping on earth orbiting satellites, however their viability as the primary propulsion system on longer range spacecraft, such as the European Space Agency's SMART-1 satellite [16], has been demonstrated as well. Future expeditions utilizing this technology include the Psyche mission, where a spacecraft equipped with four Hall thrusters as its primary propulsion system will be sent to orbit the Psyche-16 asteroid and study its composition [35]. Given the established, and continued, importance of these devices, exploring means of maximizing their performance is always of interest.

Laboratory and flight proven Hall thrusters have historically employed hollow cathodes as a source of free electrons for their operation. As will be discussed later chapter, hollow cathodes possess a number of attributes that make them an attractive option for this particular role, and little research has been conducted to explore alternate cathode types for use on Hall thrusters. In response to this lack of research, this thesis will analyze planar cathodes, with the goal of determining under what conditions these devices can improve Hall thruster performance.

1.2 Thesis Structure

The basic physics of rocket propulsion is presented in chapter 2. The physics of electrostatic propulsion is also discussed. It's here that the equations for the total efficiency and specific impulse of an electrostatic thruster are derived.

Chapter 3 begins with a discussion the physics of thermionic emission and commonly used electron emitting materials. Following that, the operational principals of both hollow cathodes and planar cathodes are described.

Chapter 4 gives a brief overview of the physics of Hall thrusters. It concludes by deriving an expression for the total efficiency of a Hall thruster.

Chapter 5 presents the mathematical model that will be used to compare the total efficiency of a Hall thruster equipped with a planar cathode, to that of a Hall thruster equipped with a hollow cathode. This model is also used to determine the maximum discharge current that a planar cathode can supply.

Chapter 6 uses the model presented in the previous chapter to calculate the efficiency of a planar cathode equipped Hall thruster as a function of the thruster's discharge properties. The maximum discharge current is also calculated as a function of these same properties.

Chapter 7 provides a summary of the results of the previous chapter and describes the conditions under which a planar could be a superior option to a hollow cathode. Experimental data from several real Hall thrusters is used to calculate the change in efficiency these thruster's would undergo if they were instead operated with a planar cathode.

Chapter 8 describes an experiment that was designed to test the validity of certain parts of the model presented in chapter 5.

Chapter 9 Discusses the imitations of the model and provides a reccomendation for futrue work.

Chapter 2

ROCKET PROPULSION BASICS

2.1 The Tsiolkovsky Rocket Equation

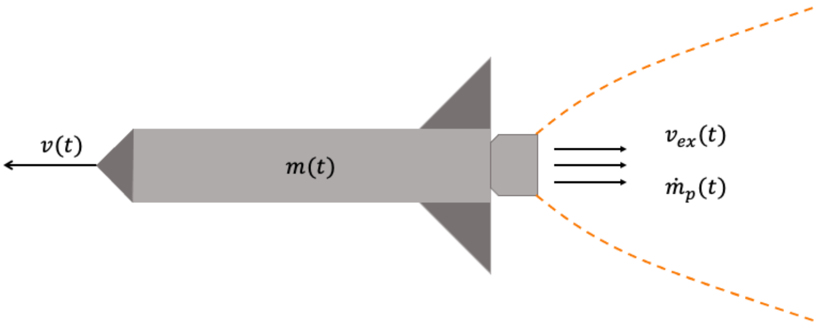

Figure 2.1: A generic rocket firing its thrusters at some time $t > 0$.

Figure 2.1 shows a generic rocket and its exhaust at some time $t > 0$, assuming the rocket began firing its thrusters at $t = 0$. In this diagram, $m(t)$ is the mass of the rocket, $v(t)$ is the rocket's velocity relative to a stationary observer, $v_{ex}(t)$ is the velocity of the exhaust relative to the rocket, and $\dot{m}_p(t) = -dm(t)/dt$ is the mass flow rate of the exhaust. The total momentum of the rocket-exhaust system at time t is then

$$P_{sys}(t) = m(t)v(t) + \int_0^t \dot{m}_p(t') \left[v(t') - v_{ex}(t')\right] dt' \tag{2.1}$$

where the first term represents the momentum of the rocket, and the second term represents the momentum of the exhaust.

If no external forces are acting on the system, then the total system momentum should be constant in time. Taking the time derivative of equation 2.1, setting it equal to zero, and simplifying, results in the relationship below.

$$m(t)\frac{dv(t)}{dt} = -v_{ex}(t)\frac{dm(t)}{dt} \tag{2.2}$$

If v_{ex} is taken to be constant in time, both sides of the above equation can be integrated over some arbitrary time interval $[t_0, t_f]$, over which the rocket is ejecting propellant, to yield the following equation.

$$\Delta v = v_{ex} \ln \frac{m_0}{m_f} \tag{2.3}$$

Here, $m_0 = m(t_0)$ is the initial mass of the spacecraft before ejecting any propellant, $m_f = m(t_f)$ is the final mass of the spacecraft after ejecting some propellant, and $\Delta v = v(t_f) - v(t_0)$ is the resulting change in the rocket's velocity. The mass of propellant spent, m_p, is simply the difference between the initial and final mass of the spacecraft. Taking that into account, equation 2.3 can be re-expressed in a more elucidating form.

$$m_p = m_0 \left(1 - e^{-\frac{\Delta v}{v_e}}\right) \tag{2.4}$$

Equation 2.4 is known as the Tsiolkovsky rocket equation [11] and it relates a rocket's Δv to the mass of propellant spent to achieve said change in velocity. For any space mission, an important quantity to minimize is the propellant mass fraction, m_p/m_0. The smaller this ratio, the more total spacecraft mass can be dedicated to useful payload instead of propellant. From equation 2.4 it's clear that, for a given Δv maneuver, the propellant mass fraction can be reduced by increasing the exhaust speed of the propellant.

2.2 Specific Impulse

Referring back to equation 2.2, the left hand side is the mass of the rocket multiplied by its acceleration. This means that the right hand side is the thrust-force, F_T, acting upon the rocket.

$$F_T = \dot{m}_p v_{ex} \tag{2.5}$$

The total change in a rocket's momentum over a time interval $[0, t]$ is known as the impulse, $I(t)$, and it's found by integrating the thrust force over said time interval.

$$I(t) = \int_0^t F_T dt' = \int_0^t \dot{m}_p v_{ex} dt' \tag{2.6}$$

In rocketry there is an additional quantity of interest known as the specific impulse, I_{sp}. This is the impulse divided by the total weight (subjected to Earth's gravitational field) of propellant spent to achieve said impulse.

$$I_{sp} = \frac{\int_0^t \dot{m}_p v_{ex} dt'}{g \int_0^t \dot{m}_p dt'} \tag{2.7}$$

In essence, the specific impulse is a measure of the rocket's fuel efficiency. Assuming the exhaust velocity is constant over this time interval, the above equation simplifies to

$$I_{sp} = \frac{v_{ex}}{g} \tag{2.8}$$

From equation 2.8 it can be seen that the faster a rocket expels its propellant, the more momentum per unit of propellant is imparted to the rocket. This explains why rockets operating with larger exhaust velocities can carry lower propellant mass fractions for a given mission.

2.3 Total Thruster Efficiency

Referring back to figure 2.1, the total kinetic energy, K_{sys}, of the rocket-exhaust system at some time $t > 0$ is given by

$$K_{sys} = \frac{1}{2}m(t)v(t)^2 + \int_0^t \dot{m}_p(t)[v(t') - v_{ex}]^2 dt' \tag{2.9}$$

where the first term is the kinetic energy of the rocket and the second term is the kinetic energy of the exhaust. The time rate of change of the total kinetic energy of the system is then given by

$$\frac{dK_{sys}}{dt} = \frac{1}{2}\dot{m}_p v_{ex}^2 \tag{2.10}$$

The above quantity is also referred to as the "jet power", P_{jet}, and has units of watts [11]. Physically, the jet power is the total power delivered, by the thruster, to all masses in the system (both the rocket and the exhaust). Some of this power goes to accelerating the rocket itself, while the rest accelerates the exhaust out of the rocket.

The jet power must come from some on-board energy source. The total efficiency, η_T, of a propulsion system is then the fraction of this on-board source power, P_{in}, that is converted into jet power.

$$\eta_T = \frac{P_{jet}}{P_{in}} \tag{2.11}$$

2.4 Electrostatic Propulsion

Electric propulsion is a sub-class of space propulsion that involves accelerating propellant to large exhaust velocities through the use of electrical power [11]. Typically this involves applying either electrostatic or electromagnetic fields to an ionized propellant as the means of acceleration. However, electrothermal thrusters, which operate by electrically heating a gaseous propellant before expanding it through a nozzle, fall into this category as well. Hall thrusters rely on the electrostatic acceleration of a propellant, and so the basic physics of electrostatic propulsion will be discussed here.

2.4.1 Thrust Force of an Electrostatic Thruster

In an electrostatic thruster, ions generated inside the device are accelerated by an applied electrostatic field and fall through some electrostatic potential drop V_b, known as the beam voltage, as they exit. Assuming an ion starts with zero kinetic energy upon its creation, conservation of energy states that its exit velocity after falling through the beam potential is given by

$$v_{ex}^{+Z} = \sqrt{\frac{2(Ze)V_b}{m_i}} \tag{2.12}$$

Here, m_i is the mass of the ion, Z is the charge state of the ion, and e is the charge of an electron (1.602×10^{-19} C).

As derived back in section 2.2, the thrust force on a spacecraft is equal to the mass flow rate of the propellant multiplied by the propellant's exhaust velocity. In an electrostatic thruster, there will be both ions and neutral particles exiting the device, each with their own mass flow rate and exhaust velocity. The total thrust force is then given by

$$F_T = F_T^{+Z} + F_{T,n} = \dot{m}_{i+z} v_{ex}^{+Z} + \dot{m}_n v_n \tag{2.13}$$

where F_T^{+Z} is the ion component of the thrust, $F_{T,n}$ is the neutral component of the thrust, $\dot{m}_{i+z}$ is mass flow rate of ions of charge state Z, $\dot{m}_n$ is the mass flow of neutral particles, and v_n is the exit velocity of the neutrals. Ideally the vast majority of neutral propellant fed into an electrostatic thruster will be ionized, and so the neutral component of the thrust will be negligible.

Since the ion mass flow out of the thruster is electrically charged, it constitutes an electric current known as the beam current. An ion beam current, I^{+Z}, consisting exclusively of ions of charge $+Ze$, is related to the ion mass flow rate via the following expression

$$I^{+Z} = \frac{Ze\dot{m}_{i+Z}}{m_i} \tag{2.14}$$

Using equations 2.12 and 2.14, the thrust force generated by a beam of charge $+Ze$ ions can be written in terms of the beam current and beam voltage.

$$F_T^{+Z} = \dot{m}_{i+Z} v_{ex}^{+Z} = I^{+Z}\sqrt{\frac{2m_i V_b}{Ze}} \tag{2.15}$$

If there are multiple different charged species in the beam, they can be thought of as having their own individual currents (I^{+1}, I^{+2}, I^{+3}...) so that the total beam current is given by

$$I_b = I^{+1} + I^{+2} + I^{+3} + ... \tag{2.16}$$

Each current will contribute additively to the thrust such that the total thrust is

$$F_T = F_T^{+1} + F_T^{+2} + F_T^{+3} ... = I_b\sqrt{\frac{2m_i V_b}{e}} \sum_{i=1}^{N} \frac{f_i}{\sqrt{Z_i}} \tag{2.17}$$

where,

$$f_i = \frac{I^{+i}}{I_b} \tag{2.18}$$

and

$$Z_i = +1, +2, +3, ... \tag{2.19}$$

Similarly, the total ionized mass flow rate exiting the thruster is given by

$$\dot{m}_i = \dot{m}_{i+1} + \dot{m}_{i+2} + \dot{m}_{i+3} + ... = \frac{m_i I_b}{e} \sum_{i=1}^{N} \frac{f_i}{Z_i} \tag{2.20}$$

Equation 2.17 assumed that the ion beam current was unidirectional along the thruster's axis. In general the ion beam current can diverge at the exit plane of the thruster as shown in figure 2.2.

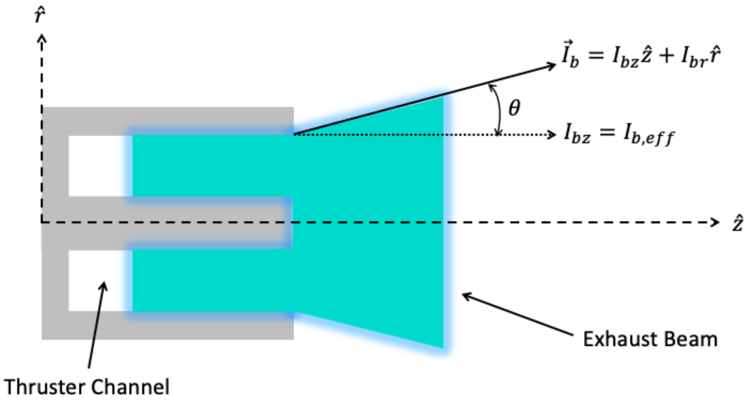

Figure 2.2: A thruster's exhaust beam diverging at the channel exit.

In the above simple case of a cylindrically-shaped thruster with an azimuthally symmetric exhaust beam, the ion beam current at the exit plane can have components in both the axial and radial directions.

$$\vec{I_b} = I_{br}\hat{r} + I_{bz}\hat{z} \tag{2.21}$$

Only the axial component will contribute to thrust, and thus the "effective" beam current is

$$I_{b,eff} = I_{bz} = cos(\theta)|\vec{I_b}| \tag{2.22}$$

The actual thrust will then be reduced by the correction factor $\eta_\theta = cos(\theta)$ where θ is known as the half-angle divergence of the beam [11]. Taking into account this correction factor, the full expression for thrust is then given by

$$F_T = \eta_\theta I_b \sqrt{\frac{2m_i V_b}{e}} \sum_{i=1}^{N} \frac{f_i}{\sqrt{Z_i}} \tag{2.23}$$

2.4.2 Specific Impulse of an Electrostatic Thruster

Equation 2.7 provided a general expression for specific impulse. Assuming both the thrust and the propellant mass flow are are constant in time, this reduces to

$$I_{sp} = \frac{F_T}{\dot{m}_p g} \tag{2.24}$$

Using equation 2.23 for the thrust force, the above equation becomes

$$I_{sp} = \frac{\eta_m \eta_\theta}{g} \sqrt{\frac{2eV_b}{m_i}} \left(\frac{\sum_{i=1}^{N} \frac{f_i}{\sqrt{Z_i}}}{\sum_{i=1}^{N} \frac{f_i}{Z_i}} \right) \tag{2.25}$$

where,

$$\eta_m = \frac{\dot{m}_i}{\dot{m}_p} \tag{2.26}$$

is known as the mass utilization efficiency of the thruster [11]. This quantity represents the fraction of injected neutral propellant that is successfully ionized.

2.4.3 Efficiency of an Electrostatic Thruster

The total efficiency of a generic thruster was given back in equation 2.11. Re-expressing it in terms of thrust yields

$$\eta_T = \frac{F_T^2}{2\dot{m}_p P_{in}} \tag{2.27}$$

Plugging in equation 2.23 for thrust and simplifying results in the following equation for the total efficiency of an electrostatic thruster.

$$\eta_T = \eta_\theta^2 \eta_q \eta_m \frac{I_b V_b}{P_{in}} \tag{2.28}$$

The quantity η_q is known as the charge utilization efficiency of the thruster [5], and it's given by

$$\eta_q = \frac{\left(\sum_{i=1}^{N} \frac{f_i}{\sqrt{Z_i}}\right)^2}{\sum_{i=1}^{N} \frac{f_i}{Z_i}} \tag{2.29}$$

From equations 2.23 and 2.20 we can see that, for a given ion beam current, the thrust and ionized mass flow (and by extension the mass utilization efficiency) would be maximized if the ion beam was purely singly charged ($I_b = I^{+1}$). The charge utilization efficiency is a correction factor that accounts for the reduction of those quantities resulting from the presence of multiply charged ions in the beam.

Chapter 3

THERMIONIC CATHODES

3.1 Thermionic Emission

3.1.1 The Richardson-Dushman Equation

Thermionic emission is a process by which electrons escape from the surface of a heated metal [10]. The amount of energy required for an electron to escape is known as the "work function" of that material. This work function represents the height of the potential energy barrier that the electrons must overcome. Electrons with thermal kinetic energies exceeding the work function will be emitted into free space. Heating a metal increases the average thermal kinetic energy of the unbounded electrons in its material lattice, resulting in a greater number of electrons having energies that exceed the work function. The emitted electron current density from a metal surface, j_{th}, at a given temperature T (in Kelvin), is governed by the Richardson-Dushman equation given below [11].

$$j_{th} = AT^2 e^{-\frac{\phi_o + \alpha T}{kT}} \tag{3.1}$$

Here, A is a constant with the value $120 A/cm^2 K^2$, k is Boltzmann's constant, ϕ_o is the material's work function measured in eV, and α is a second material dependant constant that governs how the work function changes with the material's temperature.

3.1.2 The Shottkey Effect

Equation 3.1 does not account for the effect of an electric field local to the material surface. The presence of an electric field effectively alters the the height of the potential barrier that the material electrons must overcome, and either enhances or reduces the effective work function of the material depending on the direction in which it's pointing. This is known as the Shottkey effect [11]. During the cathode's operation there will always be a local electric field as a result of space charge accumulating near the emitter surface. Any external electric field applied to the cathode will contribute to the net field at the surface as well. The amount by which the work function potential barrier is altered, $\Delta\phi$, is given by Shottkey term below.

$$\Delta\phi = \sqrt{\frac{eE_c}{4\pi\epsilon_0}} \tag{3.2}$$

Here, E_c is the magnitude of the electric field component normal to the surface, evaluated at the cathode surface, and ϵ_0 is the permittivity of free space. For the case in which the normal field component points inwards and assists with electron emission, the modified Richardson-Dushman equation is given by

$$j_{th} = AT^2 e^{-\frac{\phi_o + \alpha T - \Delta\phi}{kT}} \tag{3.3}$$

Here, the Shottkey term is negative, representing the fact that the electric field is working to reduce the material's work function.

3.2 Emissive Materials

As shown in equation 3.3, the emitted current density at a given surface temperature and electric field strength increases exponentially as the material's work function decreases. Therefore, a low work function is an incredibly desirable property for an electron emitter. There are two types of emitters that are commonly used in electric propulsion devices: oxide emitters, and lanthanum hexaboride (LaB_6) emitters [11], both of which will be discussed here.

3.2.1 Oxide Emitters

In an oxide emitter, the main body of the emitter is a porous tungsten matrix that's typically formed by pressing and sintering fine tungsten powder into a solid mass before machining it into the desired shape [8]. Distributed between the pores is a compound consisting of barium oxide (BaO), calcium oxide (CaO), and aluminum oxide (Al_2O_3). This compound is introduced into the tungsten either by blending it as a powder with the tungsten before pressing the entire mixture, or by melting it into an already pressed tungsten base. The chemical formula of the barium-calcium-aluminate impregnate is $x(BaO)y(CaO)z(Al_2O_3)$, where x, y and z are numbers corresponding to the molar ratio of each molecule in the compound [36]. Common molar ratios used in dispenser cathodes are 311, 411, 502, and 532, each yielding a slightly different work function [8]. Table 3.1 showcases the measured work functions of the aforementioned oxide emitters.

Material	ϕ_0	α
Type 311 Oxide	1.67	3.07×10^{-4}
Type 411 Oxide	1.67	2.82×10^{-4}
Type 532 Oxide	1.67	3.17×10^{-4}

Table 3.1: Reported work functions of several different oxide emitters [8].

When the emitter is heated, the impregnated mixture undergoes a chemical reaction with the tungsten which produces gaseous Ba and BaO inside the pores [29]. These gaseous products diffuse through the pores to produce a mono-layer of Ba-O dipoles over the tungsten surface. The electrostatic field produced by the dipole layer aids in reducing the work function of the tungsten from its normally large value of about 4.55eV [11], to around 2eV at typical cathode operating temperatures [6]. Once this dipole layer is established, the cathode is considered "activated".

While operating at emissive temperatures, barium is constantly evaporated from the surface of the emitter [29]. Additionally, if operating in a plasma discharge, ions striking the surface can sputter away the barium mono-layer. When the reservoir of the impregnated compound begins to deplete and can no longer replenish the mono-layer at the same rate that it's being removed, the emitter has reached the end of its life and the work function will increase back to that of pure tungsten.

3.2.2 Oxide Emitter Poisoning

When operating in a gaseous environment, an oxide emitter is at risk of being "poisoned". Emitter poisoning is a process in which gaseous molecules are adsorbed onto the surface of the emitter. This can modify the dipole mono-layer, leading to an increase in the emitter work function [7]. Common gases which can lead to poisoning include oxygen, water vapor, air, and carbon dioxide. For each of these gases, there is a critical partial pressure below which the emitter is safe to operate. For an operating temperature of 1100C, this pressure limit hovers between $10^{-7} - 10^{-6}$ Torr for the gases listed above [7]. Once the pressure limit is exceeded, the emitted current begins to drop dramatically.

Noble gases on their own, such as the xenon used in Hall thrusters, pose no risk to the emitter [12]. However if using a noble gas, it's imperative that it be of extremely high purity, containing only minimal traces of the aforementioned poisonous gases.

3.2.3 Lanthanum Hexaboride Emitters

A more robust alternative to oxide emitters are emitters made from LaB_6. When heated, lanthanum atoms will diffuse through the bulk of the material to the surface where they form a mono-layer. The La atoms at the surface become polarized, resulting in dipole electric field that reduces the work function of the emitter [21]. The work function of LaB_6 has been measured to be around $2.66 + (1.23 \times 10^{-4})T$ [11], which is larger than a typical oxide cathode. Thus, for a given emission current level,

LaB_6 emitters will have to operate at temperatures several hundred degrees higher than their oxide counterparts.

The are several advantages that LaB_6 emitters possess over oxide emitters, which can justify their use despite their poorer emissive properties. First, LaB_6 is more resistant to poisoning. When operating while exposed to the previously mentioned poisonous gases, the critical partial pressure limit for LaB_6 emitters is about two orders of magnitude higher than the limit for oxide emitters ($\sim 10^{-4}$ Torr) [12]. Second, despite its higher operating temperatures, the evaporation rate LaB_6 is comparable to that of BaO from oxide cathodes at emission current density levels of $20A/cm^2$ or less [12]. Additionally, for a given emitter volume, there will be more La atoms in a LaB_6 emitter, than there will be impregnate molecules in an oxide emitter. Thus, LaB_6 emitters will have notably longer lives while operating at the same emission levels.

3.3 Hollow Cathodes

3.3.1 Components of a Hollow Cathode

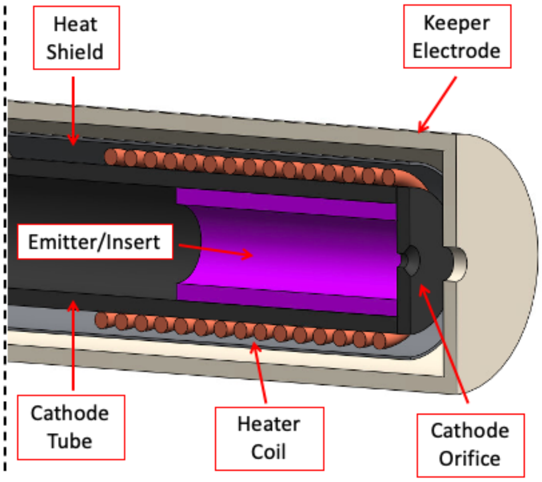

Figure 3.1: Cross section of a generic hollow cathode.

A diagram showcasing the cross-section of a generic hollow cathode is shown in figure 3.1. The main body of the cathode consists of a long tube made from either one of the refractory metals or graphite [37]. The end of the tube is capped off with a plate that has small orifice bored through it to allow the passage of emitted electrons. Internally concentric with the cathode tube is a tubed-shaped ”insert” made from one of the previously discussed, low work function, electron emitting materials. The cathode tube is surrounded by a heater which is used to raise the insert up to the temperatures required for substantial electron emission. The heating element is typically a coil made from a refractory metal wire wrapped about the the cathode tube and is connected to the cathode's heater supply [27]. The entire system is then wrapped in a heat shield in order to reduce the radiative power losses the cathode would incur while heated. The final component is a cylindrical electrode known as the ”keeper electrode” [11]. The keeper is insulated from, and lies concentric with, the entire system. The keeper also has its own orifice through which electrons can exit.

3.3.2 Working Principals of a Hollow Cathode

During start up, the cathode's heater supply is turned on and current is supplied to the heating element. The restively generated heat is then conducted through the cathode tube to the insert, raising it to emissive temperatures. The keeper is then biased positively with respect to the cathode body by a voltage V_{keep} so it can draw the emitted electrons out through the orifice plate. Neutral propellant gas is then fed into the base of the cathode tube. The propellant molecules are ionized via collisions with the emitted electrons, resulting in the formation of a plasma between the insert and the keeper as showcased in figure 3.2.

Usually hollow cathodes are operated in conjunction with an external anode, with the purpose of generating an anode-to-cathode discharge. Once the cathode-keeper discharge is ignited, a voltage V_d is then applied between the anode and cathode to

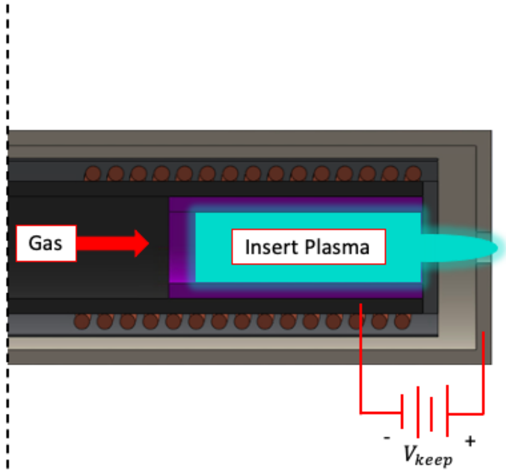

Figure 3.2: The cathode-keeper discharge inside a hollow cathode.

draw electrons out through the keeper into the main discharge. This configuration is shown in figure 3.3. This discharge voltage is usually sufficient to maintain the insert plasma, and so in steady state operation the keeper voltage is typically turned off [11]. If at any point the main discharge is disrupted, the keeper electrode can used to either maintain or re-ignite the insert plasma.

The insert plasma serves two important functions in a hollow cathode. Due to the small orifice restricting particle flow, the plasma and neutral densities in the insert region tend to be vary large, with plasma densities in excess of $10^{20} m^{-3}$ found in typical hollow cathodes [11]. Meanwhile the electron temperature in this plasma is usually quite low, only around a few eV. As will be discussed in a later section, these plasma conditions are optimal for alleviating space charge issues at the emitter surface. Additionally, electrons and ions from the insert plasma that strike the emitter surface transfer energy to it providing an extra source of heating. This heating is typically sufficient to maintain the insert temperature on its own [11]. Therefore, in steady state operation, once the discharge is ignited, the cathode's heating supply can be turned off as well.

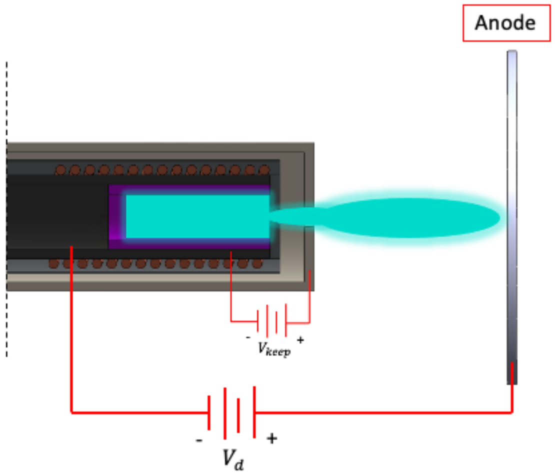

Figure 3.3: The plasma discharge between a hollow cathode and an external anode.

3.4 Planar Cathodes

In accordance with it's name, a planar cathode is characterized by its emitter having a planar surface. Aside from the emitter, the only other components necessary for operation are a heating element, electrical insulation for the heating element, and the infrastructure necessary to hold these components together. For the purposes of this thesis, the design used for the dispenser cathodes developed and sold by HeatWave Labs [19] will act the paradigmatic planar cathode design. A CAD model of their cathode is showcased in figure 3.4.

In this design, a disk-shaped emitter is connected to a thin-walled cylindrical shell made of some refractory metal. Interior to the shell is a solid cylindrical block of ceramic material. Encased within the ceramic is the heating coil. The purpose of the ceramic is to both electrically isolate the heater coil from the molybdenum body, and provide a conductive path for the heat generated by the coil to reach the emitter.

The operational principals of this type of cathode are far simpler than a hollow cathode. Electrical current is supplied to the heating coil to restively heat it. Heat from the coil is then conducted through the ceramic to the emitter in order to bring it

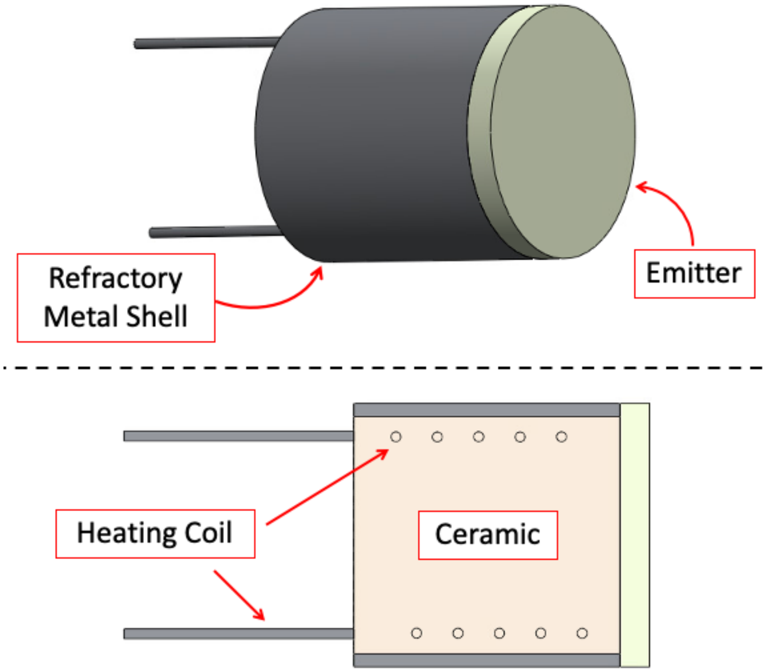

Figure 3.4: CAD model of the planar cathodes developed by HeatWave Labs.

up to the desired operating temperature. This type of cathode requires no additional propellant gas to be fed to it as part of its ignition process. However, due to its geometry, it lacks any mechanism to self heat and will require continuous heating power in order to sustain its emission. One thing to note, is that if a planar cathode is operated in an external plasma discharge, the plasma can provide heating, lowering the amount of power necessary to maintain its operating temperature.

Chapter 4

PHYSICS OF HALL THRUSTERS

4.1 Working Principals of a Hall Thruster

A diagram depicting the cross section of a generic Hall thruster is shown in figure 4.1.

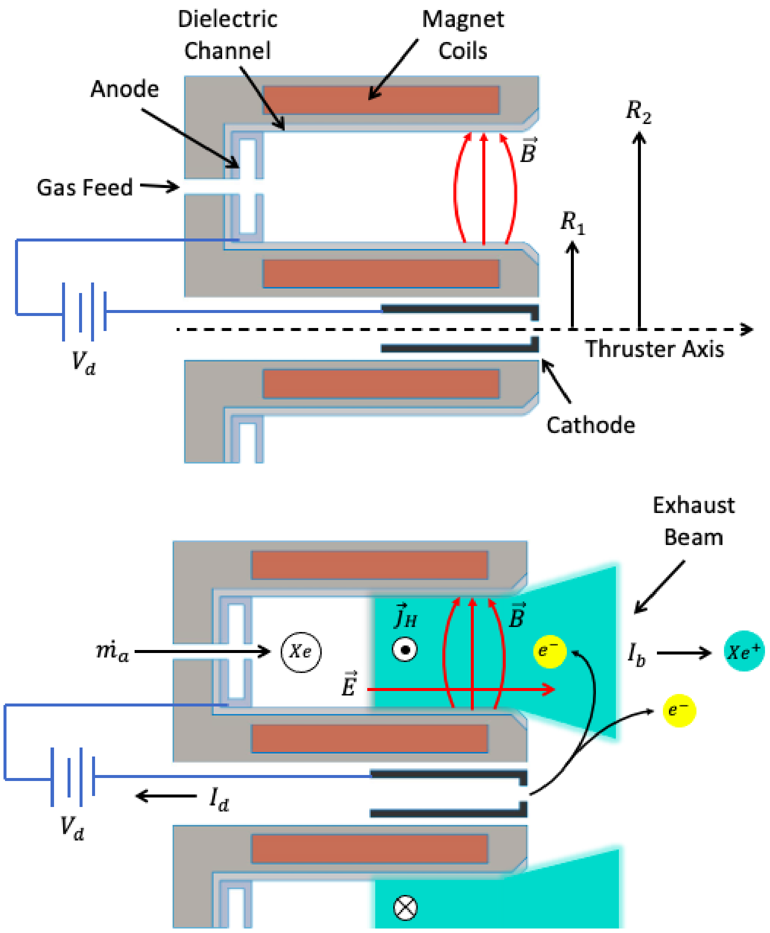

Figure 4.1: A cross section of a generic Hall thruster. The second diagram depicts the Hall thruster during operation.

The main body of a Hall thruster consists of two co-axial cylinders made from some dielectric material that together form the thruster's channel [3]. Common choices for the channel wall material include boron nitride (BN) and boroil (BN-SiO$_2$) [11]. In the diagram above, the inner channel has a radius R_1 and the outer channel has a radius R_2, yielding a mean channel diameter $D = (R_1 + R_2)$, a channel width $W = R_2 - R_1$, and a cross-sectional channel area $A_{ch} = \pi(R_2^2 - R_1^2) = \pi DW$. It's within this channel that the thruster plasma is generated and the electrostatic ion acceleration takes place.

At the base of the channel is a metallic ring-shaped anode [11]. The anode is typically designed with holes evenly distributed around its circumference which connect to the thruster's gas feed system. During operation, neutral propellant gas, typically xenon, is fed through these holes at some mass flow rate $\dot{m}_a$.

Placed external to the channel, either center-mounted along the thruster's axis (depicted above), or mounted at some radial position outside the thruster body, is a thermionic cathode. The thruster's discharge power supply is connected between the anode and cathode. During operation, the cathode is heated to induce the thermionic emission of electrons. The anode is biased positively with respect to the cathode by the discharge voltage V_d, in order to draw the emitted electrons into the channel. The net current that flows between the anode and cathode is the discharge current I_d, making the power consumed by the discharge supply $P_d = I_d V_d$.

The thruster's magnetic circuit creates an axisymmetric, and predominately radial (pointing from the inner wall to the outer wall) magnetic field within the channel. The magnetic circuit is typically designed such that the field strength peaks near the channel exit, and drops off significantly moving towards the anode. As an example, figure 4.2a shows the radial component of the magnetic field, normalized by its peak value, plotted as a function of the axial position along the thruster channel for EDB Fakel's SPT-100M Hall thruster. Showcased next to it in figure 4.2b is the magnetic field line topology for the same thruster. The purpose of the magnetic field is to

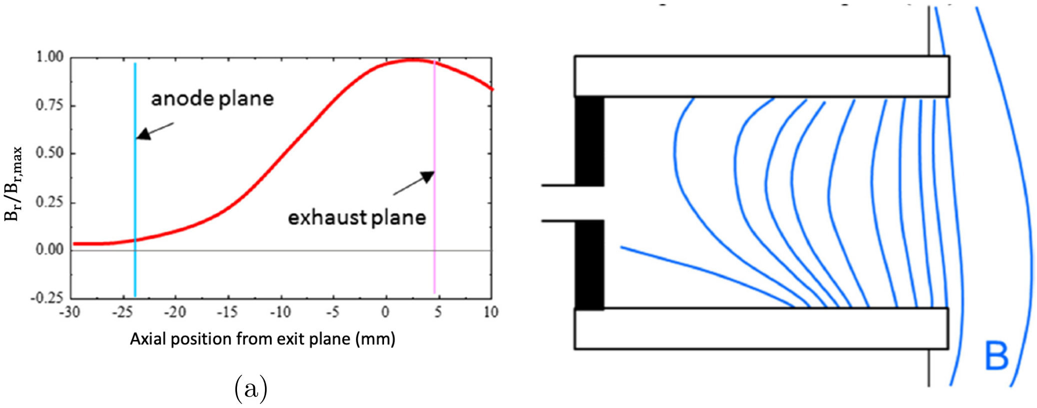

(a)

(b)

Figure 4.2: (a) Axial distribution of the (normalized) radial magnetic field strength inside the SPT-100M Hall thruser. (b) Magnetic field line topology of the same thruster [3].

restrict the axial motion of the plasma electrons, while leaving ions unhindered [11].

As soon as they enter the channel the emitted electrons encounter the primarily radial magnetic field, which, in combination with the predominantly axial electric field produced by the discharge supply, forces the electrons to drift in the $\vec{E} \times \vec{B}$ azimuthal direction. The resulting azumthal electron current is refereed to as the Hall current [11]. This is depicted as out of the page in figure 4.1. The electrons will spiral helically along the magnetic field lines, bouncing back and forth between the channel walls due to repulsion by the wall sheaths, while at the same time drifting azimuthally about the thruster's axis. The presence of the radial magnetic field also reduces the axial mobility of the electrons, increasing their residence time in the downstream end of the channel.

Neutral gas atoms that collide with the circulating electrons are ionized, and then accelerated out of the thruster channel by the local electric field. The result is an ion beam current, I_b, crossing the channel exit plane. As the ions are being accelerated through the channel, they exert an electrostatic force on the magnetized, circulating electrons. This force is then transferred through the magnetic field to the Hall thruster's magnetic circuit, providing thrust [11].

4.2 Potential Distribution in a Hall Thruster

As mentioned in the previous section, a DC voltage V_d is applied between the thruster's anode and cathode. However, due to the presence of the magnetic field, the way in which the electric potential is distributed across the plasma differs from a standard DC discharge.

Figure 4.3 showcases the axial electric potential distribution inside a typical Hall thruster's channel. In a Hall thruster's "cross-field" discharge, the bulk of the anode-to-cathode potential drop occurs near the channel exit where the magnetic field strength is the largest. This location is known as the "acceleration region" [11]. A strong potential gradient, and thus electric field, is able to be sustained within the quasi-neutral plasma here as a result of reduced axial conductivity of the electrons [3]. This can be thought of as similar to the potential drop across a resistor in a circuit. The plasma near the anode will be close to the anode potential as the magnetic field is weak and the axial electron mobility is mostly unhindered [11].

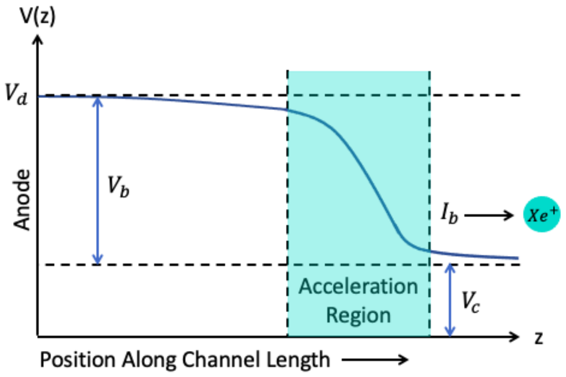

Figure 4.3: Axial electric potential distribution inside a typical Hall thruster's channel.

Not all of the discharge voltage drop occurs within the acceleration region however.

The potential drop that exists between the anode and the ion beam plasma is known as the beam voltage, V_b. This is the voltage drop through which ions generated in channel are accelerated through. The ratio of the thruster's beam voltage to the applied discharge voltage is known as the voltage utilization efficiency, η_v [11].

$$\eta_v = \frac{V_b}{V_d} \tag{4.1}$$

This quantity can be thought of as the fraction of the applied discharge voltage that becomes "useful" accelerating ion voltage.

The remaining potential drop, which exists between the ion beam plasma and the cathode, is known as the coupling voltage, V_{cc} [11]. The discharge voltage is then simply the sum of the beam and coupling voltages.

$$V_d = V_b + V_{cc} \tag{4.2}$$

4.3 Hall Thruster Efficiency

The total efficiency of a generic electrostatic thruster was given back in equation 2.28. For a Hall thruster specifically, there are a few more loss terms to consider.

If the Hall thruster employs a hollow cathode, it will require its own mass flow rate, $\dot{m}_c$. The total propellant flow rate is then the sum of the cathode mass flow rate, and the mass flow rate through the anode.

$$\dot{m}_p = \dot{m}_c + \dot{m}_a \tag{4.3}$$

While the mass flow through the hollow cathode is necessary for its operation, it still represents a loss of efficiency as those propellant molecules are not being converted into beam ions. A Hall thruster's cathode efficiency, η_c, is then defined as the ratio of the anode mass flow rate, to the total mass flow rate [11].

$$\eta_c = \frac{\dot{m}_a}{\dot{m}_p} \tag{4.4}$$

The previous section discussed a quantity called the voltage utilization efficiency. In a similar vein, the thruster's current utilization efficiency is defined as the ratio of the ion beam current to the total discharge current [11].

$$\eta_b = \frac{I_b}{I_d} \tag{4.5}$$

P_{in} is the total electrical power used to operate a Hall thruster. Aside from the previously discussed discharge power, there are several other contributors to this term. If the thruster's magnetic circuit is employing electromagnets, it will require an additional power supply consuming some power P_{mag}. The cathode's heater may require a power P_{heat} to maintain the temperatures necessary for sufficient electron emission. Lastly, if the thruster is using a hollow cathode, its keeper electrode will consume a power P_{keep} while it's in use. In general, the total input power is given by

$$P_{in} = P_d + P_{mag} + P_{heat} + P_{keeper} \tag{4.6}$$

Of the terms listed in equation 4.6, only the discharge power is providing energy directly to the thruster's plasma. It's this power that's partially converted into the power of the ion beam. Thus the other power terms are, from an efficiency standpoint, "wasted". The thruster's electrical efficiency, n_0, is then defined as the ratio of the discharge power to the total input power [11].

$$\eta_0 = \frac{P_d}{P_{in}} \tag{4.7}$$

Combining equations 2.28, 4.1, 4.4, 4.5, and 4.7, the total efficiency of a Hall thruster can be expressed as

$$\eta_T = \eta_\theta^2 \eta_q \eta_{ma} \eta_b \eta_v \eta_c \eta_0 \tag{4.8}$$

In the above equation, η_{ma} is defined as the the ratio of the total ion mass flow rate exiting the channel, to the anode mass flow rate entering the channel.

Chapter 5

PLANAR CATHODE EFFICIENCY MODEL

5.1 Comparison of Cathode Efficiencies

5.1.1 The Anode Efficiency

The total efficiency of a Hall thruster was given by equation 4.8 where it was shown to be the product of seven individual efficiency terms, each describing a different aspect of the thruster's performance. A detailed comparison between hollow and planar cathodes, and their influence on total efficiency, would normally require analyzing how each individual term depends on which cathode type is installed. To make this problem more tractable, a major simplifying assumption will be discussed in this section.

The first five terms in the total thruster efficiency equation are collectively referred to as the anode efficiency, η_a [11].

$$\eta_a = \eta_\theta^2 \eta_{ma} \eta_q \eta_b \eta_v \tag{5.1}$$

The first assumption of the the model will be that the anode efficiency is completely independent of which electron source is equipped external to the channel. That is, taking any given Hall thruster, but switching the hollow cathode for a planar cathode, will not change the properties of the discharge, provided that the thruster is operated with the same discharge voltage, discharge current, anode mass flow rate, magnetic field topology, etc... Thus, for the purposes of comparing the two cathode types, only differences in the product of the cathode and electrical efficiencies, $\eta_c \eta_0$, need be analyzed.

5.1.2 $(\eta_c \eta_0)_{hollow}$

As mentioned section 2.3, a hollow cathode requires no heater or keeper power during steady state operation. Thus those two quantities are set to zero in the electrical efficiency term. A hollow cathode does however require a constant mass flow through its interior. This amount is typically 7-10% of the mass flow injected into the anode [28]. As a result, $\eta_c \eta_0$ for a Hall thruster employing a hollow cathode is given by

$$(\eta_c \eta_0)_{hollow} = \left(\frac{\dot{m}_a}{\dot{m}_a + \dot{m}_c}\right)\left(\frac{P_d}{P_d + P_{mag}}\right) = \left(\frac{\dot{m}_a}{\dot{m}_a + \dot{m}_c}\right)\left(\frac{1}{1 + \eta_{mag}}\right) \tag{5.2}$$

where,

$$\eta_{mag} = \frac{P_{mag}}{P_d} \tag{5.3}$$

5.1.3 $(\eta_c \eta_0)_{planar}$

Unlike hollow cathodes, planar cathodes do not have the benefit of a dense interior plasma to provide reliable heating to their emitters. However when equipped to a Hall thruster, the planar cathode's emitter will be exposed to the plasma produced by the thruster. This will either the plume or channel region plasma, depending on where the planar cathode is placed. This plasma will assist in heating the planar emitter, but for the purposes of model the cathode will still be assumed to require some external heating power to maintain the desired operating temperatures. Thus the P_{heat} term cannot be neglected. On the other hand, planar cathodes require no additional propellant to operate and so the cathode efficiency term is always unity. As a result, $\eta_c \eta_0$ for a Hall thruster employing a planar cathode is given by

$$(\eta_c \eta_0)_{planar} = \frac{1}{1 + \eta_{mag} + \frac{P_{heat}}{P_d}} \tag{5.4}$$

5.1.4 $(\eta_c\eta_0)_{hollow}$ *vs* $(\eta_c\eta_0)_{planar}$

In figure 5.1 below, $(\eta_c\eta_0)_{hollow}$ and $(\eta_c\eta_0)_{planar}$ are both plotted as functions of P_{heat}/P_d. For the purposes of this plot, the values 0.011 and 0.935 were chosen for η_{mag} and $\eta_{c,hollow}$ respectively. These values correspond to one of the operating points of the H9 Hall thruster [15]. It's also assumed the magnet power is independent of the cathode type and the same value is used in each function.

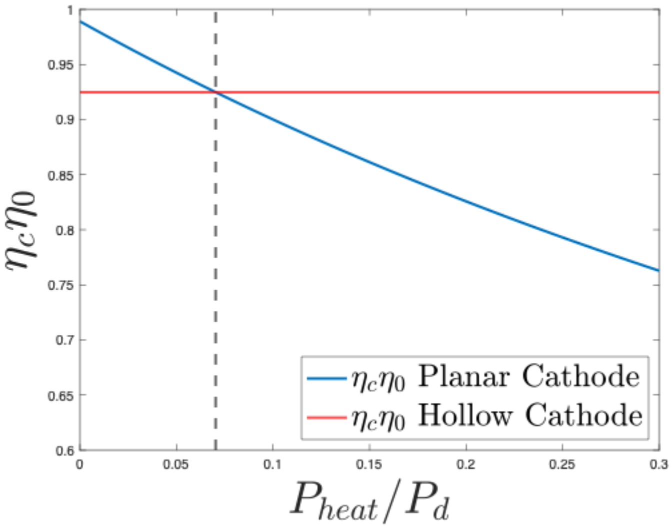

Figure 5.1: Plot of $(\eta_c\eta_0)_{hollow}$ and $(\eta_c\eta_0)_{planar}$ as functions of P_{heat}/P_d.

Since $(\eta_c\eta_0)_{hollow}$ has no dependence on P_{heat}, it's simply a horizontal line representing the value of $\eta_c\eta_0$ which the planar cathode must beat. Meanwhile $(\eta_c\eta_0)_{planar}$ is inversely proportional to P_{heat}/P_d and trends downwards as this ratio is increased.

From figure 5.1 it can be clearly observed that for given values of η_{mag} and $\eta_{c,hollow}$, there is a critical value of P_{heat}/P_d below which the planar cathode equipped-thruster would have a higher total efficiency. In this particular example, that critical value is around 0.07. In practice however, the heating power for a planar cathode cannot be made some arbitrarily small fraction of the thruster's discharge power. Based on the desired thruster operating conditions, the planar cathode will be required to provide some discharge current at some discharge voltage, which will in turn determine the required heating power for that operational state. Thus, in order to identify an operational regime where the planar cathode may yield a greater thruster efficiency than a hollow cathode, it's first necessary to determine P_{heat} as a function of discharge power.

5.2 Additional Benefits of Planar Cathodes

Before moving on to calculating P_{heat}, it's important to note that, outside of the possible gains in total thruster efficiency, there are other advantages planar cathodes have in terms of thruster performance.

Using the definitions of η_c and η_{ma} in conjunction with equation 2.25, the specific impulse of a Hall thruster can be written as

$$I_{sp} = \frac{\eta_c \eta_{ma} \eta_\theta}{g} \sqrt{\frac{2e\eta_v V_d}{m_i}} \left(\frac{\sum_{i=1}^{N} \frac{f_i}{\sqrt{Z_i}}}{\sum_{i=1}^{N} \frac{f_i}{Z_i}} \right) \tag{5.5}$$

Assuming η_{ma}, η_θ, η_q and η_v remain constant, switching to a planar cathode will always increase the specific impulse of a Hall thruster at a given discharge voltage level since $\eta_{c,planar} = 1$.

Hollow cathodes require their own gas delivery and mass flow control system, something planar cathodes will not need. Additionally, planar cathode's will not need a keeper power supply. Thus, the dry mass of a planar cathode-equipped Hall thruster can potentially be lower, provided that the mass of the planar cathode and its support structure isn't significantly larger than the mass hollow cathode and its corresponding support structure.

5.3 The Plasma Sheath in front of a Planar Emissive Surface

As with any boundary in contact with a plasma, a sheath will at the surface of a planar cathode once the thruster's discharge is ignited. The properties of the bulk plasma, and the plasma sheath, determine how much heat is transferred from the plasma to cathode's emitter. Any power lost by the cathode during operation, that's not compensated for by the plasma, must be provided by the cathode's heating supply. Thus, to quantify the heating power necessary to produce a given discharge current, it's necessary to analyze the physics of this sheath.

The sheath that forms adjacent to a thermionic emitter differs substantially from that which forms next to a non-emissive boundary due to the presence of the thermionically emitted electrons. Treating the emissive sheath in its most complete form, taking into account the three-dimensional nature of the problem, and phenomenon like inter-particle collisions, is highly mathematically complex. To mathematics more tractable, a simple, one-dimensional, collision-less model of an emissive sheath, first derived by Prewtt and Allen [30], is presented in this section.

5.3.1 Emissive Sheath Model

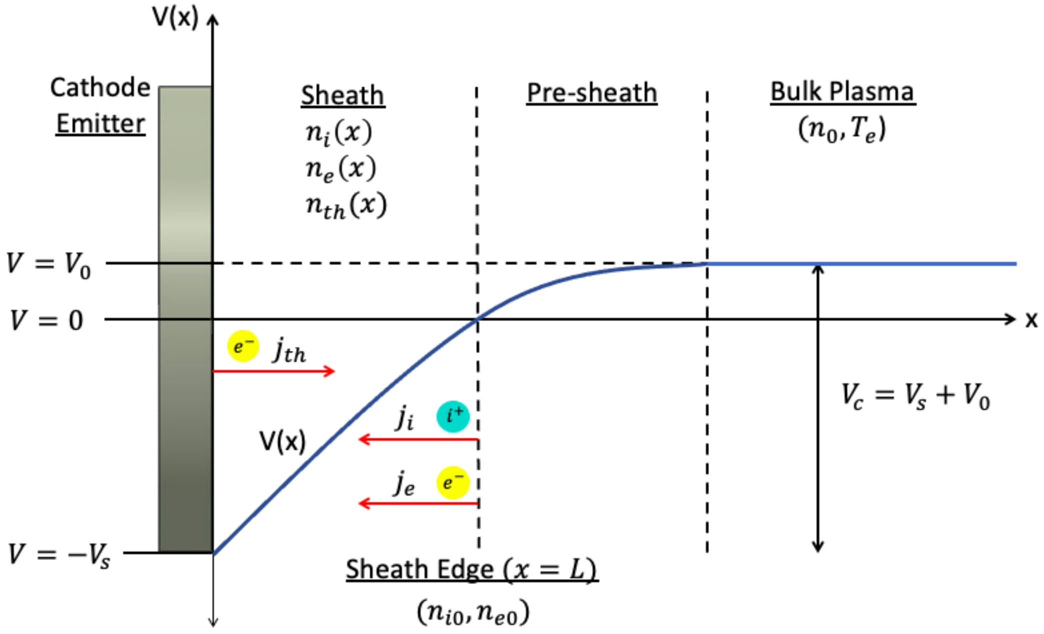

Figure 5.2: Diagram of the one-dimensional sheath in front of a planar cathode.

A diagram of the one-dimensional, emissive sheath is show in figure 5.2. The cathode surface is modeled as an infinite plane located at x = 0, and is held at a potential $-V_s$ relative to the sheath edge located at some position $x = L$. Similar to the sheath in front of a non-emissive boundary, there will be a pre-sheath region with a pre-sheath potential drop V_0, that separates the sheath edge from the bulk plasma. The total potential drop between the bulk of the plasma and the cathode surface, V_c, is then given by

$$V_c = V_s + V_0 \tag{5.6}$$

The electrical potential inside the sheath, $V(x)$, is assumed to monotonically increase from $-V_s$ at the wall to positive V_0 in the bulk of the plasma. The cathode surface is constantly emitting a beam of thermionic electrons with a current density j_{th}. At the same time, the plasma sends electron and ion current densities, j_e and j_i, to the cathode surface. In total, there are three populations of particles inside the sheath: emitted electrons, plasma ions, and plasma electrons, with densities $n_{th}(x)$, $n_i(x)$, and $n_e(x)$ respectively. Lastly, the bulk plasma is assumed to be quasi-neutral with a density n_0, and an electron temperature T_e.

Under the assumptions of the model, the simplified continuity and momentum equations for an arbitrary fluid of species α are written below.

$$n_\alpha u_\alpha = constant \tag{5.7}$$

$$n_\alpha m_\alpha u_\alpha \frac{du_\alpha}{dx} = -n_\alpha q_\alpha \frac{dV}{dx} - \frac{d}{dx}\left(n_\alpha k T_\alpha\right) \tag{5.8}$$

Here, u_α is the average velocity of species α, n_α is the density of species α, T_α is the temperature of species α, and m_α is the mass of a type α particle. These two equations will be solved inside the sheath to determine $n_{th}(x)$, $n_i(x)$, and $n_e(x)$.

5.3.2 Thermionically Emitted Electrons

The first species to consider are the thermionically emitted electrons. These electrons are assumed to possess no thermal kinetic energy upon emission, and thus the fluid of emitted electrons is modeled as cold ($T_{th} = 0$). Under this assumption, the emitted electron momentum equation is given by

$$m_e u_{th} \frac{du_{th}}{dx} = e \frac{dV}{dx} \tag{5.9}$$

The above equation can be integrated from the emitter face at $x = 0$, to a plane in the sheath located at some position x, to yield

$$\frac{1}{2}[u_{th}^2(x) - u_{th}^2(0)] = \frac{e}{m_e}[V(x) - V(0)] \tag{5.10}$$

Since the emitted electrons are cold, their velocity at the cathode surface, before any electrostatic acceleration takes place, is zero. That is, $u_{th}(0) = 0$. Noting that $V(0) = -V_s$, the velocity of the emitted electrons as a function of position inside the sheath is then given by

$$\frac{1}{2} m_e u_{th}^2(x) = e[V_s + V(x)] \tag{5.11}$$

Using equation 5.7, the density of emitted electrons can be related directly to the emitted current density.

$$n_{th}(x) u_{th}(x) = \frac{j_{th}}{e} \tag{5.12}$$

Combing equations 5.11 and 5.12 results in the following equation for the density of the emitted electrons inside the sheath.

$$n_{th}(x) = \frac{j_{th}}{e} \left(\frac{m_e}{2e}\right)^{1/2} [V_s + V(x)]^{-1/2} \tag{5.13}$$

5.3.3 Plasma Ions

The second species to consider are the singly charged plasma ions that enter from the sheath edge at $x = L$ and stream towards the cathode. These ions are similarly approximated as cold and thus $T_i = 0$. The momentum equation for the ion fluid is then given by

$$m_i u_i \frac{du_i}{dx} = -e\frac{dV}{dx} \tag{5.14}$$

The above equation can be integrated from the sheath edge at $x = L$ to some point x inside the sheath, yielding

$$\frac{1}{2}m_i u_i(x)^2 - \frac{1}{2}m_i u_i(L)^2 = -e[V(x) - V(L)] \tag{5.15}$$

The second term on the left hand side represents the kinetic energy of the ions entering the sheath. The ions here are assumed fall through the pre-sheath potential drop before reaching the sheath edge, imparting them with an initial kinetic energy $eV_0 = \frac{1}{2}m_i u_i(L)^2$.

The continuity equation for the plasma ions is written as

$$n_i(x)u_i(x) = n_{i0}u_{i0} \tag{5.16}$$

where $n_{i0} = n_i(L)$ and $u_{i0} = u_i(L)$ are the ion density and velocity at the sheath edge respectively. Combining equations 5.15 and 5.16, and noting that $V(L) = 0$, results in the following equation for the ion density inside the sheath.

$$n_i(x) = n_{i0}\left[1 - \frac{V(x)}{V_0}\right]^{-1/2} \tag{5.17}$$

5.3.4 Plasma Electrons

Lastly, a population plasma electrons will penetrate into the sheath and contribute to the total charge density. The plasma electrons are assumed to be in a state of thermodynamic equilibrium with a uniform temperature T_e. Thus their distribution function is given by

$$f_e(x, v) = n_{e0} \left(\frac{m_e}{2\pi k T_e} \right)^{3/2} exp \left[- \frac{\frac{1}{2} m_e v^2 - eV(x)}{kT_e} \right] \tag{5.18}$$

where $n_{e0} = n_e(L)$ is the plasma electron density at the sheath edge. The electron density inside the sheath can be found by integrating this distribution function over all of velocity space.

$$n_e(x) = \int_{-\infty}^{\infty} \int_{-\infty}^{\infty} \int_{-\infty}^{\infty} f_e(x, v) dv_x dv_y dv_z \tag{5.19}$$

Evaluating this integral yields

$$n_e(x) = n_{e0} exp \left[\frac{eV(x)}{kT_e} \right] \tag{5.20}$$

Similarly, the plasma electron density at the sheath edge can be related to the bulk plasma density in a similar manner through equation 5.21 below.

$$n_{e0} = n_0 exp \left[\frac{-eV_0}{kT_e} \right] \tag{5.21}$$

5.3.5 Boundary Conditions

Now that expressions for the particle densities have been derived, boundary conditions can be applied to the sheath edge to derive algebraic equations for the other plasma variables of interest.

The total charge density inside the sheath, $\rho_T(x)$, is given by

$$\rho_T(x) = en_i(x) - en_{th}(x) - en_e(x) \tag{5.22}$$

Assuming quasi-neutrality is maintained from the bulk plasma up until the sheath edge, then the macroscopic charge density at the sheath edge, $\rho_T(L)$, is zero. Evaluating equation 5.22 at $x = L$ yields the following expression relating the species' densities at the sheath edge

$$n_{i0} - \frac{j_{th}}{e}\left(\frac{m_e}{2eV_s}\right)^{1/2} - n_{e0} = 0 \tag{5.23}$$

Poisson's equation inside the sheath is given by

$$\epsilon_0 \frac{d^2V}{dx^2} = -\rho_T(x) \tag{5.24}$$

Focusing on the region right near the sheath edge where $|V(x)| << kT_e/e$, V_s and V_0, the individual densities can be expanded out as follows:

$$n_i(x) \approx n_{i0}\left[1 + \frac{V(x)}{2V_0}\right] \tag{5.25}$$

$$n_{th}(x) \approx \frac{j_{th}}{e}\left(\frac{m_e}{2eV_s}\right)^{1/2}\left[1 - \frac{V(x)}{2V_s}\right] \tag{5.26}$$

$$n_e(x) \approx n_{e0}\left[1 + \frac{eV(x)}{kT_e}\right] \tag{5.27}$$

Specifically in this region, Poisson's equation can be approximated as

$$\epsilon_0 \frac{d^2V}{dx^2} = -eV(x)\left[n_{i0}\frac{1}{2V_0} + \frac{j_{th}}{e}\left(\frac{m_e}{2eV_s}\right)^{1/2}\frac{1}{2V_s} - n_{e0}\frac{e}{kT_e}\right] \tag{5.28}$$

To have a monotonically decreasing sheath potential, V(x) must be concave down at the sheath edge. Therefore, the right-hand side of equation 5.28 must be negative.

This is satisfied if

$$V_0 \geq \left(\frac{kT_e}{2e}\right)\left(\frac{n_{i0}}{n_{e0}}\right)\left(1 - \frac{j_{th}}{en_{e0}\left(\frac{kT_e}{m_e}\right)^{1/2}\left(\frac{2eV_s}{kT_e}\right)^{3/2}}\right)^{-1} \tag{5.29}$$

Equation 5.29 represents a modification of the Bohm criterion due to the presence of the emitted electrons. If $j_{th} = 0$, equation 5.23 yields $n_{i0} = n_{e0}$, and equation 5.29 then reduces to the original Bohm criterion.

Lastly, electric field at the sheath edge is approximated as zero. Multiplying both sides of Poisson's equation by dV/dx and integrating from the sheath edge, while taking $E(L) = 0$, yields the following equation for the electric field inside the sheath.

$$\frac{\epsilon_0}{2}E^2(x) = 2en_{i0}V_0\left[\left(1 - \frac{V(x)}{V_0}\right)^{1/2} - 1\right] + n_{e0}kT_e\left[exp\left(\frac{eV(x)}{kT_e}\right) - 1\right] \tag{5.30}$$

$$+2j_{th}\left(\frac{m_e}{2e}\right)^{1/2}\left\{[V_s + V(x)]^{1/2} - V_s^{1/2}\right\}$$

Of greater interest is the electric field at the cathode surface, E_c, since this quantity is used in calculating the Shottkey term. This is imply found by evaluating equation 5.30 at $x = 0$ where $V(x) = -V_s$.

$$\frac{\epsilon_0}{2}E_c^2 = 2en_{i0}V_0\left[\left(1 + \frac{V_s}{V_0}\right)^{1/2} - 1\right] + n_{e0}kT_e\left[exp\left(-\frac{eV_s}{kT_e}\right) - 1\right] \tag{5.31}$$

$$-2j_{th}\left(\frac{m_eV_s}{2e}\right)^{1/2}$$

Referring back to section 3.1.2, the emitted current density, j_{th}, can be related to the surface temperature of the cathode, T, the material properties of the cathode, and the electric field at the cathode surface through equation 3.3. Thus, for a desired value of j_{th}, if the cathode's work function, the bulk plasma's density and temperature, and the total sheath potential drop (V_c) are known, then 5.23, 5.29, 5.31, 5.21, 3.3 and 5.6 provide a system of six, non-linear, algebraic equations that can be solved to find the surface temperature required to produce j_{th}, along with the sheath variables n_{i0}, n_{e0}, V_0, V_s, and E_c.

Once the aforementioned six variables are known, both the power lost by the cathode while emitting j_{th}, and the power transferred to it from the plasma, can be calculated. The difference between these powers is the heating power, P_{heat}, required to sustain j_{th}. The process of calculating these power terms is outlined in the following section.

5.4 Calculation of P_{heat}

5.4.1 Cathode Power Losses

While the cathode is operating at emissive temperatures, the emitter will be constantly radiating energy. The total electromagnetic power radiated off a surface at temperature T is given by the Stephan-Boltzmann law [34].

$$P_{rad} = A_c \sigma \epsilon T^4 \tag{5.32}$$

Here, ϵ is the emissivity of the emitting material, σ is the Stephan-Bolztmann constant defined as $5.67 \times 10^{-8} W/m^2K^4$, and A_c is the emitting surface area measured in square-meters.

There is also a power loss associated with the emission of electrons. The energy required to remove an electron from the cathode is equal to its charge multiplied by the total work function of the emitter. That is,

$$\text{Energy loss per emitted electron} = e\phi_t \tag{5.33}$$

where ϕ_t is the total work function, including the Shottkey term.

$$\phi_t = \phi_0 + \alpha T - \Delta\phi \tag{5.34}$$

Consequently, equation 5.34 is the energy lost by the cathode per emitted electron. The power lost by the cathode while emitting a current I_{th} is then

$$P_{emit} = I_{th}\phi_t \tag{5.35}$$

5.4.2 Plasma Ion heating

Once n_{i0} and V_0 are obtained by solving the sheath equations, the back-streaming ion current across the sheath can be calculated from equation 5.36 below.

$$I_i = eA_c n_{i0} u_{i0} = eA_c n_{i0} \left(\frac{2eV_0}{m_i}\right)^{1/2} \tag{5.36}$$

Here, m_i, the atomic mass of the ion species. Since the ion fluid inside the sheath and pre-sheath regions was modeled as singly-charged, cold, and collision-less, every single plasma ion will just fall through the full sheath potential and arrive at the emitter surface with a kinetic energy eV_c. Upon colliding with the surface, it's assumed that the ions completely give up their kinetic energy to the emitter.

It's also assumed that upon reaching the emitter every ion recombines with an electron at the surface. Recombination is an exothermic process which releases an energy equal to eU_i^+, where U_i^+ is the first ionization potential of the ion species measured in electron-volts. However the recombination process also removes an electron and an energy $e\phi_t$ from the emitter. The total energy per ion transferred to the emitter is then given by

$$\text{Energy transferred per plasma ion} = e(V_c + U_i^+ - \phi_t) \tag{5.37}$$

The total power delivered by the plasma ions to the cathode, P_i, is simply the product of the number of ions per second striking the surface, and the energy per ion.

$$P_i = I_i(V_c + U_i^+ - \phi_t) \tag{5.38}$$

5.4.3 Plasma Electron heating

For Maxwellian plasma electrons, the flux of electron kinetic energy in the x-direction (towards the sheath) is given by

$$\Gamma_{e,KE}(x) = n_0 < \frac{1}{2}m_e v^2 v_x >_e = \int_0^\infty \int_{-\infty}^\infty \int_{-\infty}^\infty \frac{1}{2}m_e v^2 v_x f_e(x,v) dv_x dv_y dv_z \tag{5.39}$$

Evaluating the above integral yields

$$\Gamma_{e,KE}(x) = n_0 \left(\frac{kT_e}{2\pi m_e}\right)^{1/2} exp\left[\frac{eV(x)}{kT_e}\right](2kT_e) \tag{5.40}$$

The flux of electron kinetic energy crossing the emitter surface at $x = 0$ is then

$$\Gamma_{e,KE}(0) = n_0 \left(\frac{kT_e}{2\pi m_e}\right)^{1/2} exp\left(\frac{-eV_c}{kT_e}\right)(2kT_e) \tag{5.41}$$

The total electron kinetic energy crossing the emitter surface every second is thus given by

$$P_{e,S} = I_e \left(\frac{2kT_e}{e}\right) \tag{5.42}$$

where,

$$I_e = en_0 \left(\frac{kT_e}{2\pi m_e}\right)^{1/2} exp\left(\frac{-eV_c}{kT_e}\right) A_c \tag{5.43}$$

is the plasma electron current reaching the emitter. According to equation 5.42, the average kinetic energy per electron reaching the emitter is $2kT_e$.

Upon reaching the emitter, the electrons will gain additional kinetic energy as they traverse the work function potential barrier from the opposite side. The average total energy that each electron transfers into the emitter is then $e\left(2kT_e/e + \phi_t\right)$, and the total power the plasma electrons deliver to the emitter is given by

$$P_e = I_e\left(\frac{2kT_e}{e} + \phi_t\right) \tag{5.44}$$

5.4.4 Heat Balance at the Emitter Surface

Some amount of electrical power, P_{heat}, will be provided to the cathode's heating element during operation. In practice however, not all of that power is actually conducted into the emitter. This power is also conducted into other parts of the cathode's body, as well the cathode's support structure, and radiated off those components as they heat up. As a result, only a fraction, η_{heat}, of the power generated by the heater supply is actually goes towards heating the emitter. This fraction is dependent on the geometry of the cathode, the geometry of the support structure, the materials used in those sub-systems, and the the heat-shielding of the cathode-support system.

The power balance at the emitter surface can be written as

$$\eta_{heat}P_{heat} + P_i + P_e = P_{rad} + P_{emit} \tag{5.45}$$

Re-arranging this yields an equation for the heating power required to produce the current density j_{th}.

$$P_{heat} = \frac{1}{\eta_{heat}}\left(P_{rad} + P_{emit} - P_i - P_e\right) \tag{5.46}$$

In total, P_{heat} is a function of eleven different input variables.

$$P_{heat} = F(j_{th}, V_c, n_0, T_e, m_i, U_i^+, \phi_0, \alpha, \epsilon, A_c, \eta_{heat}) \tag{5.47}$$

The properties of the bulk plasma, the total sheath potential drop, the properties of the gas being used in the discharge, the material properties of the emitter, and the geometric properties of the cathode and it's support structure, must all be known in order to calculate the P_{heat} necessary to produce j_{th}.

5.5 P_{heat} as a Function of a Hall Thruster's Discharge Properties

In the previous sections, a method of calculating the heating power required to produce a given emitted current density was presented. This model assumed the planar cathode was operating inside a generic plasma discharge. The focus of this paper however, is a planar cathode operating inside a Hall thruster's discharge, and the goal, as stated back in section 4.1, is to obtain P_{heat} as a function of the thruster's discharge properties. This section outlines two additional equations that will be used to relate the sheath voltage and emitted current density, to the Hall thruster's discharge voltage and discharge current.

5.5.1 Discharge Current

As stated in section 3.2, the discharge current in a Hall thruster is defined as the current flowing through power supply connected between the anode and cathode. This will necessarily be the total current crossing the plane of the emitter's surface. A diagram of this is showcased in figure 5.3.

The total current crossing this plane is emitted current $I_{th} = j_{th}A_c$, plus the back-streaming ion current I_i, minus the back-streaming electron current I_e. The discharge current is then related to the emitted current density through the following equation

$$I_d = j_{th}A_c + I_i - I_e \tag{5.48}$$

Equation 5.48 must be added to the model in order to obtain P_{heat} as a function of the discharge current, instead of the emitted current density.

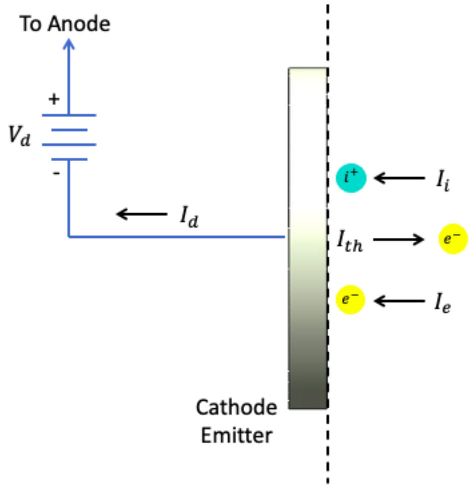

Figure 5.3: Diagram of the total current crossing the emitter's surface.

5.5.2 Coupling Voltage

In a Hall thruster a discharge voltage V_d will be applied between the thruster's anode and cathode during operation. As stated back in section 3.2, due to the cross-field configuration of a Hall thruster's discharge, part of the applied voltage drop will exist between the anode and the exhaust beam, and the remaining portion of the drop, the coupling voltage, will exist between the beam and the cathode.

For a planar cathode, part of the coupling voltage drop will occur across cathode sheath and pre-sheath regions. This is the potential that will draw the emitted electrons into the plasma. The remaining portion of the coupling voltage drop will occur in the plasma between the cathode sheath and the exhaust beam. This voltage, which will be labeled V_r, is necessary to draw the electrons into the channel discharge. In total, the coupling voltage for a planar cathode-equipped Hall thruster can be written as

$$V_{cc} = V_c + V_r \tag{5.49}$$

The cathode sheath voltage will then be some fraction of the total coupling voltage. For this analysis however, it will be assumed that the entire coupling voltage drop will occur across the cathode sheath. Therefore, the total sheath voltage can be related to the discharge voltage and the voltage utilization efficiency through the following equation:

$$V_c \approx V_{cc} = V_d\left(1 - \eta_v\right) \tag{5.50}$$

With equations 5.48 and 5.50 added to the model, P_{heat} is now obtained as a function of the thruster's discharge properties.

$$P_{heat} = F(I_d, V_d, \eta_v, n_0, T_e, m_i, U_i^+, \phi_0, \alpha, \epsilon, A_c, \eta_{heat}) \tag{5.51}$$

Once P_{heat} is known, $(\eta_c\eta_0)_{planar}$ can be calculated using equation 5.4 assuming the magnet power is also known.

5.6 Maximum Allowable Discharge Current

It should be noted that planar cathode will not always be able to produce a desired discharge current under any arbitrary set of conditions. Based on the density and temperature of the plasma local to the cathode, as well as the coupling voltage, there will be a maximum, space charge limited, value of the emitted current density, j_{max}. At this value of emitted current, the electric field at the cathode surface is zero. This maximum current density can be solved for by setting E_c in equation 5.31 to zero, and then solving 5.23, 5.29, 5.31, 5.21, 5.50 and 5.6 for j_{max} alongside the space charge limited values of n_{i0}, n_{e0}, V_0, and V_s. Once these are determined, the maximum allowable discharge current, $I_{d,max}$, can be solved for using equation the following equation:

$$I_{d,max} = j_{max}A_c + en_{i0}^{*}A_c\left(\frac{2eV_0^*}{m_i}\right)^{1/2} - en_0\left(\frac{kT_e}{2\pi m_e}\right)^{1/2} exp\left(\frac{-eV_c}{kT_e}\right)A_c \tag{5.52}$$

Here, the star superscript indicates that the space charge limited value of that quantity is being used. In total, the maximum discharge current will be a function of n_0, T_e, V_d, η_v, m_i, and A_c.

$$I_{d,max} = G(V_d, \eta_v, m_i, n_0, T_e, A_c) \tag{5.53}$$

As outlined the previous section, solving for P_{heat} requires a value for the discharge current (among other variables) to first be specified. If the additionally specified values of n_0, T_e, V_d, η_v, m_i and A_c determine that the maximum allowable discharge current is lower than the user-specified discharge current, the eight sheath equations won't have a real solution. Thus, before attempting to calculate P_{heat} for a given discharge current, the subsystem of equations mentioned in the previous paragraph must be first solved to determine $I_{d,max}$. If it's the case that I_d (provided) $\leq I_{d,max}$, then one can proceed to solve for P_{heat} and $(\eta_c\eta_0)_{planar}$.

The full solution procedure is summarized in figure 5.4.

5.7 Plasma Properties Local to the Cathode Surface

In total, $(\eta_c\eta_0)_{planar}$ is a function of thirteen different input variables.

$$(\eta_c\eta_0)_{planar} = H(I_d, V_d, \eta_v, n_0, T_e, m_i, U_i^+, \phi_0, \alpha, \epsilon, A_c, \eta_{heat}, P_{mag}) \tag{5.54}$$

Not all of these variables are completely independent from each other, however. Certain inputs like the cathode's material properties, the cathode area, the heating efficiency, and the type of propellant gas are mostly independent, and could, in practice,

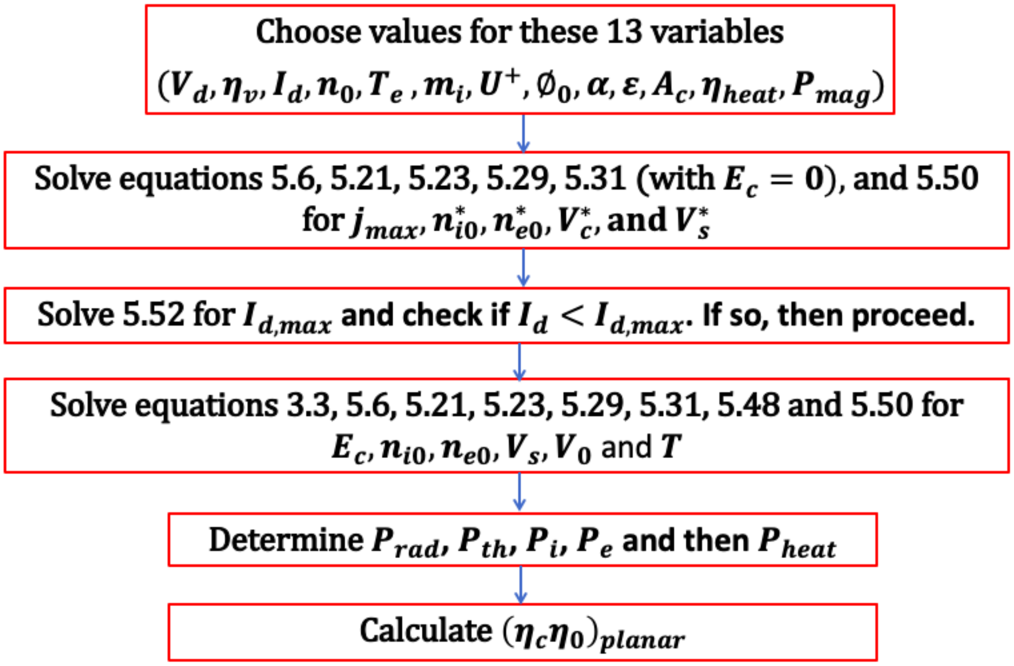

Figure 5.4: Full procedure for determining $(\eta_c\eta_0)_{planar}$.

be controlled by the Hall thruster's engineer. The discharge voltage can be set by the external discharge supply, but the resulting discharge current and voltage utilization efficiency are dictated by a complex combination of the discharge voltage, the channel wall material, the channel dimensions, the anode propellant flow rate, and the magnetic field strength and topology. Meanwhile, the plasma density and electron temperature local to the planar cathode's surface will be a function of both the discharge properties of the thruster, and the location at which the planar cathode is equipped.

Due to the complex relationship between the discharge voltage, discharge current, and voltage utilization efficiency, simple expressions relating these quantities do not, to the author's knowledge, exist. Thus, for the purpose of calculating $(\eta_c\eta_0)_{planar}$ using this model, V_d, I_d, and η_v will be treated as fully independent input variables, and this thesis will explore how $I_{d,max}$ and $(\eta_c\eta_0)_{planar}$ scale with these quantites. In an attempt to reduce the number of independent variables however, this section will present simple algebraic expressions that relate n_0 and T_e to the discharge properties of the thruster.

5.7.1 Cathode Mounting Schemes

As mentioned in section 3.1, there are two common ways to mount cathode's on Hall thruster's: internally and externally.

As an example of a Hall thruster with an externally mounted cathode, figure 5.5 shows images of the BHT-200 Hall thruster developed by Busek.

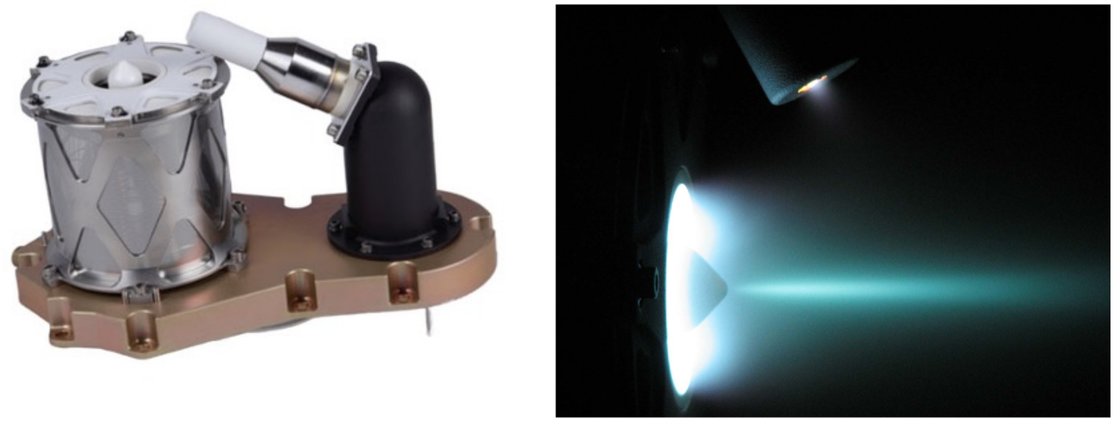

Figure 5.5: Images of the BHT-200 Hall thruster. The right photo showcases the BHT-200 in operation.

If the planar cathode is mounted externally, in the manner showcased in figure 5.5, its surface will be in contact with the thruster's plume plasma during operation. This is a non-ideal mounting scheme for a planar cathode due to the diffuse nature of the plume plasma.

Figure 5.6 shows a contour plot of the BHT-200's plume plasma density. This contour plot was generated from a PIC-simulation of the BHT-200's plume operating at it's nominal conditions [25]. It can be seen that the plasma density decreases by

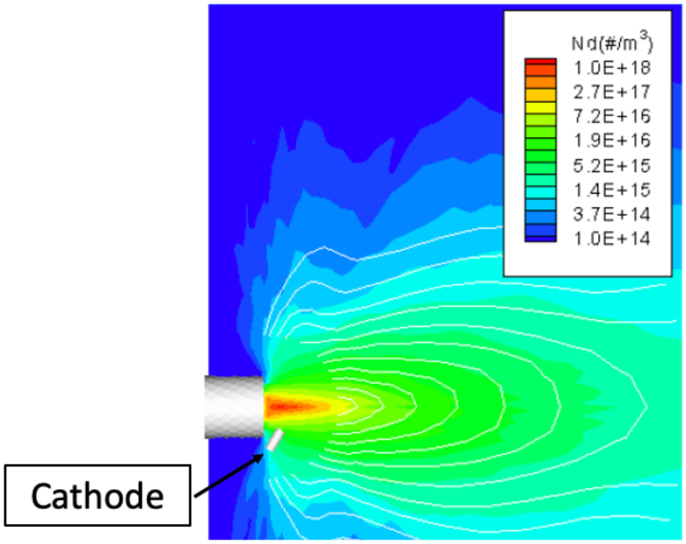

Figure 5.6: Contour plot of the BHT-200's plume plasma density [25].

more than an order of magnitude moving from the region near the channel exit, to the location of the cathode. From equation 5.17, we can see that the ion density inside the sheath roughly scales linearly with the bulk plasma density. These ions help neutralize the emitted electron space charge, which allows more current to be extracted from the cathode. Having a dense plasma local to the planar cathode is essential for maximizing the value of $I_{d,max}$. Hence, an externally mounted planar cathode will likely not be able to meet a given thruster's discharge current needs.

The other option is to mount the cathode internally along the thruster's axis, as is the case with Busek's BHT-1500 shown in in figure 5.7. In this configuration the planar cathode's surface would be flush with the channel exit plane, and the plasma properties local to it would be similar to what's found at the channel exit. This is a far more favorable location at which to mount the planar cathode due to the higher plasma density found near the exit.

For the purposes of the efficiency model, it will be assumed that the planar cathode is mounted internally, as is shown in figure 5.8. The density and temperature of

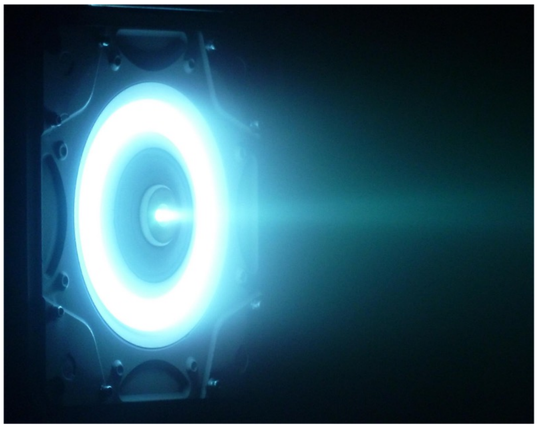

Figure 5.7: Image of the BHT-1500 Hall thruster in operation.

the plasma local to the cathode will be assumed to be equal to the density and temperature of the plasma at the channel exit. That is, the thruster's plasma properties are taken to be uniform across the thruster's exit plane. The following subsections outline simple scaling laws that can be used to determine the density ($n_{0,ex}$) and temperature ($T_{e,ex}$) of the plasma at the channel exit, as functions of the discharge voltage and utilization efficiencies of the thruster.

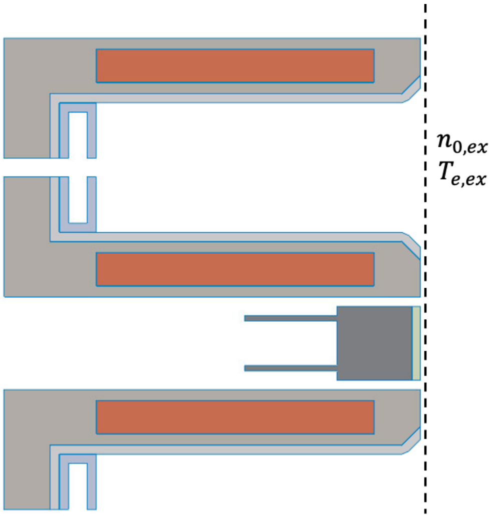

Figure 5.8: Schematic of a planar cathode mounted along a Hall thruster's axis.

5.7.2 Plasma Density at the Channel Exit

The ion beam current in a Hall thruster, assuming singly charged ions, can be expressed as

$$I_b = e n_{i,ex} v_{ex} A_{ch} \tag{5.55}$$

where v_{ex} is the average exit velocity, $n_{i,ex}$ is the ion density at the channel exit, and A_{ch} is the area of the channel exit plane.

As mentioned in section 3.2, the exit velocity of the ions is not a uniform quantity. Different ions will have different exit velocities depending on where in the acceleration zone they were created. It will be assumed here that every single ion is created at the start of the acceleration zone, and will fall through the full beam potential. The exit velocity of the ions is then given by

$$v_{ex} = \left(\frac{2e\eta_v V_d}{m_i}\right)^{1/2} \tag{5.56}$$

Rearranging equation 5.55 for the ion density yields

$$n_{i,ex} = \frac{\eta_b I_d}{e\left(\frac{2e\eta_v V_d}{m_i}\right)^{1/2} A_{ch}} \tag{5.57}$$

Since the plasma is quasi-neutral in the exit region, the above quantity is also equal the plasma density, $n_{0,ex}$, in that region. The quotient $J_{ch} = I_d/A_{ch}$ is the discharge current density in the thruster channel. Experiments have shown that the discharge current density is fairly constant quantity across most Hall thrusters, hovering in the range of $1000 - 1500 A/m^2$ [11]. Utilizing this scaling law the plasma density at the exit plane of a Hall thruster is then simply a function of V_d, η_v, η_b and m_i.

$$n_{0,ex} = \frac{10^3 \eta_b}{e\left(\frac{2e\eta_v V_d}{m_i}\right)^{1/2}} \tag{5.58}$$

Since both plasma heating power and the maximum allowable discharge current scale well with increasing plasma density, $1000 A/m^2$ was chosen for J_d in order to provide a more conservative estimate for the plasma density.

5.7.3 Electron Temperature at the Channel Exit

It has been demonstrated experimentally that, for lower voltages, the electron temperature in the downstream, magnetized, region of a Hall thruster's channel has fairly linear dependence on discharge voltage [9] [33] [32] [31]. At larger discharge voltages however, the electron temperature can begin to saturate. Raites et al. explored this effect in their medium power Hall thruster [32]. Figure 5.9 shows the maximum electron temperature measured within their thruster plotted as a function of the applied discharge voltage.

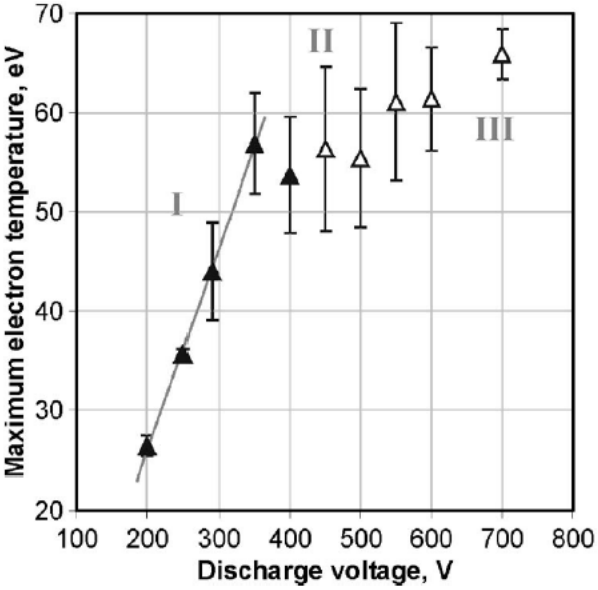

Figure 5.9: Maximum electron temperature measured as a function of discharge voltage. The open triangles indicate that the peak temperature was measured outside the channel [32].

Below 400V the electron temperature is observed to increase linearly from $\sim$ 25eV to $\sim$ 50eV as the discharge voltage is raised from 200V to 400V. Above the 400V threshold, this growth is stunted, and the electron temperature slowly rises from $\sim$ 50eV to $\sim$ 65eV as the discharge voltage is increased to 700V.

This saturation effect can be possibly attributed to the emission of secondary electrons from the channel walls [33]. Increasing the electron temperature in the channel increases the flux of plasma electrons to the channel walls, which in turn increases the flux of secondary electrons from the channel walls. The presence of secondary electrons within a sheath adjacent to a floating boundary reduces the potential drop across the sheath [13]. A reduction of the repulsive channel-wall sheath potential serves to further drive up the plasma electron flux and plasma electron power loss to the walls. As a result, the electron power transferred to the walls has an incredibly strong dependence on the electron temperature, both from it's natural scaling with temperature ($\sim T_e^{3/2} e^{-1/T_e}$ for Maxwellian electrons) and from the temperature-dependent reduction of the sheath potential. This extreme power loss at large temperatures can balance out the power provided to the electron fluid from joule heating, leading to a saturation of the electron temperature.

It should be noted that competing explanations for this temperature saturation have been proposed [32]. Fluid models of the channel plasma that assume Maxwellian electrons predict a significantly lower saturation temperature and voltage compared to the measured values shown. Additionally, measurements of the plasma potential inside the thruster suggestted that a decrease in the joule heating experienced by the electrons could also contribute to this saturation.

A common rule-of-thumb for Hall thrusters is that the electron temperature in the magnetized region is found to be roughly one-tenth of the beam voltage [11].

$$kT_e(eV) = 0.1V_b = 0.1\eta_v V_d \tag{5.59}$$

While this scaling law captures the initial linear trend demonstrated in the experimental measurements, it fails to account for any temperature saturation. In the data sets showcased in figure 5.9, the electron temperature was observed to saturate around 60eV. Thus, for the purposes of this analysis, the electron temperature will be treated as a piece-wise function. Equation 5.59 will be used to calculate kT_e as a function of discharge voltage up until the limit of 60eV. After this point, using the above data as a benchmark, the electron temperature will no longer increase with voltage and will remain at 60eV. In piecewise form, $kT_{e,ex}$ is given by

$$kT_{e,ex}(eV) = \left\{ \begin{array}{ll} 0.1\eta_v V_d, & \text{if } 0.1\eta_v V_d \leq 60 \\ 60, & \text{if } 0.1\eta_v V_d > 60 \end{array} \right\} \tag{5.60}$$

Using equations 5.58 and 5.60, the electron temperature and density local to the cathode's surface can be determined solely from the discharge voltage, the beam and current utilization efficiencies, and the atomic mass of the propellant. Adding these equations, n_0 and T_e are removed as independent variables from the model, at the cost of adding in the current utilization efficiency (η_b). $I_{d,max}$ and $(\eta_c\eta_0)_{planar}$ are now functions of the following variables:

$$I_{d,max} = G_2(V_d, \eta_v, \eta_b, m_i, A_c) \tag{5.61}$$

$$(\eta_c\eta_0)_{planar} = H_2(I_d, V_d, \eta_v, \eta_b, m_i, U_i^+, \phi_0, \alpha, \epsilon, A_c, \eta_{heat}, P_{mag}) \tag{5.62}$$

Chapter 6

RESULTS OF EFFICIENCY MODEL

6.1 Calculations of the Maximum Discharge Current

In this section, the dependencies of $I_{d,max}$ on the discharge voltage and the utilization efficiencies will be explored. For the plots showcased in sections 6.1.1 - 6.1.2, the cathode radius is fixed at 0.375", and the thruster is assumed to be operating on xenon.

6.1.1 $I_{d,max}$ as a Function of the Discharge Voltage

Figure 6.1a showcases the maximum discharge current plotted as a function of discharge voltage for three different values of η_b. Here, it's assumed the thruster has a voltage utilization efficiency of 85%.

At lower voltages, the maximum allowable discharge current is observed to remain fairly constant as the discharge voltage is increased. Once V_d reaches the value at which the electron temperature saturates, $I_{d,max}$ is then seen to increase monotonically as the discharge voltage is increased further. The voltage at which the temperature saturation occurs, V_{sat}, is given by

$$V_{sat}(V) = \frac{60(eV)}{0.1\eta_v} \tag{6.1}$$

To understand the behavior of $I_{d,max}$, it's necessary to look at how the individual currents that make up $I_{d,max}$ scale with discharge voltage. Figure 6.1b showcases the maximum value of the emitted current (I_{max}), alongside the space charge limited values of the back-streaming electron (I_e^*) and ion (I_i^*) currents, plotted as functions

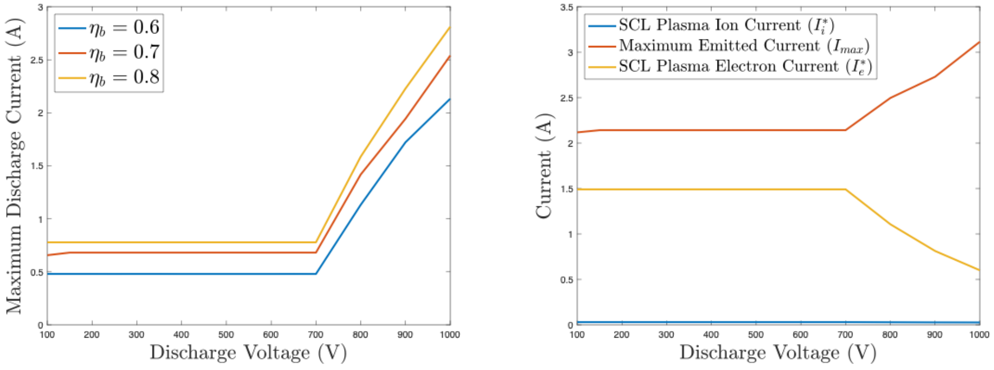

(a)

(b)

Figure 6.1: (a) $I_{d,max}$ plotted as a function of the discharge voltage. (b) I_{max}, I_e^*, and I_i^* plotted as a functions of the discharge voltage for the $\eta_b = 0.7$ case. For both plots, it's assumed that $\eta_v = 0.85$.

of the discharge voltage, for the case corresponding to $\eta_b = 0.7$.

I_{max} is also observed to remain constant at lower voltages. The reason it behaves in this way is because there are several competing effects occurring simultaneously. Increasing the discharge voltage increases the voltage drop across the cathode sheath. On its own this would increase the strength of the electric field at the cathode surface, allowing more current to be extracted from the cathode. However, as dictated by equations 5.58 and 5.60, the local plasma density and temperature decease and increase respectively, as V_d is raised. Decreasing the local plasma density decreases the density of plasma ions within the sheath. Plasma ions help neutralize the emitted electron space charge near the cathode, so a reduction in the plasma density also acts to reduce I_{max}. Conversely, increasing the local electron temperature increases the number of plasma electrons which are able to penetrate into the sheath. Plasma electrons contribute to the negative space charge at the cathode surface, which means less electrons can be emitted before the space charge limit is reached. In total, the benefits of increasing discharge voltage are offset by the changes in the bulk plasma properties, and I_{max} remains constant.

Once the saturation voltage is reached, I_{max} is observed to increase with voltage. In this regime, the discharge voltage can be increased without incurring the penalties of increasing the electron temperature, allowing the maximum current to rise.

The back-streaming electron current also remains constant a low voltages. However, it begins to decline once the saturation voltage is reached. Plugging equations 5.58 and 5.60 for the plasma density and temperature into equation 5.43, yields the following expressions for the back-streaming electron current to the cathode:

$$I_e^* = \left\{ \begin{array}{ll} A_c 10^3 \eta_b \left(\frac{0.1 m_i}{4\pi m_e}\right)^{1/2} exp\Big(-\frac{1-\eta_v}{\eta_v}\Big), & \text{if } 0.1\eta_v V_d \leq 60 \\ A_c 10^3 \eta_b \left(\frac{60 m_i}{4\pi m_e \eta_v V_d}\right)^{1/2} exp\Big(-\frac{V_d(1-\eta_v)}{60}\Big), & \text{if } 0.1\eta_v V_d > 60 \end{array} \right\} \tag{6.2}$$

According to equation 6.2, for fixed values of η_v, η_b, A_c, and m_i, the back-streaming electron current is independent of the discharge voltage below the saturation point. Above it, the electron current scales as $\propto V_d^{-1/2} e^{-V_d}$. This is consistent with the behavior of I_e^* showcased in figure 6.1b.

Circling back to figure 6.1a, the maximum discharge current is approximately the difference between I_{max} and I_e^*. Both currents remain constant below the saturation voltage, and so $I_{d,max}$ remains constant as well. Above the saturation voltage, I_{max} increases while I_e^* decreases. As a result $I_{d,max}$ increases, and at a faster rate than I_{max}, explaining the behavior shown in figure 6.1a. The back-streaming ion current contributes to the discharge current as well. However, due to the large atomic mass of xenon, this current is two orders of magnitude smaller than the electron currents at every voltage level and can thus be neglected.

The final thing to note is that the maximum discharge current is shown to increase with increasing η_b. This is to be expected as equation 5.58 dictates that the local plasma density scales linearly with the current utilization efficiency.

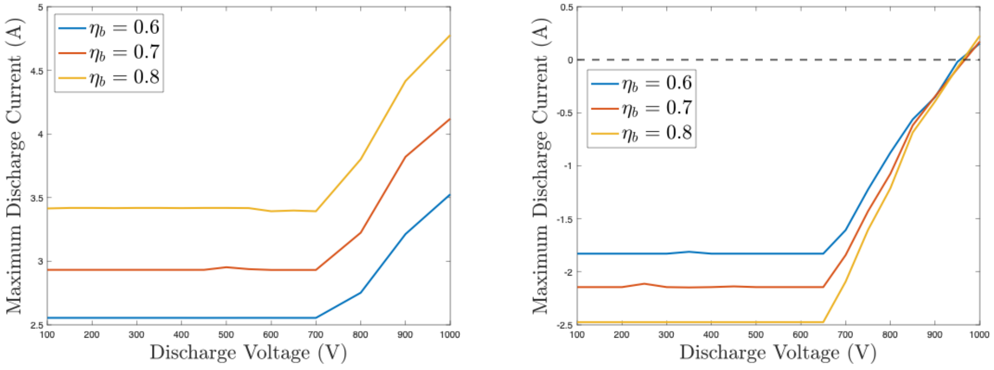

(a) (b)

Figure 6.2: $I_{d,max}$ plotted as a function of the discharge voltage for η_v values of 0.8 (a) and 0.9 (b).

6.1.2 $I_{d,max}$ as a Function of the Voltage Utilization Efficiency

Figure 6.2a showcases $I_{d,max}$ plotted as a function of the discharge voltage, but now for a voltage utilization efficiency of 80%. Compared to the $\eta_v = 0.85$ case, the maximum discharge current is now higher by over 2A at every discharge voltage level. This is due to the increased sheath voltage available to help extract electrons.

In contrast figure 6.2b showcases the same plot of $I_{d,max}$ for a voltage utilization efficiency of 90%. With only 10% of the discharge voltage across the sheath, the back-streaming electron current is always larger than the maximum emitted current except at discharge voltages exceeding 950V. This results in a negative value of $I_{d,max}$ over the range of discharge voltages at which Hall thruster's typically operate at.

The results discussed in the previous paragraph showcase a situation in which the model presented in chapter 5 breaks down. In this model, the plasma is assumed to form with the properties η_b, η_v, $n_{0,ex}$, and T_{ex}, and the maximum discharge current is then calculated from those properties. A negative discharge current is un-physical, and a Hall thruster's plasma will not form with properties that would allow for that. Therefore, if it's the case that the selected values of V_d, η_b and η_v lead to a negative value of the maximum discharge current, it will be assumed that no plasma would form at all. Thus, for a Hall thruster to even ignite with a planar cathode, the voltage utilization efficiency needs to be comfortably less than 0.9.

6.2 Calculations of $(\eta_c\eta_0)_{planar}$

In this section, the dependencies of $(\eta_c\eta_0)_{planar}$ on the discharge voltage, discharge current, cathode radius, and emitting material will be explored. For the plots showcased in sections 6.2.1 - 6.2.3, figure 6.3 outlines the values chosen for the input variables that are being held fixed. In these sections, the emitter is assumed to be made from LaB_6, and the thruster is assumed to be operating on xenon. In section 6.2.4, the choice of emitting material will be varied.

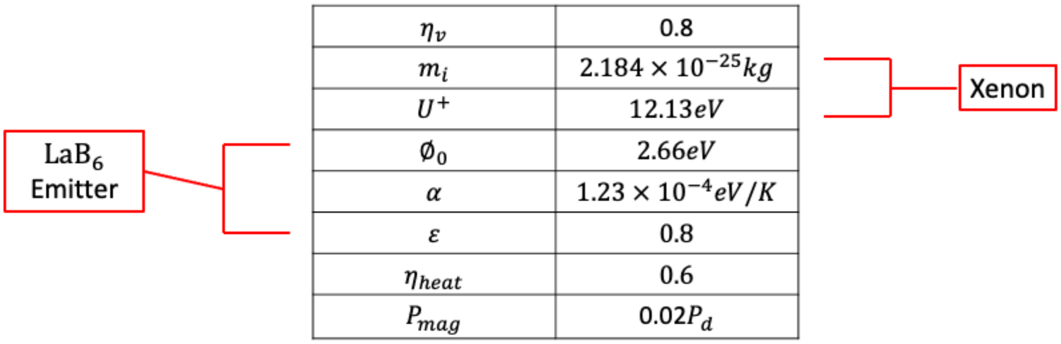

η_v	0.8
m_i	$2.184 \times 10^{-25} kg$
U^+	$12.13 eV$
$\emptyset_0$	$2.66 eV$
α	$1.23 \times 10^{-4} eV/K$
ε	0.8
η_{heat}	0.6
P_{mag}	$0.02 P_d$

Figure 6.3: Table showcasing the fixed values of several input variables.

6.2.1 $(\eta_c\eta_0)_{planar}$ *as a Function of the Discharge Voltage*

Figure 6.4 shows $(\eta_c\eta_0)_{planar}$ plotted as a function of the discharge voltage for three different values of the current utilization efficiency. For this plot, the discharge current was fixed at 2A, and the cathode radius was fixed at 0.375". On the same plot is a dashed line representing a typical value of $(\eta_c\eta_0)_{hollow}$. This value of $(\eta_c\eta_0)_{hollow}$ was calculated assuming that $\eta_{c,hollow} = 0.935$. In every curve shown in figure 6.4

$(\eta_c\eta_0)_{planar}$ initially increases before peaking at the saturation voltage. From there, it begins to decrease as the discharge voltage is increased further.

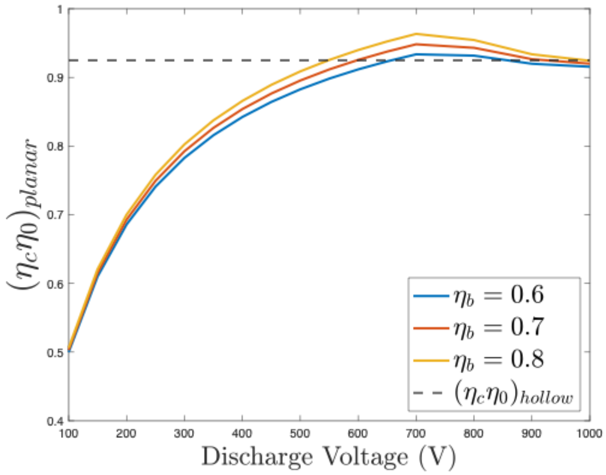

Figure 6.4: $(\eta_c\eta_0)_{planar}$ plotted as a function of the discharge voltage. Here it's assumed that $I_d = 2A$, and $r_c = 0.375in$.

To explore this behavior further, figure 6.5 showcases the plasma ion power, plasma electron power, emitted power loss, and radiated power loss plotted as functions of the discharge voltage, for case corresponding to $\eta_b = 0.7$.

From figure 6.5, it's clear that the dominant power loss term is the radiated power loss. P_{rad} is observed to remain constant as a function of discharge voltage up until the saturation voltage. After this point it begins to decrease. The radiated power loss term is determined by the surface temperature of the cathode, which in turn is dictated by how much current needs to be emitted to to meet the discharge current requirement. To keep the discharge current fixed at 2A, the emitted current must either rise or fall in response to changes in the back-streaming electron current. As shown in equation 6.2, the back-streaming electron current is constant as a function of discharge voltage, prior to the saturation voltage. Since I_e is not changing in this regime, the emitted current does not change either. Above the saturation voltage the

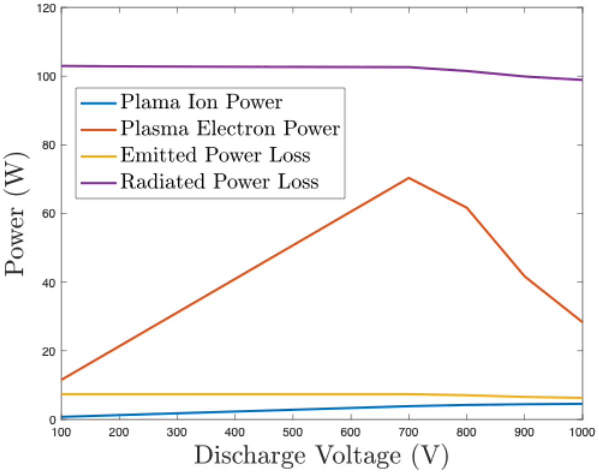

Figure 6.5: P_i, P_e, P_{emit}, and P_{rad} plotted as a functions of the discharge voltage. Here it's assumed that $\eta_b = 0.7$, $I_d = 2A$, and $r_c = 0.375in$.

back-streaming electron current drops, and so the required emitted current drops as well. Figure 6.6a showcases the required emitted current plotted a function of the discharge voltage for every trial, where this trend is demonstrated. The required cathode surface temperature, shown in figure 6.6b, expectedly follows the same pattern, explaining the behavior of the radiated power loss.

The non-dominant power loss term is the emitted power loss. Since the emitted power loss is directly proportional to the emitted current, it should also remain constant with voltage and decrease after the saturation point, which is exactly what's observed to happen in figure 6.5.

The dominant heating term is the plasma electron power. In figure 6.5 it's seen to rise linearly with discharge voltage, before exponentially declining after the saturation voltage. Combining equations 5.58 and 5.60 with equation 5.44 yields the following piece-wise function for the plasma electron heating power:

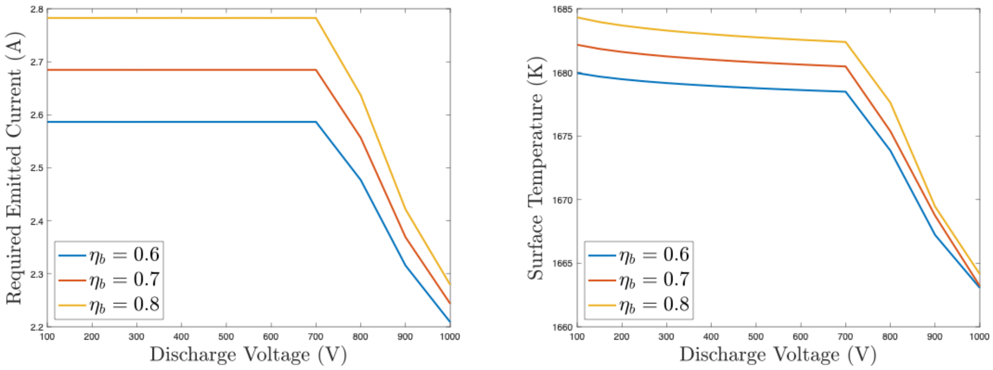

(a) (b)

Figure 6.6: I_{emit} (a) and T (b) plotted as a functions of the discharge voltage. Here it's assumed that $I_d = 2A$, $\eta_b = 0.7$, and $r_c = 0.375in$.

$$P_e = \left\{ \begin{array}{ll} A_c 10^3 \eta_b \left(\frac{0.1 m_i}{4\pi m_e}\right)^{1/2} exp\left(-\frac{1-\eta_v}{\eta_v}\right)(0.2\eta_v V_d + \phi_t)\,, & \text{if } 0.1\eta_v V_d \leq 60 \\ A_c 10^3 \eta_b \left(\frac{60 m_i}{4\pi m_e \eta_v V_d}\right)^{1/2} exp\left(-\frac{V_d(1-\eta_v)}{60}\right)(120 + \phi_t)\,, & \text{if } 0.1\eta_v V_d > 60 \end{array} \right\} \quad (6.3)$$

Below the the saturation voltage the electron heating power scales as $\propto V_d$ for fixed values of the cathode area and utilization efficiencies. Once the electron temperature saturates, the electron heating power scales as $\propto V_d^{-1/2} e^{-V_d}$. In the second regime the sheath voltage is increasing without a corresponding increase in the electron temperature, resulting in a decrease in the back-streaming electron current and electron power.

The final power term to consider is the ion heating power. This term is shown to slowly and monotonically increase as the discharge voltage is raised. This is to be expected as the sheath voltage is growing and ions are being accelerated to higher velocities before impacting the emitter. Due to the small magnitude of the back-streaming ion current, this term remains fairly negligible in comparison to the electron

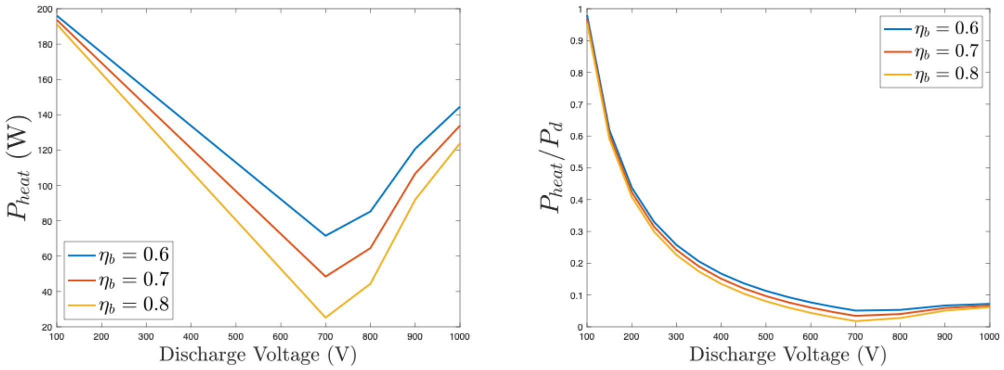

(a) (b)

Figure 6.7: P_{heat} (a) and P_{heat}/P_d (b) plotted as a functions of the discharge voltage. Here it's assumed that $I_d = 2A$, and $r_c = 0.375in$.

heating power.

Figure 6.7a now showcases required heating power plotted as a function of the applied discharge voltage. Next to it in figure 6.7b is the the ratio P_{heat}/P_d plotted as a function of the discharge voltage. P_{heat} observed to decrease fairly linearly up until the electron temperature saturation point, at which point it begins to rise. This behavior can be explained as follows. In the pre-saturation regime the power loss terms are constant while the electron heating power increases. This of course leads to a decrease in the required external heating power. Post saturation the power loss terms decrease, but at a slower rate than which the plasma electron power decreases, and so the required heating power slowly rises. The ratio of P_{heat}/P_d follows the exact same trend but with a much sharper decline and slower rise since the discharge power is increasing at every voltage level. Since $(\eta_c \eta_0)_{planar}$ is inversely proportional to P_{heat}/P_d for a given value of P_{mag}, it naturally follows the exact opposite trend, as was seen back in figure 6.4.

One last thing to note is that efficiency improves at every voltage level with increasing current utilization efficiency. This is a result of the plasma density, and by extension the electron and ions powers, having a linear dependence on η_b.

6.2.2 $(\eta_c\eta_0)_{planar}$ as a Function of the Discharge Current

Figure 6.8 shows $(\eta_c\eta_0)_{planar}$ plotted as a function of the discharge current for three different values of the current utilization efficiency. For this plot, the discharge voltage was fixed at 500V, and the cathode radius was fixed at 0.375". In every scenario, $(\eta_c\eta_0)_{planar}$ increases monotonically with increasing discharge current, up until the maximum discharge current limit is reached.

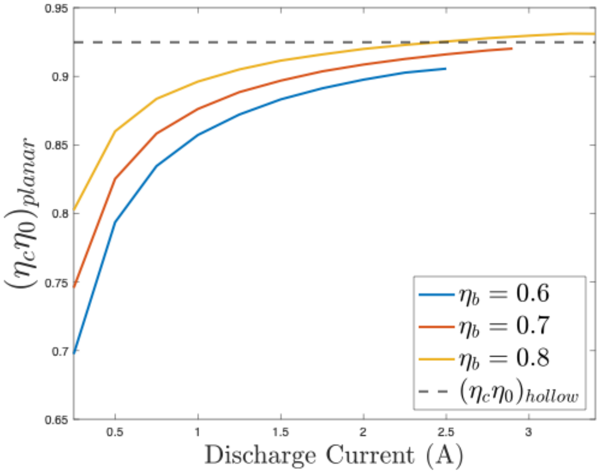

Figure 6.8: $(\eta_c\eta_0)_{planar}$ plotted as a function of the discharge current. Here it's assumed that $V_d = 500V$, and $r_c = 0.375in$.

To again explore this further, figure 6.9 showcases the various power terms plotted as functions of the discharge voltage for case corresponding to $\eta_b = 0.7$.

Both the radiated and emitted power losses are seen to increase with discharge current. This is to be expected as the required emitted current is increasing. Conversely, the plasma ion and electron heating terms are seen remain relatively constant. This is also to be expected as the bulk plasma properties and sheath voltage are being left unchanged. P_i and P_e will vary only slightly as a result of changes in the total

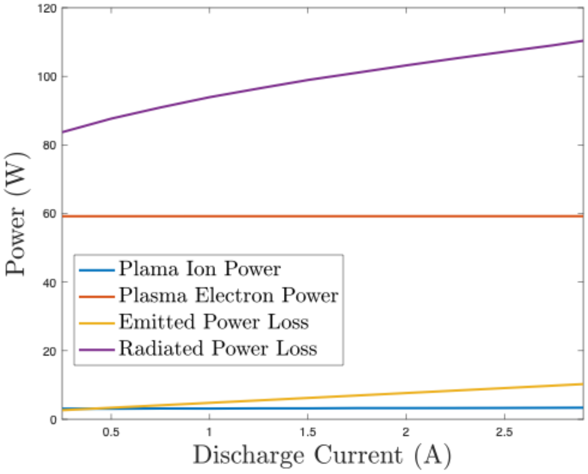

Figure 6.9: P_i, P_e, P_{emit}, and P_{rad} plotted as a functions of the discharge current. Here it's assumed that $\eta_b = 0.7$, $V_d = 500V$, and $r_c = 0.375in$.

work function of the emitter. These small changes in ϕ_t occur because the required surface temperature of the emitter, and the surface electric field, increase and decrease respectively, as the emitted current is increased.

Since the power losses are rising as the discharge current is increased, without significant compensation from the plasma heating terms, the required heating power also increases with the discharge current. This is demonstrated in figure 6.10a where the required heating power is plotted as a function the discharge current for all three trials.

While it is the case that the required heating power is growing at every current level, it's growing slower than the linearly increasing discharge power. As a result, the ratio P_{heat}/P_d decreases monotonically as a function of the discharge current, as shown in figure 6.10b. This leads to the behavior of $(\eta_c\eta_0)_{planar}$ showcased in figure 6.8.

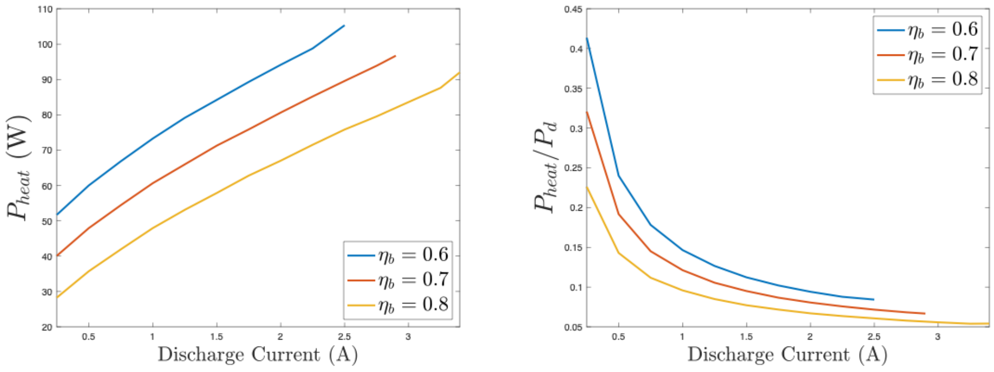

(a) (b)

Figure 6.10: (a) P_{heat}, and (b) P_{heat}/P_d plotted as a functions of the discharge current. Here it's assumed that $V_d = 500V$, and $r_c = 0.375in$.

6.2.3 $(\eta_c\eta_0)_{planar}$ as a Function of the Cathode Radius

Figure 6.11 showcases $(\eta_c\eta_0)_{planar}$ plotted as a function of the emitter radius for three different values of the current utilization efficiency. For these calculations, the discharge voltage was fixed at 600V, and the discharge current was fixed at 2.5A.

For the cases corresponding to $\eta_b = 0.6$ and $\eta_b = 0.7$, $(\eta_c\eta_0)_{planar}$ decreases monotonically with increasing cathode radius. For the $\eta_b = 0.8$ case, $(\eta_c\eta_0)_{planar}$ initially decreases before reaching some minimum value, at which point it begins to rise as the cathode radius is increased further.

To help understand the behavior of $(\eta_c\eta_0)_{planar}$, figure 6.12a showcases the various power terms plotted as functions of the cathode radius for the $\eta_b = 0.7$ case. As a followup, figure 6.12b showcases the various power densities plotted as functions of the cathode radius for the same case.

The radiated power density is observed to decrease with increasing cathode radius. This can be explained by the following logic. Ignoring the small back-streaming ion current, the discharge current can be expressed as

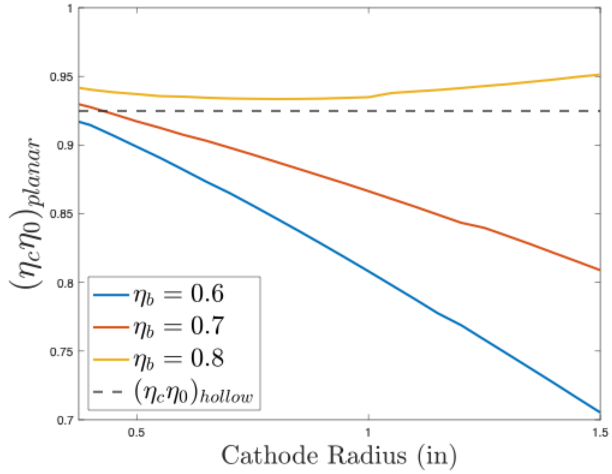

Figure 6.11: $(\eta_c \eta_0)_{planar}$ plotted as a function of the cathode radius. Here it's assumed that $V_d = 600V$, and $I_d = 2.5A$.

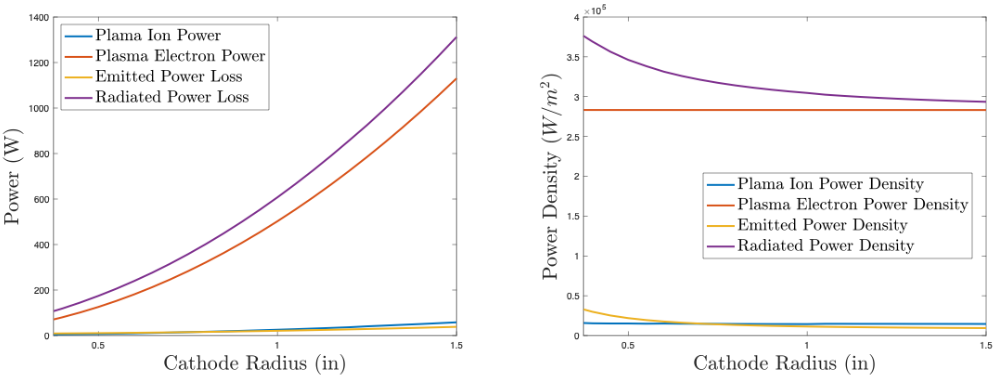

(a)

(b)

Figure 6.12: The various power terms (a), and their power densities (b) plotted as a functions of the cathode radius. Here it's assumed that $\eta_b = 0.7$, $V_d = 600V$, and $I_d = 2.5A$.

$$I_d = j_{th} A_c - j_e A_c \tag{6.4}$$

where $A_c = \pi r_c^2$. Re-arranging for the required emitted current yields

$$j_{th} = \frac{I_d}{\pi r_c^2} + j_e \tag{6.5}$$

For given values of η_b, η_v, and V_d, the back-streaming electron current density j_e is a constant as dictated by equation 6.2. Thus, for a fixed value of the discharge current, the required emitted current density, j_{th}, scales as $\propto 1/r_c^2$. Since the required emitted current density is shrinking, the required cathode surface temperature and the radiated power density also shrink as the cathode radius is increased.

While the radiated power density is decreasing with cathode radius, it's decreasing at a slower than quadratic rate. Thus, when multiplied with the quadratically increasing cathode area, the the total radiated power still increases with cathode radius, as seen in 6.12a.

The emitted power density is directly proportional required emitted current density, so it must decrease with cathode radius as well. This is consist with what is observed in figure 6.12b. However according to equation 6.4, the required emitted current increases with cathode radius due to the quadratically increasing back-streaming electron current. Hence, the total emitted power will still increase with cathode radius, as seen in figure 6.12a.

The plasma electron and ion power densities are predominantly determined by the bulk plasma properties and sheath voltage. Since these variables are not changing in each trial, those power densities relatively constant with increasing cathode radius, as observed in figure 6.12b. On the other hand, the plasma electron and ion heating powers have a linear dependence on cathode area, and thus increase quadratically with cathode radius, as seen in figure 6.12a.

As discussed above, every single power term increases with cathode radius. There-

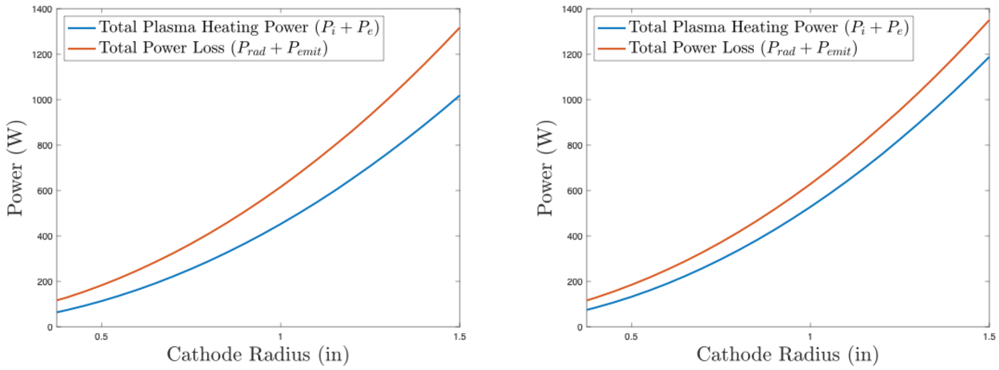

(a) $\eta_b = 0.6$ (b) $\eta_b = 0.7$

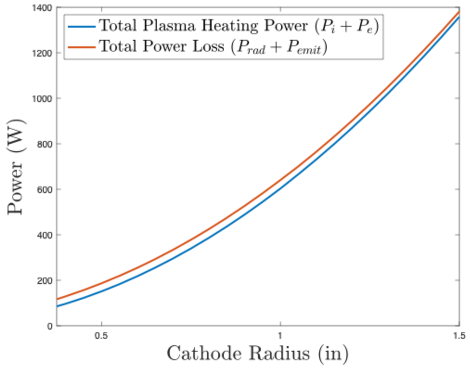

(c) $\eta_b = 0.8$

Figure 6.13: The total plasma heating power and total power losses plotted as functions of the cathode radius. Here it's assumed that $V_d = 600V$, and $I_d = 2.5A$.

fore, it's necessary to look at the rate at which these terms increase to understand why $(\eta_c \eta_0)_{planar}$ exhibits the behavior shown in figure 6.11.

Figures 6.13a-6.13c showcase the total plasma heating power $(P_i + P_e)$ and the total power loss $(P_{rad} + P_e)$ plotted as functions of the cathode radius. In the low η_b cases, the total power loss grows faster than the total plasma heating power as the cathode radius is increased. In these scenarios, the required heating power must increase with radius. In the highest η_b case, the opposite is observed to be true. The reason for this is that electron and ion heating power densities both scale linearly

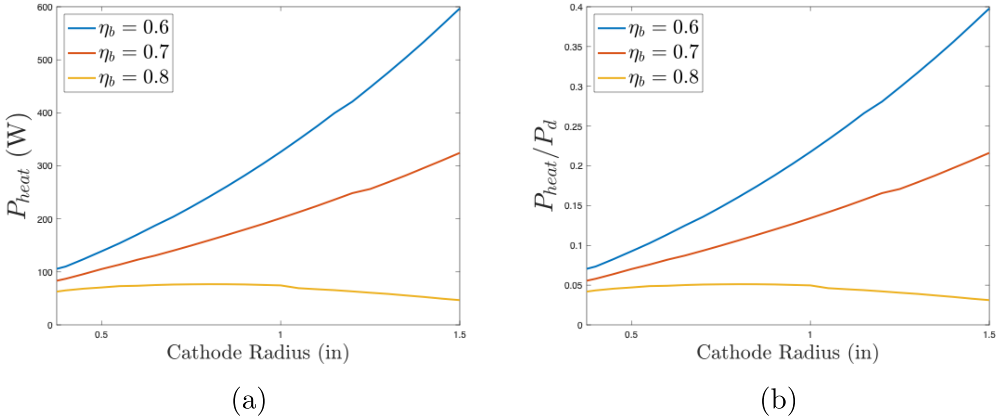

(a) (b)

Figure 6.14: (a) P_{heat}, and (b) P_{heat}/P_d plotted as a functions of the cathode radius. Here it's assumed that $V_d = 600V$, and $I_d = 2.5A$.

with the bulk plasma density, and by extension, the current utilization efficiency. In the $\eta_b = 0.8$ case, the plasma heating power densities are large enough such that total plasma heating power increases faster than the total power loss. In this scenario, the required heating power will decrease with cathode radius.

Figure 6.14a showcases the required heating power plotted as a function of of the cathode radius for all three η_b values, where the trends described in the previous paragraph are observed. Lastly, it can be seen from figure 6.14b that P_{heat}/P_d follows the same behavior as P_{heat} since the discharge power is being held fixed. Inverting the trends showcased in figure 6.14b yields the behavior of $(\eta_c\eta_0)_{planar}$ shown in figure 6.11.

6.2.4 $(\eta_c\eta_0)_{planar}$ as a Function of the Emitting Material

Figure 6.15 showcases $(\eta_c\eta_0)_{planar}$ plotted as a function of the discharge current, but for three different emitting materials. Here, the discharge voltage is fixed at $500V$, the cathode radius is fixed at $0.375in$, and the current utilization efficiency is fixed at 0.7.

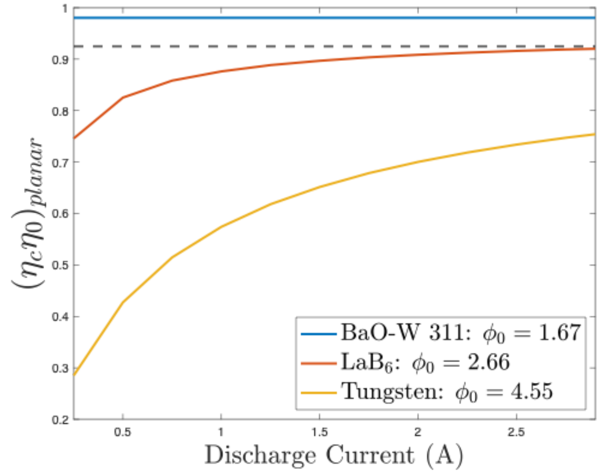

Figure 6.15: $(\eta_c\eta_0)_{planar}$ plotted as a function of the discharge current for three different materials. Here it's assumed that $\eta_b = 0.7$, $V_d = 500V$, and $r_c = 0.375in$.

From figure 6.15, it can be seen that $(\eta_c\eta_0)_{planar}$ improves with lower work function materials. The reason for this is that, for a given emitted current requirement, lower work function materials can operate at lower surface temperatures while providing said current. This means cathodes with better emitters will have lower radiative power losses and can be operated with less external heating power. Figures 6.16a and 6.16b showcase both the required surface temperature, and the required external heating power as functions of the discharge current, for the same case shown in figure 6.15. Here, the previously described behavior can be clearly observed.

When using the type 311 oxide cathode, the radiative power losses are low enough such that the required heating power is zero, as seen in figure 6.16b. In this case, the plasma heating is enough to maintain the required operating temperature. In figure 6.15, the $(\eta_c\eta_0)_{planar}$ vs I_d curve associated with the oxide cathode is a horizontal line sitting at the value 0.98. This is the maximum possible value $(\eta_c\eta_0)_{planar}$, achievable when only the magnet and discharge powers are left.

Figures 6.17a and 6.17b showcase $(\eta_c\eta_0)_{planar}$ plotted as functions of the discharge

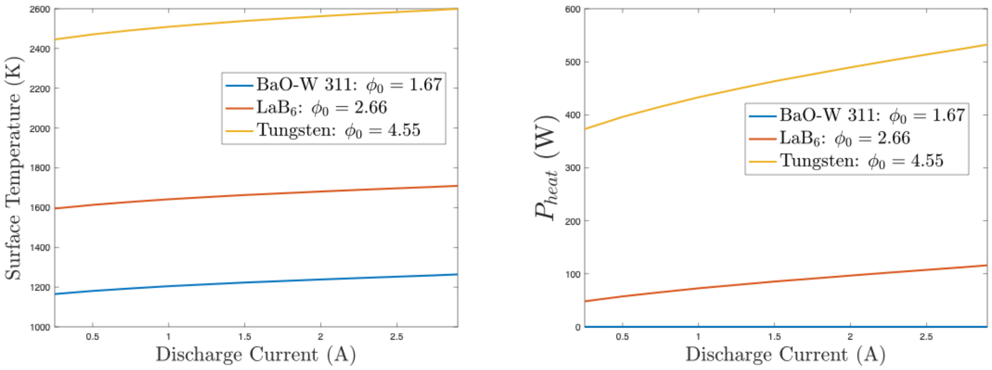

(a) (b)

Figure 6.16: The required surface temperature (a), and the radiated power loss (b) plotted as a functions of the discharge current for three different materials. Here it's assumed that $\eta_b = 0.7$, $V_d = 500V$, and $r_c = 0.375in$.

voltage and cathode radius respectively, for the same three materials. It's again observed that $(\eta_c\eta_0)_{planar}$ is larger at every operating point for the lower work function materials. Additionally, $(\eta_c\eta_0)_{planar}$ is again observed reach its maximum value over most operating points when using an oxide cathode.

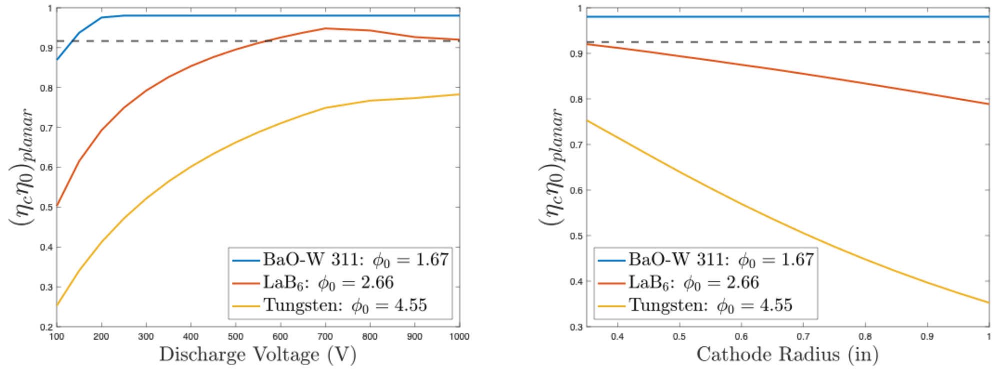

(a) (b)

Figure 6.17: $(\eta_c\eta_0)_{planar}$ plotted as a function of the discharge voltage (a), and the cathode radius (b). In a) it's assumed that $\eta_b = 0.7$, $I_d = 2.A$, and $r_c = 0.375in$. In b) it's assumed that $\eta_b = 0.7$, $I_d = 2.5A$, and $V_d = 500V$.

Chapter 7

DISCUSSION

7.1 Summary of Results

7.1.1 Maximizing $I_{d,max}$

In section 6.1.1, it was found that $I_{d,max}$ is nearly constant as a function of discharge voltage when $V_d < V_{sat}$, and grows steadily for voltages above V_{sat}, where V_{sat} is given by equation 6.1. Thus, for discharge voltages below V_{sat}, the maximum discharge current is dictated purely by η_v, η_b, and A_c. $I_{d,max}$ was also show to scale positively with increasing η_b due to the increased plasma density at the exit plane.

In section 6.1.2, it was shown that having a sufficiently low voltage utilization efficiency is essential for maximizing $I_{d,max}$. For η_v values of 0.9 and above, it's nearly impossible to obtain a positive discharge discharge current. For an η_v value of 0.85, only $I_{d,max}$ values on the order of $10^{-1}A$ were attainable using a 0.75" diameter cathode for voltages below V_{sat}. Only once η_v was lowered to 0.8 were currents above 1A achievable in the low voltage range.

$I_{d,max}$ can also be increased by increasing the cathode's emitting area, but this comes with several issues. Since the planar cathode is center-mounted, its diameter needs to be comfortably smaller than the inner diameter of the thruster channel. Additionally, the discharge power level of a thruster scales with the cross-sectional channel area [3]. Thus, larger area cathodes will be incompatible with lower power thrusters. Lastly, as was seen in section 6.2.3, $(\eta_c \eta_0)_{planar}$ can scale poorly with the cathode area due to increased radiative power losses.

The scaling of $I_{d,max}$ with η_v presents several issues for the viability of planar cathodes. First, the voltage utilization efficiency is not a fully controllable parameter.

It's dictated by a complex array of factors, and can vary between operating points. Even if this parameter was fully adjustable, it would not be ideal to fix it at a lower value, just to allow a planar cathode to function. Lowing the voltage utilization efficiency reduces the beam voltage, the specific impulse, and the thrust at a given discharge voltage. Additionally, the total thruster efficiency scales linearly with η_v, as seen in equation 4.8. Thus, lowering η_v to allow a planar cathode meet the discharge current requirements could still result in a lower total efficiency, even if $(\eta_c \eta_0)_{planar} > (\eta_c \eta_0)_{hollow}$ for that particular operating point.

Working within the restrictions outlined above, planar cathodes could be a workable option on low current Hall thrusters that operate with low voltage utilization efficiencies.

7.1.2 Maximizing $(\eta_c \eta_0)_{planar}$

$(\eta_c \eta_0)_{planar}$ was found to increase with discharge voltage up until the saturation voltage is reached. At that point it begins to steadily decline. Thus, $(\eta_c \eta_0)_{planar}$ is maximized at $V_d = V_{sat}$. As for the discharge current, $(\eta_c \eta_0)_{planar}$ was shown to increase monotonically with I_d, up until the maximum discharge current limit was reached. Thus, for any given values of η_v, η_b, and A_c, $(\eta_c \eta_0)_{planar}$ would be maximised at the operating point $(V_{sat}, I_{d,max})$.

$(\eta_c \eta_0)_{planar}$ always increases with increasing η_b due to the increased plasma density local to the cathode. While $(\eta_c \eta_0)_{planar}$ was not varied as a function of η_{heat} in the previous chapter, it will always scale positively with this quantity as a larger η_{heat} means less wasted heat. Thus, the planar cathode should be properly shielded, and the support structure should be designed in such a way as to maximize the heat transferred to the emitter.

While under certain conditions $(\eta_c \eta_0)_{planar}$ was shown to scale positively with the cathode radius, maximizing r_c to take advantage of this would not be ideal. As mentioned in the previous section, there are several issues with larger area cathodes.

Thus, for a given discharge current requirement I_d, the ideal cathode radius is the smallest possible value ($r_{c,min}$) that can provide that current, based on specified values of η_v, η_b, and V_d.

Lastly, for any given values of V_d, I_d, η_v, η_b, and A_c, $(\eta_c\eta_0)_{planar}$ was shown to always be larger for lower work function materials.

When using a LaB_6 emitter, $(\eta_c\eta_0)_{planar}$ was seen to approach and, depending on the chosen value of η_b, even exceed the plotted sample value of $(\eta_c\eta_0)_{hollow}$ as V_d, I_d, and r_c approached the values V_{sat}, $I_{d,max}$, and $r_{c,min}$ respectively. When using an oxide emitter, $(\eta_c\eta_0)_{planar}$ comfortably exceeded $(\eta_c\eta_0)_{hollow}$ over most of the showcased operating points. These results bode well for the viability of planar cathodes, particularly if they employ oxide emitter, provided that the discharge current requirement can be met.

7.2 Experimental Hall Thruster Data

Figure 7.1 showcases a table containing the measured values of V_d, I_d, η_b and η_v for selected operating points of several existing Hall thrusters. The inner channel diameter (D_1) of each thruster is also listed. For each operating point, the smallest possible planar cathode diameter ($D_{c,min}$) that can provide the specified discharge current is calculated. Provided that a positive discharge current can be achieved with a planar cathode, an $(\eta_c\eta_0)_{planar}$ value is calculated for that operating point. An $(\eta_c\eta_0)_{hollow}$ value is also calculated for each Hall thruster. A star next to the listed $(\eta_c\eta_0)_{hollow}$ value indicates that the source publication did not report either the cathode flow fraction, or the magnet power. In the event that either were missing, an η_c value of 0.935, and a magnet power of $0.02P_d$ were assumed. When calculating $(\eta_c\eta_0)_{planar}$ an η_{heat} value of 0.6 was assumed. Additionally, the planar cathode's emitter is assumed to be made from type 311 BaO.

If "N/A" is listed in the columns corresponding the the minimum cathode diameter and $(\eta_c\eta_0)_{planar}$ values, this indicates that the reported voltage utilization efficiency

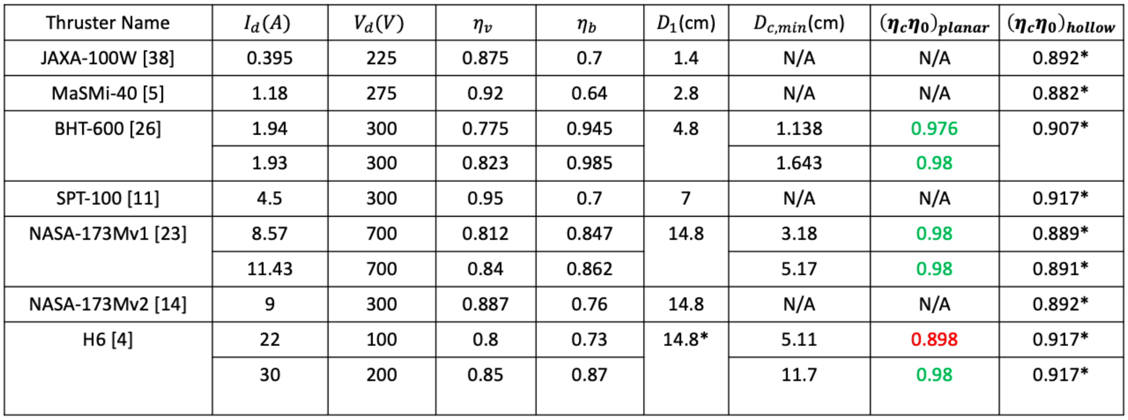

Thruster Name	$I_d(A)$	$V_d(V)$	η_v	η_b	D_1(cm)	$D_{c,min}$(cm)	$(\eta_c\eta_0)_{planar}$	$(\eta_c\eta_0)_{hollow}$
JAXA-100W [38]	0.395	225	0.875	0.7	1.4	N/A	N/A	0.892*
MaSMi-40 [5]	1.18	275	0.92	0.64	2.8	N/A	N/A	0.882*
BHT-600 [26]	1.94	300	0.775	0.945	4.8	1.138	0.976	0.907*
	1.93	300	0.823	0.985		1.643	0.98	
SPT-100 [11]	4.5	300	0.95	0.7	7	N/A	N/A	0.917*
NASA-173Mv1 [23]	8.57	700	0.812	0.847	14.8	3.18	0.98	0.889*
	11.43	700	0.84	0.862		5.17	0.98	0.891*
NASA-173Mv2 [14]	9	300	0.887	0.76	14.8	N/A	N/A	0.892*
H6 [4]	22	100	0.8	0.73	14.8*	5.11	0.898	0.917*
	30	200	0.85	0.87		11.7	0.98	0.917*

Figure 7.1: Measured values of I_d, V_d η_v and η_b for selected operating points of several existing Hall thrusters. If applicable, values of $D_{c,min}$ and $(\eta_c\eta_0)_{planar}$ are calculated for each operating point.

was large enough such that the calculated value of $I_{d,max}$ was negative. It would thus be impossible for a planar cathode to meet the discharge current requirement regardless of its area. This is the case for Hall thrusters such as the MaSMi-40 and the SPT-100.

For Hall thrusters such at the BHT-600 and the NASA-173Mv1, a planar cathode could be a superior alternative to their hollow cathodes. For the listed nominal operating conditions, a planar cathode would be able to provide the discharge currents with emitter diameters that are several times smaller than the inner diameters of the thruster's channels. This leaves plenty of room for a planar cathode and its support structure to be mounted internally on these on these thrusters. Additionally, for each operating point, the calculated value of $(\eta_c\eta_0)_{planar}$ exceeds the measured value of $(\eta_c\eta_0)_{hollow}$. Provided the assumption of a constant anode efficiency holds, switching to a planar cathode would improve the total efficiency and specific impulse of these thrusters.

The H6 Hall thruster provides an example of the incompatibility of planar cathodes with higher discharge current thrusters. For the $I_d = 22A$, $V_d = 100V$ case, a planar cathode is able to provide that current with a cathode diameter that is comfortably smaller than the inner channel diameter. However, even with an oxide emitter, the calculated value of $(\eta_c\eta_0)_{planar}$ is less than the measure value of $(\eta_c\eta_0)_{hollow}$. At an I_d value of 22A, the radiative and emissive power losses will be very large. Meanwhile, since the dischagre voltage is only 100V, the plasma electron heating power will be relatively small. This leaves the thruster with a relatively large required heating power and P_{heat}/P_d ratio. For the $I_d = 30A$, $V_d = 200V$ case, the minimum cathode diameter approaches the inner diameter of the thruster channel, likely making it impossible to mount the planar cathode internally [1].

These results are in line with the findings of the previous section, which is that planar cathodes can potentially improve the efficiency of Hall thrusters whose nominal operating points possess a sufficiently low voltage utilization efficiency and a low discharge current.

---

[1] Reported values of D_1 for the H6 Hall thruster were not found in literature. The value of 14.8cm was used as this thruster has been described as having similar dimensions to the NASA-173M thrusters [17].

Chapter 8

EXPERIMENT

8.1 Purpose of the Experiment

To complement the model presented in chapter 5, an experiment was designed to test a planar cathode. The goal of the experiment was to produce DC plasma discharges between a planar cathode and an external anode. Once formed, measurements would be taken of the cathode heating powers (P_{heat}) required to sustain various discharge currents (I_d), at various discharge voltages (V_d). At each operating point, a Langmuir probe would be used to record the bulk plasma density (n_0) and temperature (T_e). For a standard parallel plate DC discharge, the cathode sheath voltage (V_c) can be roughly approximated as the discharge voltage [22]. Thus, using the measured values of I_d, V_d, n_0, T_e, along with the known geometric and material properties of the cathode and it's support stand, a theoretical value of the required heating power could be calculated using the model outlined in chapter 5. These calculated values of P_{heat} would then be compared with the measured ones. While the physics of a non-magnetized DC discharge is significantly different from that of a Hall thruster's cross-field discharge, this experimental process could at least be used to assess the accuracy of the model, and some of the assumptions made, in a simpler scenario.

The following sections outline both the experimental setup and the experimental procedures in detail.

8.2 Cathode Support Stand

This section describes both the cathode used in the experiment, as well as the stand that was built to support it.

8.2.1 The Cathode

The planar cathode chosen for this experiment was a type 311 oxide cathode purchased from HeatWave Labs [19]. A CAD mockup of this cathode and its dimensions is shown below in figure 8.1. Images of the real cathode are shown in figure 8.2.

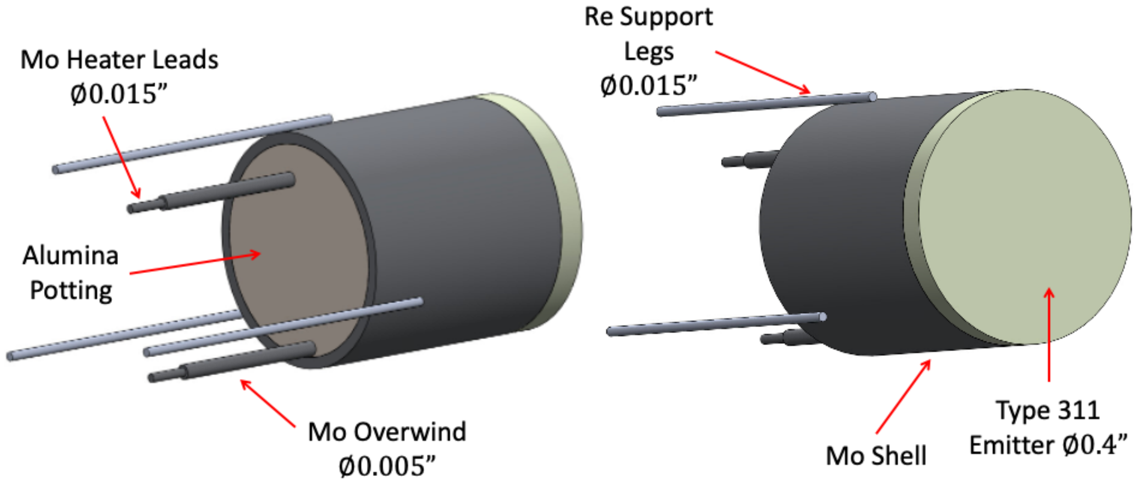

Figure 8.1: CAD model of the cathode used in the experiment.

The active emitter is 0.4" diameter disk comprised of the aforementioned emitting material. This emitter is connected to a thin-walled cylindrical shell composed of molybdenum. The entire length of the cathode body, including both the emitter and the shell, is 0.45". Interior to to the molybdenum shell is a solid cylindrical block of alumina potting. Encased within the alumina potting is a coil made from 0.015" diameter molybdenum wire. The leads of the coil protrude out from the alumina block by 0.35". This coil acts as the cathode's heating element and it's electrically isolated from the molybdenum shell due to the alumina potting. Wound about the exposed portion of each heater lead is a 0.005" diameter molybdenum wire. This over-wind acts to increase the effective surface area of leads, increasing their radiative and conductive heat losses, which helps to cool them during operation. Welded to the exterior of the molybdenum shell are three, 0.6" long, 0.015" diameter, rhenium legs

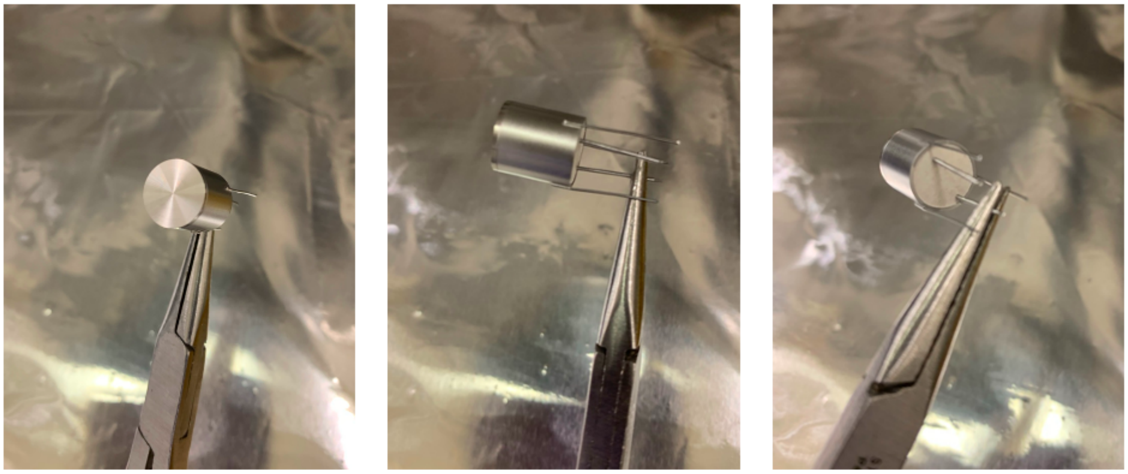

Figure 8.2: Images of the cathode used in the experiment.

spaced 120 degrees apart about the circumference of the shell. These legs extend 0.5” past the body of the cathode. The purpose of the legs is to allow for easier electrical contact with the cathode body.

8.2.2 Electrical Contact with the Cathode

During operation, the temperature of the cathode’s body, heater leads, and legs, easily exceeds 1000C. It’s thus imperative that the electrical conductors in direct contact with the heater leads and support legs can survive these temperatures. Type 304 stainless steel was chosen as the contacting material due to its relatively high melting point of about 1400C.

Two, 5.56” long, 0.042” outer diameter, 0.027” inner diameter, 304 stainless steel tubes were crimped to the base of both of the cathode’s heater leads, below the overwind. A third steel tube of the same dimensions was also crimped to one of the three support legs. This tube length was chosen to ensure a significant temperature gradient between the crimped end of the tubes, which will be near the cathode’s temperature during operation, and the far ends, which will have lower melting point conductors in contact with them. A diagram of this configuration is shown in figure 8.3

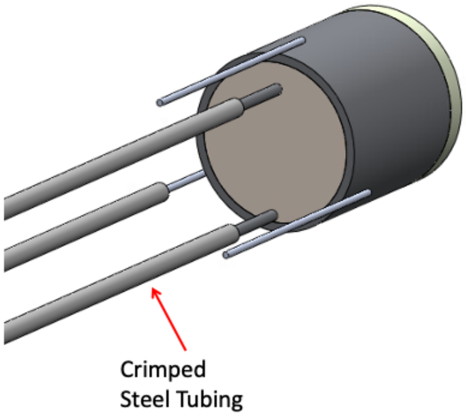

Figure 8.3: CAD model of the planar cathode with the crimped steel tubing connections.

8.2.3 Design of the Cathode Support Stand

To support the cathode and the steel tubing, a mount was constructed to hold all of the components. The main portion of the mount consists of two, 0.07” thick, stainless steel support stands. The stands were first water-jetted out of a stainless steel sheet into the two shapes shown in figure 8.4a. Afterwards, they were both bent into the shapes shown in figure 8.4b. Both stands rest on a series of two, 0.08” thick, L-shaped stainless steel rails.

During operation, the cathode body will be held negatively with respect to ground, at the discharge voltage. Meanwhile, the metallic stands are left electrically floating. It’s thus imperative that the cathode, it’s crimped steel tubing, and the stands remain electrically isolated from each other. To ensure this, a ceramic mount was created to isolate the cathode from the stainless steel. The top portion of the front steel stand is sandwiched between two, 0.25” thick, macor ceramic plates. At the base of the forward facing macor plate is a 0.25” thick bar of macor. The bar has a 0.4in”

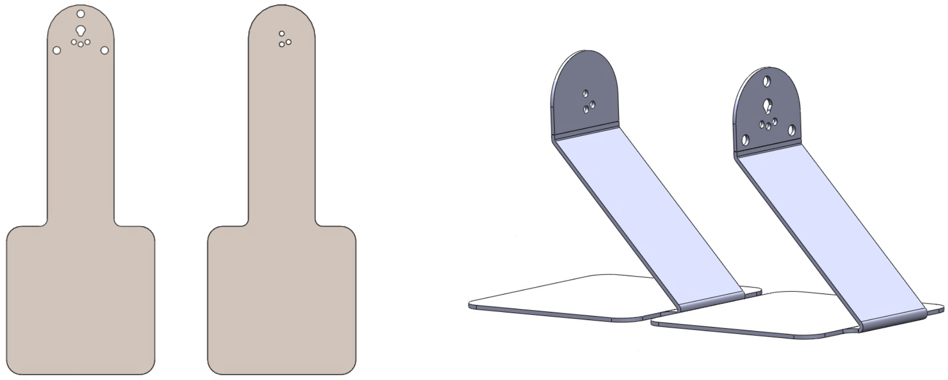

(b)

(a)

Figure 8.4: Stainless steel stands before (a) and after (b) bending.

diameter, semi-circular concavity for the cathode's body to rest on. The macor pieces and the front-facing stand have holes milled through them in order to accommodate the 3/16" diameter screws used to hold the pieces together. Macor was chosen for it's low coefficient of thermal expansion and large dielectric strength. A CAD model of the stainless steel stands with the macor plating is shown in figure 8.5.

Additional holes were milled into both the macor plates and the steel supports to accommodate the placement of five alumina tubes. The purpose of the alumina tubes is to electrically isolate the cathode's legs and heater leads, as well as their corresponding crimped steel tubes, both from each other and from the steel support stand. The alumina tubes containing the long, straight segments of steel tubing were 5.34" long, and possessed an outer diameter of 0.125" and an inner diameter of 0.0625". These alumina tubes were supported on their far ends by holes milled into the second steel support stand. With a dielectric strength of 220V/mil, this tube thickness can insulate up to 6,820V, far exceeding the range of discharge voltages tested in this experiment. The alumina tubes containing the un-crimped cathode legs were 0.57" long, spanning only the length of the two macor plates and front steel

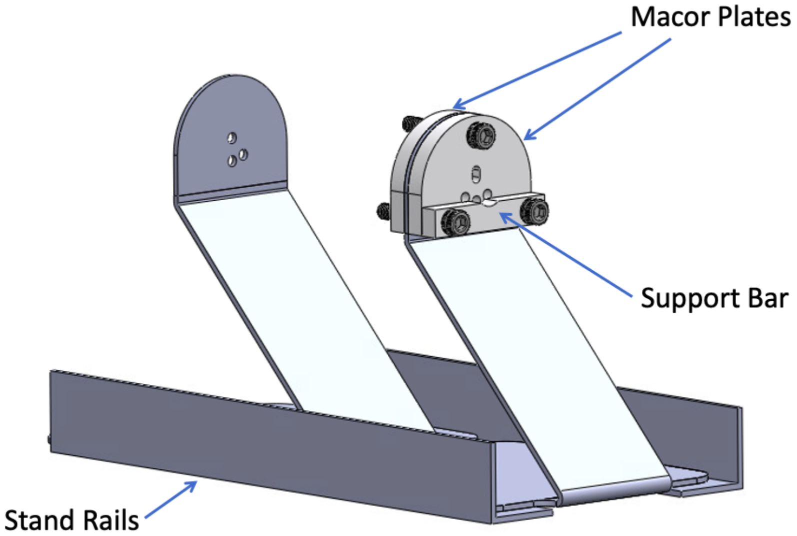

Figure 8.5: CAD model of the stainless steel stands with the attached macor plates.

stand. All five of these tubes were potted into the holes of the front-facing macor plate using using Contronics Corporation's Resbond 940LE ceramic adhesive. Figure 8.6 shows a CAD model of the cathode stand with the alumina tubing installed. The second image shows a close-up of the front macor plate, with labels indicating where the cathode's leads and legs insert into.

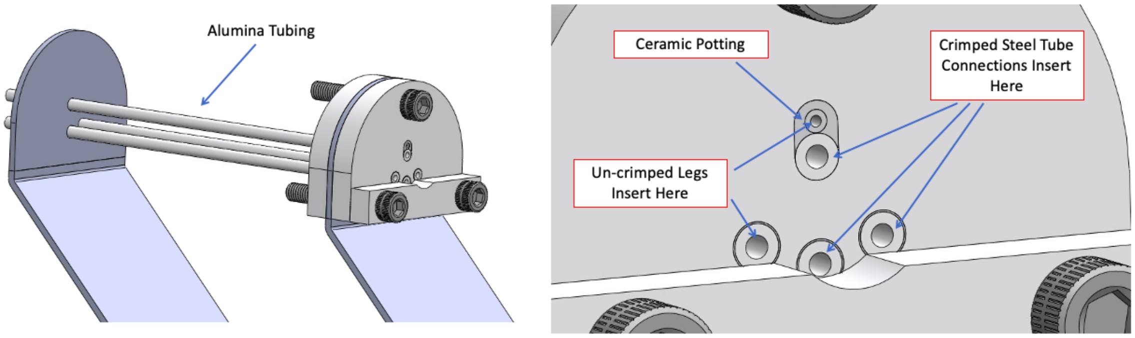

Figure 8.6: CAD model of the cathode stand with the alumina tubing. The second image indicates where the cathode legs/leads insert into.

The placement of the holes were chosen such that the cathode's legs and heater leads would sit concentrically inside the alumina tubes while the cathode body rests on the semicircular cavity on the macor bar. A CAD model of the stand, with the cathode and steel tubing connections installed, is shown in figure 8.7. The steel tubes protrude out from the alumina tubing by 0.5". This is to allow for electrical contact to be made with them.

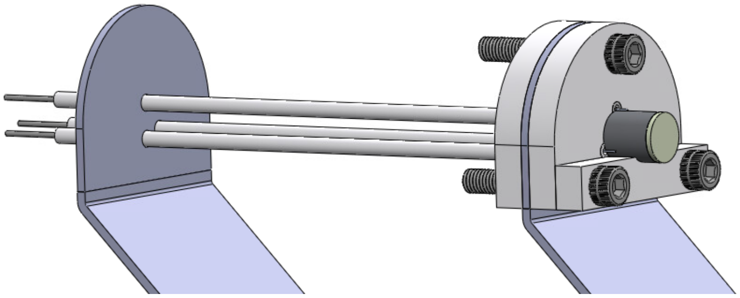

Figure 8.7: CAD model of the cathode stand with the cathode and steel tubing installed.

8.2.4 Stand Redesign

During initial testing, the support leg with the crimped steel tube became detached from the cathode body. It's suspected that as the cathode was heated and cooled over a number of cycles, the steel tube crimped to the leg in question underwent notable longitudinal thermal expansion and contraction. This process would have caused it to push and pull on the cathode leg, until the induced stress on the weld point caused it to snap off. A diagram showing this process is presented in figure 8.8.

As part of the re-design, a Z-shaped, 304 stainless steel tubing bend was crimped to one of the surviving support legs. The steel tubing used in this bend possessed an outer diameter of 0.05" and an inner diameter of 0.033". This is roughly a thirty-six percent increase in cross-sectional area compared to tubing used to make contact

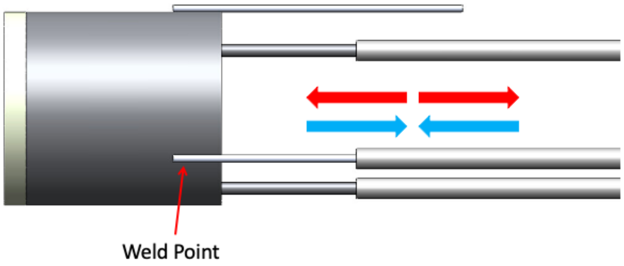

Figure 8.8: Diagram showcasing the thermal expansion and contraction of the crimped tubing.

with the damaged support leg. This was done to both reduce the resistivity of the connection and lower the resistive heating caused by the discharge current, and to increase the radiative and conductive power losses of the connection. The z-shape was chosen so that during thermal expansion the connection can deform inward, reducing the stress on the weld point. This z-bend connection is show in figure 8.9.

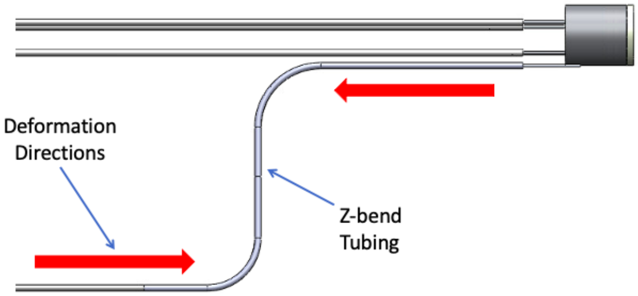

Figure 8.9: CAD model of the planar cathode with the z-bend connection.

Once the z-bend was incorporated into the design, an additional mounting system was included on the cathode stand to support it. A diagram of the updated cathode stand is shown in figure 8.10. A photograph of the actual cathode stand with the cathode inserted is shown in figure 8.11.

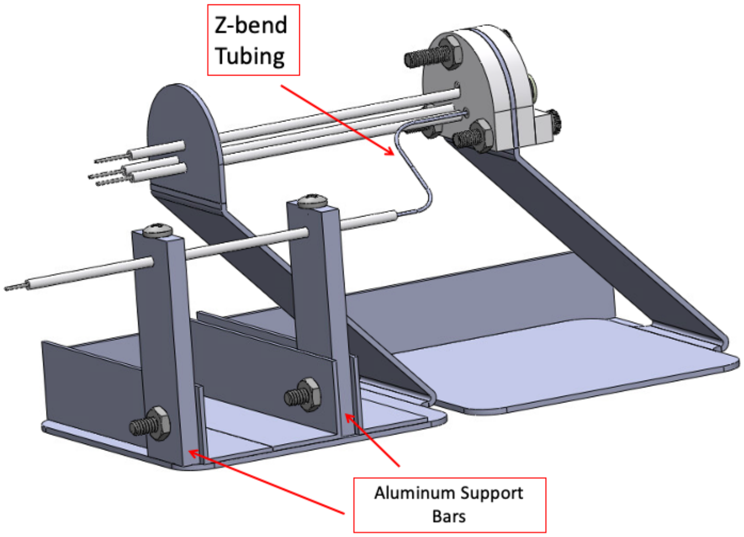

Figure 8.10: CAD model of the cathode stand with the mounting system for the z-bend included.

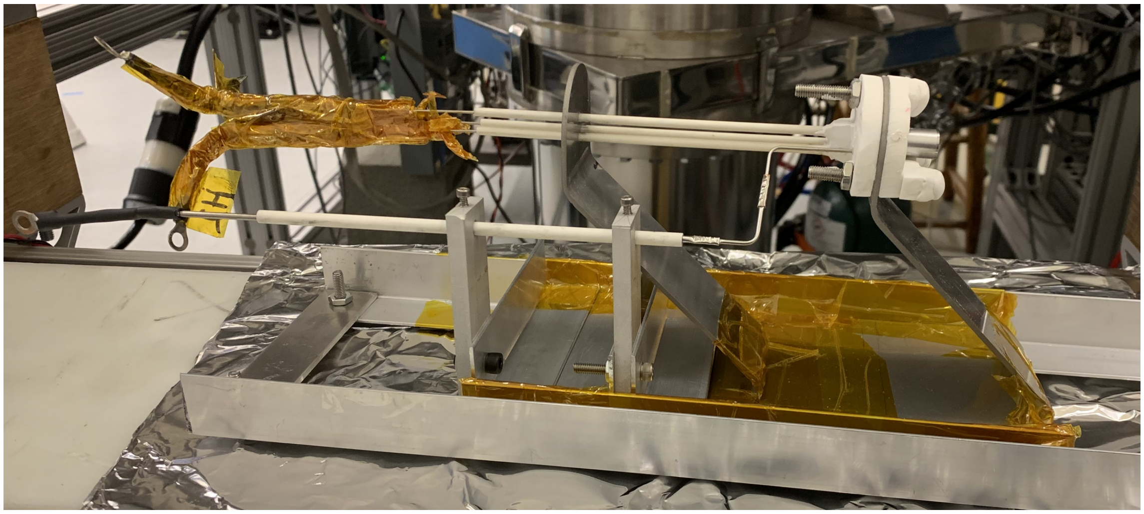

Figure 8.11: Photograph of the cathode stand with the cathode installed.

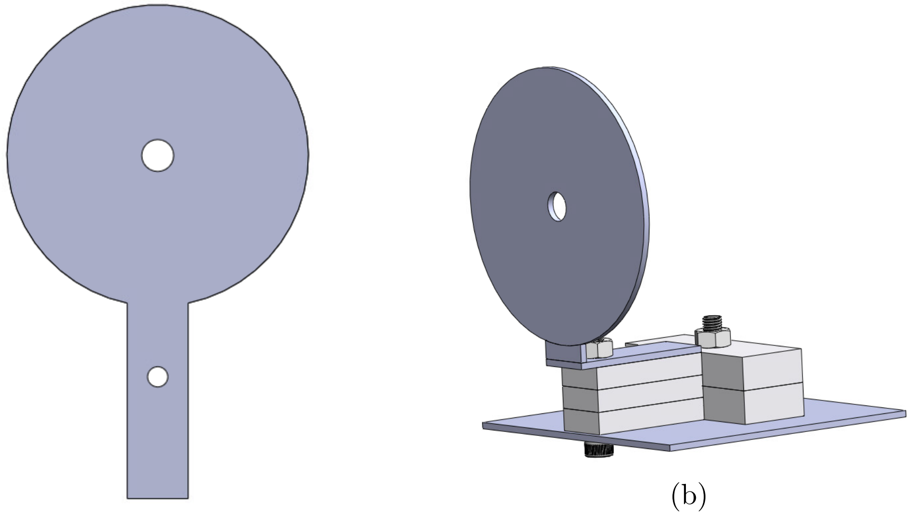
(a)

(b)

Figure 8.12: CAD model of the anode.

8.3 Experimental Setup

8.3.1 The Anode

The circuit's anode is a 3.71" diameter, disc connected to a 2.4" long, 0.75" wide rectangular tab. The anode was first water-jetted out of a 0.09" thick stainless steel sheet into the shape shown in figure 8.12a. It was then bent into the design showcased in figure 8.12b.

The base of the anode stand is a 4" x 4" stainless steel square with two holes milled through it to accommodate 1/4" diameter screws. The anode is elevated off the base using three, 0.3" thick, Teflon spacers. The screw holding the the components together ensures that the anode and the square base are in electrical contact. This screw is also used to hold a ring terminal. In this experiment, the anode its base were held at ground potential. Lastly, two more Teflon blocks are fastened to the rear end of the stand to weigh it down.

The anode and the cathode stand rest on a pair of 18" long, L-shaped stainless steel rails. The anode was positioned such that its face was 6.5cm away from the surface of the cathode. Figure 8.13 shows a photograph of the entire experimental assembly.

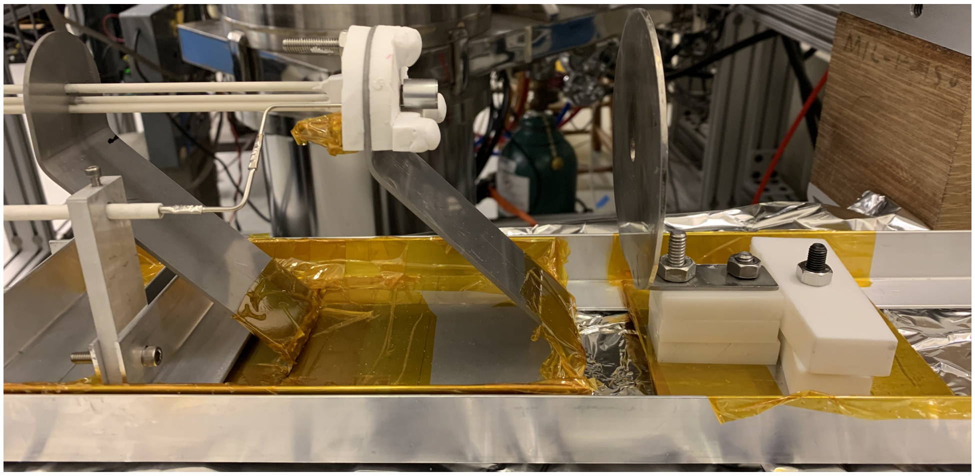

Figure 8.13: Photograph of the full experimental assembly.

8.3.2 The Electrical Circuit

The discharge circuit is shown in figure 8.14. Within the discharge circuit, the anode is grounded. Meanwhile the cathode's emitter, and by extension the molybdenum body and support legs, are biased negatively with respect to the anode by the discharge voltage.

The power supply originally chosen for the discharge circuit was TDK-Lambda's GEN600-2.6 model which is a 600V, 2.6A, DC supply. However, as will be discussed further in a later section, there were difficulties in igniting the discharge with only 600V. In later testing, Spellman's model SL10N300 -10kV, 30mA, DC supply was used as the discharge supply instead.

When using the 600V supply, a diode was connected in parallel with the supply's

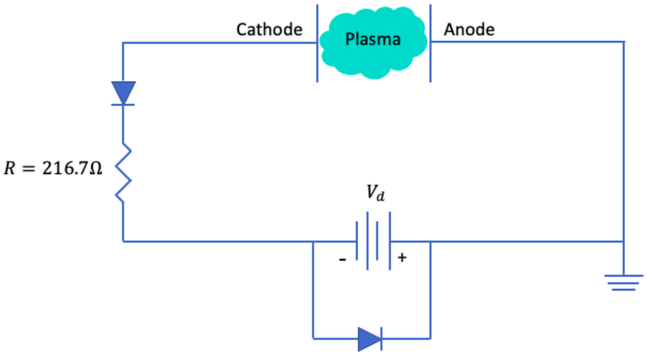

Figure 8.14: Diagram of the discharge circuit connecting the anode and cathode.

output. The purpose of this diode was to protect the supply from large inductive voltage spikes. This diode had a reverse voltage rating of 800V and a current rating of 4A, enough to exceed the output of the supply. A second diode with the same properties was connected in series with the supply to ensure current only flowed in the forward-biased direction. Lastly, a 216.7Ω resistor was connected in series with the supply. The purpose of this resistor was to protect the power supply from any current spikes once the plasma discharge was formed. The value was chosen such that the current in the circuit would never exceed 2.6A, even with 600V applied between the anode and cathode. Additionally, the resistor had a power rating of 2000W, which comfortably exceeds the total output of the supply.

As mentioned in section 8.2.1, the heater leads are electrically isolated from the molybdenum body due to the alumina potting. Hence, the cathode's heating circuit is separate from the discharge circuit. No additional components were utilized within the heater circuit, just the wiring necessary to connect the heater leads to the heater supply. 10AWG wire was used for both the discharge and the heating circuits. This wire possessed an outer layer of silicon rubber insulation rated up to 15kV.

The power supply chosen as the heater supply was GW Instek's model GPC-3030D. This power supply consists of two 30V, 3A DC supplies that can be connected in either series or parallel, to double either the voltage or current output. Parallel mode was chosen to allow heater coil currents of up to 6A.

Since the layer of potting separating the cathode's molybdenum shell and heater leads is thin, there was concern that they would come into contact with the cathode body. If this were to occur while the discharge supply is on, the output terminals of the heater supply would be raised up to the discharge voltage. This could lead to arcing between the supply outputs and the grounded chassis. To prevent this, the heater supply was connected to the wall through an isolation transformer. The transformer chosen was Stangenes Industries' model SIT 300-100. When connected in this manner, both the chassis and the supply outputs are left floating. To keep it electrically isolated during operation, a box made from 3/16" thick acrylic plastic and 80/20 aluminum rails was constructed to hold the heater supply. A photograph of this setup is shown in figure 8.15. Once the discharge supply is turned on, the door to the acrylic box is closed to avoid any contact with the heater supply's chassis.

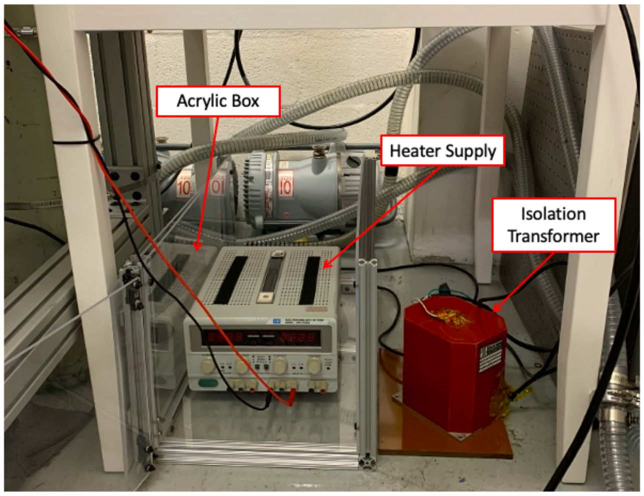

Figure 8.15: Image of the heater supply, the insulating box, and the isolation transformer.

8.3.3 The Vacuum Chamber

A photograph of the vacuum chamber housing the experiment is shown in figure 8.16.

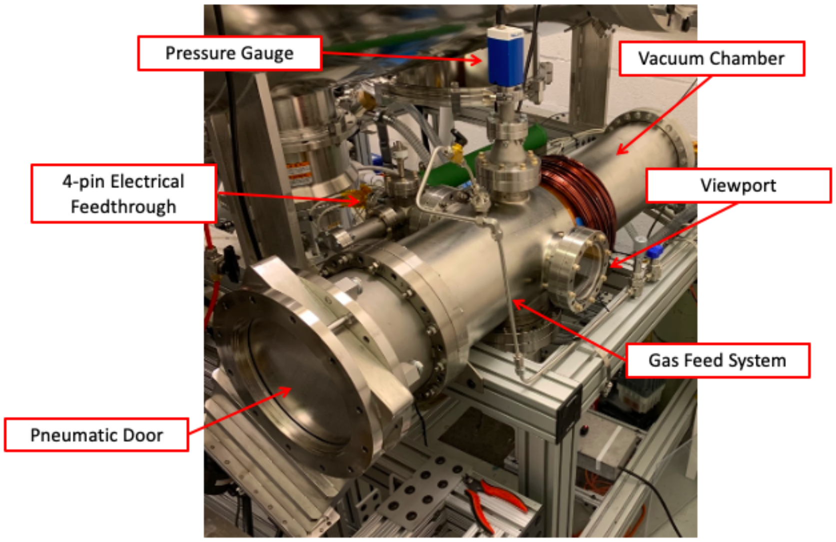

Figure 8.16: Image of the vacuum chamber with its various components labeled.

This vacuum chamber is an 8” inner diameter (I.D), 44” long stainless steel tube, capped with two 10” outer diameter (O.D) ConFlat (CF) flanges. A pneumatic door is mounted on the front flange, while the rear flange is sealed by a 10” O.D blank CF flange. The entire chamber is mounted on 2” thick 80/20 aluminum bars.

On the bottom of the chamber, midway along its length, is an 8” O.D CF port. Connected to this port is a turbo-molecular vacuum pump. The pump used was Pfeiffer Vacuum’s model TC100. Connected to the turbo-molecular pump is Dayton Electric Mfg Company’s model 5K340X roughing pump.

On the right side of the chamber, midway along its length, is a 6” O.D CF viewport. The experimental assembly was positioned such that the plasma discharge would be visible from this viewport.

Connected to a port the left hand side of the chamber is a 4pin CF electrical feed-through purchased from Kurt J. Lesker company. This feed-through has four, 0.05" diameter, copper rods that protrude from both sides of the flange. These rods are electrically isolated from both the flange and each other. Each copper rod has ring terminals crimped to both its ends. On the vacuum side of the flange, the ring terminals connect to wires that run throughout the chamber and attach to the heater, cathode and anode connections. On the air side, the ring terminals connect to the wires that make up the heating and discharge circuits.

On the top of the chamber is a CF port to which the chamber's pressure gauge is connected. The gauge used for this experiment was Kurt J. Lesker Company's model KJLC-CCPG combination gauge. This gauge was connected to the model KJL-SPARC-3.0 power supply and display unit from the same company.

Lastly, there is a second, diagonally positioned, 1.25" O.D CF port on the top of the chamber. Connected to this port is a 1/4" I.D Swagelok feed-through. The chamber's gas feed system connects to this feed-through.

8.3.4 The Gas Feed System

For this experiment, argon was chosen as the test gas. A bottle of argon gas was mounted, via hose clamps, to the same 80/20 structure as the chamber. Connected between the gas bottle's regulator and the vacuum chamber's Swagelok feed-through, is the chamber's gas feed system. A schematic of this feed system is shown below in figure 8.17.

The gas feed lines are made from 1/4" O.D, 1/8" I.D stainless steel tubes. A gate valve is placed right near the Swagelok feed-through so the chamber can be sealed off from the gas feed lines if desired. A needle valve is used to control the gas flow rate into the chamber. Various Swagelok elbows and tees were used to connect the steel tubes.

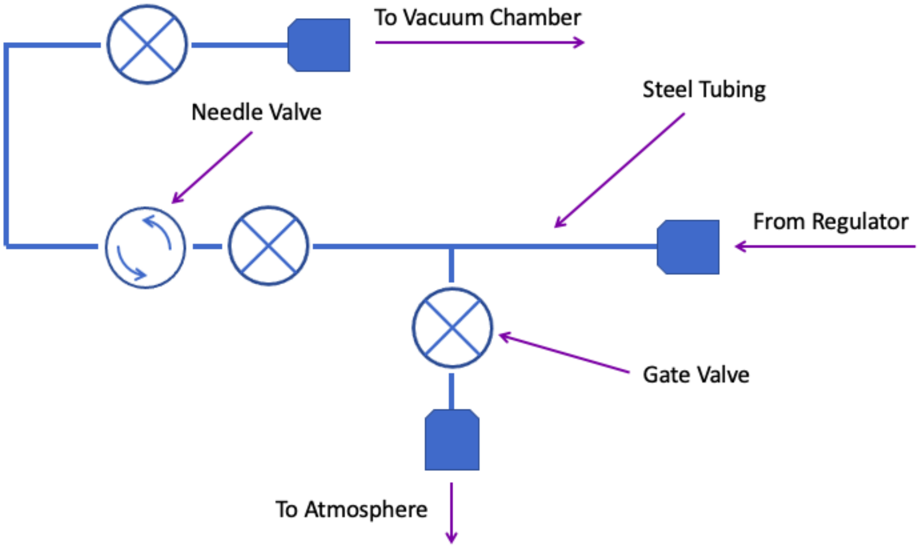

Figure 8.17: Schematic of the gas feed system.

8.4 *Experimental Procedures*

8.4.1 Chamber Pump-down

Once the chamber is sealed with the cathode and anode inside, the roughing pump is turned on and ran by itself until the chamber is brought down to a pressure of around 0.1 Torr. From atmosphere this process takes about one hour. Once this pressure is achieved, the turbo-molecular pump is turned on and the chamber pumped down to an ultimate base pressure of 2.8×10^{-7} Torr over a period of about one day. During this pump down process, all of the gate valves in the gas feed system (barring the one that opens to atmosphere), and the needle valve are completed open, so the gas feed lines can be brought to vacuum as well.

8.4.2 Cathode Bake-out

Oxide cathodes require an extensive bake-out procedure in order to both remove atmospheric moisture from the emitter, and evolve the impregnate from the porous tungsten matrix to the to the emitter surface. Described in this section are the steps required to properly bake-out the cathode, as specified by HeatWave Labs [20].

Once the chamber reaches it's base pressure, the heater supply turned on and the output voltage is set to 0.25V. With current now passing through the heater coil, the cathode, and by extension the ceramic mount, are restively heated. At this point, the cathode and the surrounding structure begin out-gassing, and the pressure in the chamber rises above the base pressure. The system is left at this heating power for fifteen minutes while the chamber pressure is monitored. If the pressure rises above 1.0×10^{-6} Torr, the cathode runs the risk of being poisoned, and the heating power must be reduced until the pressure level drops. If at the end of the fifteen minutes the pressure has not exceeded this limit, the supply voltage is increased by an increment of 0.25V. This process of incremental voltage increases, while ensuring the chamber pressure stays on the order of 10^{-7} Torr, continues until the heater supply's output voltage is 7.5V. Based on the data sheet provided by the HeatWave Labs, this corresponds to a cathode temperature of around 1100C. Once this temperature is achieved, the bake-out process is complete and the emitter can be considered fully out-gassed and activated. Overall, this process took over 30 hours spread out over a week and a half.

Once the cathode has been activated, it can brought back up to emissive temperatures rather quickly. The bake-out process only needs to be performed again if the cathode is exposed to atmosphere.

8.4.3 Plasma Ignition Procedures

This section outlines the procedures followed for igniting the plasma discharge. It's assumed the bake-out process from the previous section has already been completed.

The cathode is heated to around 1100C, using the data sheet provided with the cathode as a reference. An image of the cathode operating at this temperature is shown in figure 8.18. The door to heater supply's insulated box is then closed for safety. The valve on the argon bottle is opened to allow gas into the feed lines. Every gate valve (except for the one that opens to atmosphere) in the feed system is opened, while the needle value is used to control the gas flow and thus the argon pressure in the chamber. Once the desired chamber pressure is achieved, the output voltage on the discharge supply is turned on.

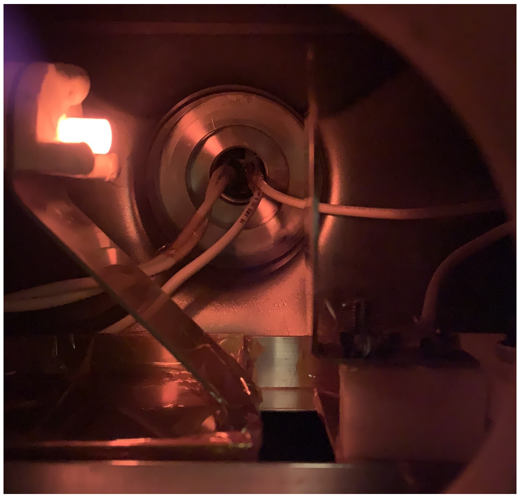

Figure 8.18: Image taken of the cathode at around 1100C.

8.4.4 First Plasma

As mentioned in a previous section, a 600V supply was originally chosen as the discharge supply. During initial testing it was found that 600V was an insufficient output voltage to ignite a discharge. This voltage was tested for argon pressures ranging from 10^{-6} Torr to 10^{-2} Torr and for cathode heating powers ranging from 15W to 26W (which correspond to cathode temperatures ranging from 900C to 1100C according to the data sheet). Higher chamber pressures were not tested to avoid over-heating the turbo-molecular pump. During these tests, no plasma was visible in the chamber and the discharge supply read zero current.

Following these initial tests, the 600V supply in the discharge circuit was replaced by a 10kV supply which initially yielded more positive results. Figure 8.19 shows the first successful plasma discharge produced using this experimental setup.

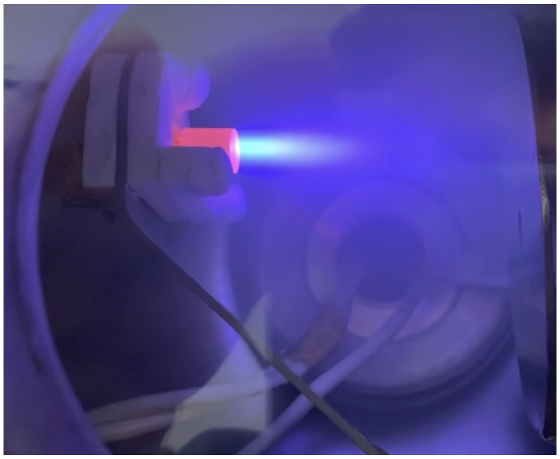

Figure 8.19: Image of the first plasma discharge.

The above discharge was achieved at a chamber pressure of 10^{-2} Torr, a cathode heating power of 21.85W, and a discharge voltage of 900V. As the plasma began to form, the discharge current rose to 30mA, which is the supply limit. Once ignited, the discharge was able to persist at the same current level and with the visual profile even as the output voltage was lowered all the way to just 60V. Only once the output voltage was lowered below 60V did the brightness of discharge diminish and the current dip below 30mA. At around 20V, the plasma fully extinguished and the discharge current dropped to zero. A similar test was ran where the discharge voltage was raised back to 900V and held there while the chamber pressure was lowered instead. It was found that the discharge continued to persist until the chamber pressure was lowered to about 1.5×10^{-3} Torr, at which point the discharge current dropped below the supply limit and the plasma began to extinguish.

8.4.5 Subsequent Testing

After the first successful plasma ignition showcased in the previous section, the plasma was unable to be re-ignited in the same manner. On subsequent testing, when operating at the same argon pressure, cathode heating power, and discharge voltage, the measured discharge currents were significantly smaller, and the discharges were far less bright.

Attempts to achieve the same discharge, by raising both the cathode heating power and discharge voltage, were made. Figure 8.20a showcases the plasma discharge at a heating power of 21.85W, and a discharge voltage of 1.5kV. Under these conditions, the measured discharge current was only 0.6mA. Instead of a large plume expanding out from the cathode surface, the plasma discharge took the form of a thin angled beam jutting out from the norther part of the cathode's face. As a follow up, figure 8.20b showcases the plasma discharge at a heating power of 24.01W, and a discharge voltage of 1.7kV. Under these conditions, the discharge current rose slightly, to 1.1mA. The plasma discharge had the same structure as the previous test, but was slightly brighter. At this point, it was assumed that something had gone wrong with the cathode's emissive surface, and efforts to re-ignite the plasma we're halted.

8.4.6 Cathode Re-activation

After discussing the above issues with an engineer from HeatWave Labs, the likely cause of the cathode's failure was deemed to be damage from ion bombardment. As discussed in section 3.2.1, ions bombarding the emitter surface can sputter away the barium-oxygen monolayer. At larger discharge voltages however, ions can begin sputtering the tungsten matrix itself. In this scenario, sputter-induced overheating of the tungsten can rapidly deplete the emission mix, or, in the worst case scenario, melt the tungsten and seal the pores. The issue of the mono-layer being sputtered off the surface can be solved by simply re-activating the cathode, and allowing the monolayer

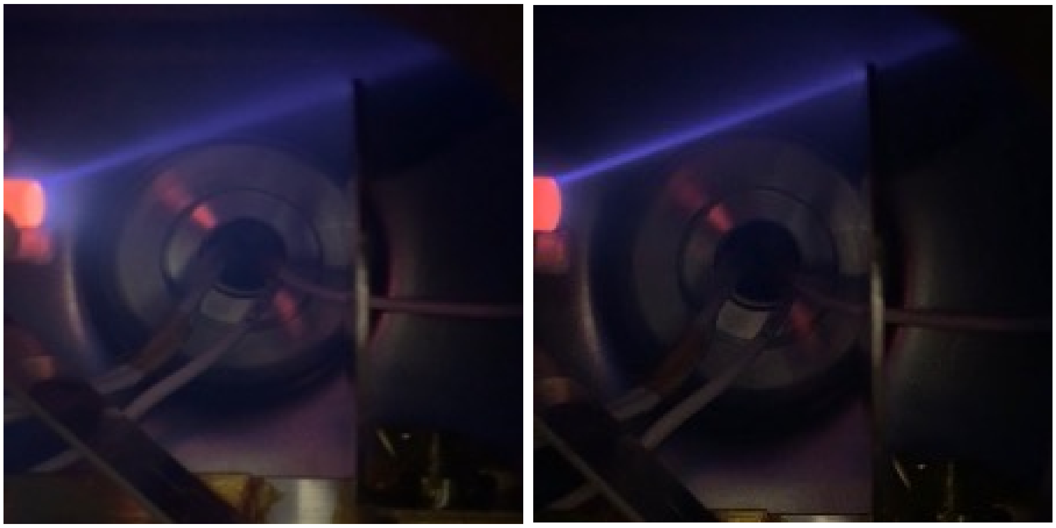

(a) $P_{heat} = 21.85W$, $V_d = 1.5kV$, and $I_d = 0.6mA$

(b) $P_{heat} = 24.01W$, $V_d = 1.7kV$, and $I_d = 1.1mA$

Figure 8.20: Photos of subsequent discharge attempts.

to re-form. Sputtering of tungsten however, can result in permanent damage to the cathode.

In an attempt to re-active the cathode, the bakeout-process outlined in section 8.4.2 was performed again. Since the cathode and its support structure had been fully out-gassed from the first bake-out, and it had never left vacuum since, there was no concern of the pressure in the chamber exceeding $1x10^{-6}$ Torr. In light of this, the voltage on the heating supply was increased at a rate of 0.25V per five minuets instead of fifteen, up to a voltage of 8.5V. According to the cathode's data sheet, this corresponds to a temperature of around 1200C. The higher bake-out temperature was chosen in order to assist with reactivation.

Despite repeating the activation process, the plasma was still unable to ignite at sub-kilovolt discharge voltages. This likely means that the original series of high voltage tests led to the sputtering of tungsten from the cathode's surface, permanently damaging the cathode. Figures 8.21a and 8.21b showcase images of the cathode's

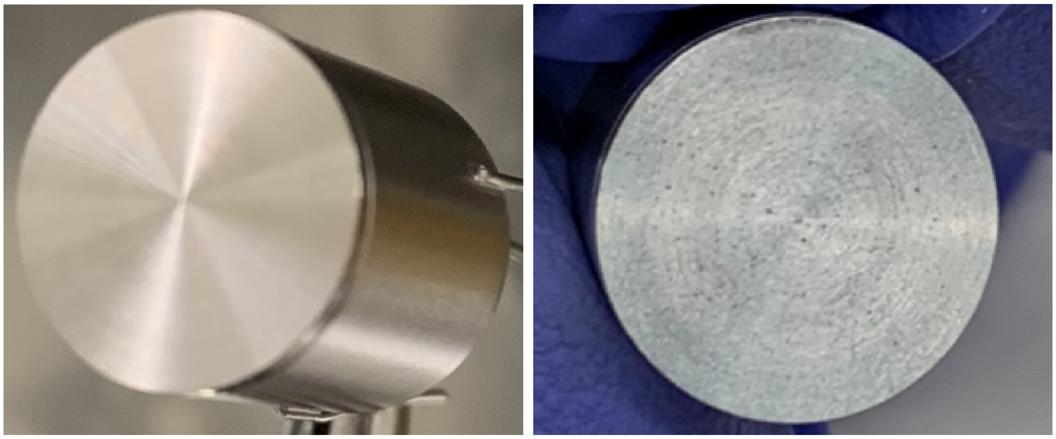

(a) (b)

Figure 8.21: Surface of the planar cathode before (a) and after (b) testing.

surface, before and after all the testing. In the "after" photo, it can be seen that the cathode surface is heavily discolored and grainy, a possible indication of sputtering damage. Following the malfunction of the cathode, the experimental component of this thesis was no longer pursued.

Chapter 9

CONCLUSION

Working under the assumptions of the model presented in chapter 5, it's been shown that, under the correct conditions, $(\eta_c \eta_0)_{planar}$ can exceed $(\eta_c \eta_0)_{hollow}$ for a given Hall thruster. The conditions under which $(\eta_c \eta_0)_{planar}$ and $I_{d,max}$ are maximized were presented in chapter 6.

The heating provided by a Hall thruster's plasma to the surface of a centrally mounted planar cathode was found to be substantial. When using a relatively good emitter such as type 311 BaO, this heating can be sufficient to maintain the required surface temperature over a wide range of operating conditions. In these circumstances, a planar cathode can be operated with no external heating power, making it a superior option to a hollow cathode as it consumes no propellant.

The primary draw-back of planar cathode's is the ease at which they run into the space charge limit. The properties of the thruster plasma local to a centrally mounted planar cathode are unfavorable for maximizing the emitted current. This places the burden of extracting current on the cathode coupling voltage. In order to draw currents from a planar cathode of the magnitude typically required by Hall thrusters, it's necessary that the Hall thruster possess a sufficiently low voltage utilization efficiency.

With these benefits and drawbacks in mind, planar cathodes could be a superior alternative to hollow cathodes on low current Hall thrusters that possess low voltage utilization efficiencies at their nominal operating conditions.

9.1 Limitations of the Model and Future Work

While the conditions under which planar cathodes can function were found to be limited, it's important to note that there were a number of simplifying assumptions baked into the model. The first, and most prominent of which, was the assumption that a Hall thruster's anode efficiency is unaffected by the type of cathode equipped. This assumption was not rigorously justified, and it's possible that one or more of the anode efficiency terms could change in response to changing the cathode geometry.

9.1.1 Voltage utilization efficiency

A likely anode efficiency term to be cathode-dependent is the voltage utilization efficiency. As discussed previously, this term is related to the cathode-coupling voltage, the voltage drop between the cathode and the beam. In a hollow cathode, the coupling voltage is split over two regions [18]. First, there's the voltage drop between the emitter surface and the cathode orifice, V_{int}, which draws the electrons from the emitter into the cathode plume. Second, there's the voltage drop between the cathode orifice and the thruster plume, V_{plume}, which is responsible for drawing electrons from the cathode plume into the channel discharge. This is expressed mathematically in the equation below.

$$V_{cc,hollow} = V_{int} + V_{plume} \tag{9.1}$$

For a planar cathode, the coupling voltage is the sum of the voltage drop across the cathode sheath (V_c), and the voltage drop between the sheath and thruster plume (V_r), as dictated by equation 5.49. The properties of the properties of the plasma internal to a hollow cathode, and in s hollow cathode's plume region, will differ notably from the properties of the plasma near a planar cathode's surface, due to the geometry of the hollow cathode, and the high neutral density resulting from the mass flow injected into the hollow cathode. This could result in a differing plasma resistivity, at least in the regions near each cathode's emitter, which in turn would result in $V_{int} + V_{plume}$ differing from $V_c + V_r$ for the same applied discharge voltage. A more accurate quantity to compare between cathode types would then be $(\eta_v \eta_c \eta_0)$.

A limitation of the assumption of constant η_v was already presented back in section 6.1.2. For a voltage utilization efficiency of 90%, a negative value of the maximum discharge current was predicted for most discharge voltages. This is an un-physical result, and so it was assumed that if a thruster's η_v value was too large, then it would not ignite with a planar cathode. It's possible a thruster possessing a large η_v while operating with a hollow cathode, could still ignite under the same conditions (V_d, $\dot{m}_a$, etc...) while operating with a planar cathode, but the potential would be distributed in such as way as to yield a lower η_v value.

Theoretical models calculating the coupling voltage of a planar-cathode equipped thruster do not yet exist in literature. A numerical model that could calculate $V_{cc,planar}$ as a function of the thruster's other discharge properties could be extremely useful for this analysis.

9.1.2 Future Experimental Work

Existing examples of experimental efforts utilizing planar cathodes on Hall thrusters are extremely limited. To the author's knowledge, only one such example exists. In 2004, the company Alta SpA developed a 100W Hall thruster prototype with an externally mounted planar cathode [1]. Coincidentally, the planar cathode used on this Hall thruster was purchased from HeatWave Labs. Images of this Hall thruster are shown below in figures 9.1a and 9.1b.

A planar cathode was selected for this thruster in an attempt to take advantage of the benefits listed in section 5.2 (higher specific impulse and reduced system mass). Additionally, the thruster was expected to have a discharge current of only 0.5A at it's nominal operation point, so the space charge limitations of a planar cathode would not be as much of a hindrance.

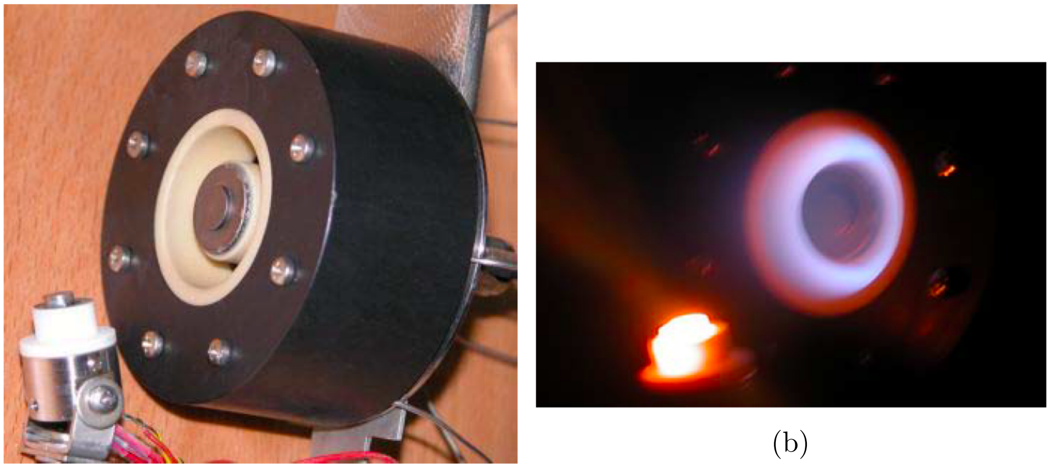

(a) (b)

Figure 9.1: Images of the HT-100 Hall thruster developed by Alta SpA. The right image showcases the Hall thruster during operation [1].

During testing the planar cathode malfunctioned, and the thruster was not able to properly ignite. Only discharge currents of around 0.1A were measured. The authors suspect the cathode was poisoned during the activation process, increasing it's work function and limiting it's emissive capabilities. In an attempt to increase emission, the cathode's temperature was increased to over 1200C. This eventually resulted in the cathode failing due to overheating. In subsequent testing of this same thruster, the planar cathode was replaced with a hollow cathode [2].

Given the lack of existing experimental data on planar cathode-equipped thrusters, future experimental efforts are needed to test the viability of planar cathodes. The ideal experiment to complement the model presented in this thesis would be to design a Hall thruster capable of supporting both a centrally mounted hollow cathode, and a centrally mounted planar cathode, which could be interchanged at will. Ideally this would be a low power Hall thruster designed to operate a low discharge currents to avoid space charge issues with the planar cathode. The thruster would first be operated with the hollow cathode, and measurements of the seven efficiency terms would be taken at different operating points. Following this, the thruster would be ran with the planar cathode, and measurements of the efficiency terms would be taken at under the exact same operating conditions. This experiment could give insight as to which, if any, of the efficiency terms are truly cathode-agnostic. Additionally, for each operating point, measured values of η_v, η_b, I_d, V_d, and P_{mag} could be used to calculate a theoretical value of $(\eta_c\eta_0)_{planar}$ using the model of chapter 5, provided η_{heat} is known. This theoretical value could then be compared to the measured value of $(\eta_c\eta_0)_{planar}$ to assess the accuracy of the method used to calculate this quantity.

BIBLIOGRAPHY

[1] Leonardo Biagioni, Matteo Berti, Ugo Cesari, Massimo Saverdi, and Mariano Andrenucci. Development and preliminary characterization of a low power hall thruster prototype. In *40th AIAA/ASME/SAE/ASEE Joint Propulsion Conference and Exhibit*, page 3944, 2005.

[2] Leonardo Biagioni, Ugo Cesari, Massimo Saverdi, and Mariano Andrenucci. Development status of the ht-100 miniaturized hall effect thruster system. In *41st AIAA/ASME/SAE/ASEE Joint Propulsion Conference & Exhibit*, page 3875, 2005.

[3] Jean-Pierre Boeuf. Tutorial: Physics and modeling of hall thrusters. *Journal of Applied Physics*, 121(1):011101, 2017.

[4] Daniel L Brown, C William Larson, James M Haas, and Alec D Gallimore. Analytical extraction of plasma properties using a hall thruster efficiency architecture. In *Proceedings of the 30th International Electric Propulsion Conference, Florence, Italy*, pages 17–20, 2007.

[5] Ryan William Conversano. *Low-power magnetically shielded Hall thrusters*. University of California, Los Angeles, 2015.

[6] René Cortenraad, AW Denier van der Gon, HH Brongersma, G Gärtner, and A Manenschijn. Surface analysis of thermionic dispenser cathodes. *Applied surface science*, 191(1-4):153–165, 2002.

[7] James L Cronin. Practical aspects of modern dispenser cathodes. 1979.

[8] JL Cronin. Modern dispenser cathodes. In *IEE Proc*, volume 128, pages 19–32, 1981.

[9] Käthe Dannenmayer. *Scaling laws and electron properties in Hall effect thrusters*. PhD thesis, Université d'Orléans, 2012.

[10] DC Faircloth. Particle sources. *arXiv preprint arXiv:2103.13231*, 2021.

[11] Dan M Goebel and Ira Katz. *Fundamentals of electric propulsion: ion and Hall thrusters*. John Wiley & Sons, 2008.

[12] Dan M Goebel, Ron M Watkins, and Kristina K Jameson. Lab6 hollow cathodes for ion and hall thrusters. *Journal of Propulsion and Power*, 23(3):552–558, 2007.

[13] GD Hobbs and JA Wesson. Heat flow through a langmuir sheath in the presence of electron emission. *Plasma Physics*, 9(1):85, 1967.

[14] Richard Hofer and Alec Gallimore. Efficiency analysis of a high-specific impulse hall thruster. In *40th AIAA/ASME/SAE/ASEE Joint Propulsion Conference and Exhibit*, page 3602, 2004.

[15] Richard R Hofer, Sarah E Cusson, Robert B Lobbia, and Alec D Gallimore. The h9 magnetically shielded hall thruster. In *35th International Electric Propulsion Conference*, pages 2017–232. Electric Rocket Propulsion Soc., 2017.

[16] Richard R Hofer, Robert S Jankovsky, and Alec D Gallimore. High-specific impulse hall thrusters, part 1: Influence of current density and magnetic field. *Journal of Propulsion and Power*, 22(4):721–731, 2006.

[17] Richard Robert Hofer. *Development and characterization of high-efficiency, high-specific impulse xenon Hall thrusters*. University of Michigan, 2004.

[18] BA Jorns and MP Byrne. Model for the dependence of cathode voltage in a hall thruster on facility pressure. *Plasma Sources Science and Technology*, 30(1):015012, 2021.

[19] HeatWave Labs. Standard series dispenser cathodes. `https://www.cathode.com/`.

[20] HeatWave Labs. Technical bulletin tb-147 processing of dispenser cathodes. `https://www.cathode.com/pdf/tb-147.pdf`.

[21] JM Lafferty. Boride cathodes. *Journal of Applied Physics*, 22(3):299–309, 1951.

[22] Michael A Lieberman and Allan J Lichtenberg. Principles of plasma discharges and materials processing. *MRS Bulletin*, 30(12):899–901, 1994.

[23] Jesse A Linnell and Alec D Gallimore. Efficiency analysis of a hall thruster operating with krypton and xenon. *Journal of Propulsion and Power*, 22(6):1402–1418, 2006.

[24] Mike Meyer, Les Johnson, Bryan Palaszewski, Dan Goebel, Harold White, and David Coote. Draft in-space propulsion systems roadmap technology area 02. *NASA Office of the Chief Technologist*, 2012.

[25] Michael Nakles, Lubos Brieda, Garrett Reed, William Hargus, and Randy Spicer. Experimental and numerical examination of the bht-200 hall thruster plume. In *43rd AIAA/ASME/SAE/ASEE Joint Propulsion Conference & Exhibit*, page 5305, 2007.

[26] Michael R Nakles, Ryne R Barry, C William Larson, and William A Hargus. A plume comparison of xenon and krypton propellant on a 600 w hall thruster. Technical report, AIR FORCE RESEARCH LAB EDWARDS AFB CA PROPULSION DIRECTORATE, 2009.

[27] Ali Enes Ozturk, Oguz Korkmaz, and Murat Celik. Design and analysis of different insert region heaters of a lanthanum hexaboride hollow cathode during initial heating. In *Space Propulsion Conference, Cologne, Germany*, 2014.

[28] Daniela Pedrini, Tommaso Misuri, Fabrizio Paganucci, and Mariano Andrenucci. Development of hollow cathodes for space electric propulsion at sitael. *Aerospace*, 4(2):26, 2017.

[29] James E Polk, Ioannis G Mikellides, Angela M Capece, and Ira Katz. Barium depletion in hollow cathode emitters. *Journal of Applied Physics*, 119(2):023303, 2016.

[30] PD Prewett and JE Allen. The double sheath associated with a hot cathode. *Proceedings of the Royal Society of London. A. Mathematical and Physical Sciences*, 348(1655):435–446, 1976.

[31] Y Raitses, A Smirnov, D Staack, and NJ Fisch. Measurements of secondary electron emission effects in the hall thruster discharge. *Physics of Plasmas*, 13(1):014502, 2006.

[32] Y Raitses, D Staack, A Smirnov, and NJ Fisch. Space charge saturated sheath regime and electron temperature saturation in hall thrusters. *Physics of Plasmas*, 12(7):073507, 2005.

[33] Yevgeny Raitses, David Staack, Michael Keidar, and Nathaniel J Fisch. Electron-wall interaction in hall thrusters. *Physics of Plasmas*, 12(5):057104, 2005.

[34] Daniel V Schroeder. An introduction to thermal physics, 1999.

[35] John S Snyder, Giiovanni Lenguito, Jason D Frieman, Thomas W Haag, and Jonathan A Mackey. The effects of background pressure on spt-140 thruster performance at multiple power levels. In *AIAA/SAE/ASEE Joint Propulsion Conference*, number GRC-E-DAA-TN57023, 2018.

[36] Phillip D Swartzentruber. Microstructure and work function of dispenser cathode coatings: effects on thermionic emission. 2014.

[37] PY CR Taunay, CJ Wordingham, and EY Choueiri. Physics of thermionic, orificed hollow cathodes: I. theory and experimental validation. *Plasma Sources Science and Technology*, 31(5):055006, 2022.

[38] Hiroki Watanabe, Shinatora Cho, and Kenichi Kubota. Performance evaluation of a 100-w class hall thruster. In *Proceedings of the 36th International Electric Propulsion Conference, University of Vienna, Wien, Austria*, pages 15–20, 2019.